Planetary radar astronomy

Steven J. Ostro

Jet Propulsion Laboratory, California Institute of Technology, Pasadena, California 91109

Radar is a powerful technique that has furnished otherwise unavailable information about solar system bodies for three decades. The advantages of radar in planetary astronomy result from (1) the observer's control of all the attributes of the coherent signal used to illuminate the target, especially the wave form's time/frequency modulation and polarization; (2) the ability of radar to resolve objects spatially via measurements of the distribution of echo power in time delay and Doppler frequency; (3) the pronounced degree to which delay-Doppler measurements constrain orbits and spin vectors; and (4) centimeter-to-meter wavelengths, which easily penetrate optically opaque planetary clouds and cometary comae, permit investigation of near-surface macrostructure and bulk density, and are sensitive to high concentrations of metal or, in certain situations, ice. Planetary radar astronomy has primarily involved observations with Earth-based radar telescopes, but also includes some experiments with a spaceborne transmitter or receiver. In addition to providing a wealth of information about the geological and dynamical properties of asteroids, comets, the inner planets, and natural satellites, radar experiments have established the scale of the solar system, have contributed significantly to the accuracy of planetary ephemerides, and have helped to constrain theories of gravitation. This review outlines radar astronomical techniques and describes principal observational results.

CONTENTS

I. Introduction 1235
II. History 1236
III. Instrumentation and Techniques 1236
A. Echo detectability 1236
B. Antennas and transmitting/receiving systems 1238
C. Measurements, observables, and target properties 1240
1. Albedo and polarization ratio 1240
2. Time delay and Doppler frequency 1242
3. Wave forms and signal processing 1243
D. Ephemerides 1244
1. Physical model and numerical implementation 1245
2. Reduction of delay/Doppler astrometry 1246
IV. Observational Results 1247
A. The scale of the solar system 1247
B. Tests of physical theories 1247
C. Asteroids and comets 1249
1. Dynamical experiments, orbits, and ephemerides 1249
2. Surface morphology, metal abundance, and meteoritic association 1250
3. Shapes of near-Earth asteroids: delay-Doppler imaging 1251
4. Cometary nuclei and large-particle clouds 1252
D. Rotations of Venus and Mercury 1254
E. Radar mapping of planetary surfaces 1257
1. Overview of techniques and results 1257
2. Scattering models and surface properties 1258
3. The radar exploration of Venus 1260
4. Anomalous features on Mars and Mercury 1263
F. The icy Galilean satellites 1264
1. Radar signatures 1264
2. Coherent backscattering 1266
G. Io and Titan 1269
V. Future Work 1270
Acknowledgments 1272
References 1272

I. INTRODUCTION

Planetary radar astronomy, a field at the intersection of planetary science and radio astronomy, is intimately bound to diverse subdisciplines within physical science. Ramifications of a single observation may involve the target's geologic characteristics at microscopic and topographic scales, its spin state, refinement of orbital parameters, constraints on electromagnetic scattering models, and tests of gravitation theories. Within this arena, there is a vigorous interplay between measurements and the refinement of planetary ephemerides. This iterative process has enriched the field, instilling within it a strong observational-theoretical dynamic.

Radar observations employ the state of the art in large radio antennas, powerful radar transmitters, low-noise receivers, and high-speed data-acquisition computers. One could think of a radar telescope as a radio telescope that can transmit, but that simplification would overlook both the difficulty of engineering a half-megawatt transmitter under severe weight/space constraints and the challenge of orchestrating the antenna, transmitter, receiver, computers, and recording devices into a single coordinated system.

A defining feature of planetary radar astronomy is human control of the transmitted signal used to illuminate the target. While virtually every other astronomical technique relies on passive measurement of reflected sunlight or naturally emitted radiation, radar employs coherent illumination whose polarization state and time/frequency structure are designed by the scientist. The general stratagem of a radar observation is to transmit a signal with very well-known characteristics and then, by comparing them to the characteristics of the echo, deduce the properties of the target. Hence the observer is intimately involved in an active astronomical observation and, in a very real sense, performs a controlled laboratory experiment on the target.

Radar delay-Doppler and interferometric techniques can spatially resolve a target whose angular extent is dwarfed by the antenna beamwidth. This capability is crucial for asteroids and planetary satellites, which almost always look like unresolved point sources through optical telescopes. Other advantages accrue from

 0034-6861/93/65(4)/1235(46)/$09.60 ©1993 The American Physical Society

centimeter-to-meter wavelengths, which penetrate comet comae and the clouds that obscure Venus and Titan, and which permit determination of near-surface roughness, bulk density, and metal concentration in planetary regoliths.

Throughout the physical sciences, novel experimental results have followed dramatic enhancements in experimental capabilities. This review was written three decades after the first interplanetary radar measurements and two years before the expected completion of upgrading projects that will render today's radar telescopes two orders of magnitude more powerful in terms of absolute sensitivity and imaging resolution. My goal has been a comprehensive, but by no means exhaustive, outline of techniques and results with an emphasis on observational highlights.

II. HISTORY

The roots of radar date back to ionospheric sounding measurements[1] in the decade following World War I (Breit and Tuve, 1926). Aircraft-detection radars were invented in several countries during the 1930s, and this technology developed rapidly during World War II (Hill, 1991). Echoes from the Moon were first detected on Jan. 10, 1946, at the Evans Signal Laboratory in Belmar, New Jersey, by the U.S. Army Signal Corps (Dewitt and Stodola, 1949; see also Mofenson, 1946), and on Feb. 6, 1946, by Bay (1947) at the Tungsram Research Laboratory in Ujpest, Hungary. These experiments were the product primarily of interest in electromagnetic propagation through the ionosphere and the possibility of using the Moon as a relay for radio communication (e.g., Grieg *et al.*, 1948). Radar investigations of the Moon began in earnest in the 1950s, when huge radio telescopes enabled investigations at wavelengths from 0.9 cm to 20 m, over most of the radar window (Evans, 1960, 1962). By 1963, improvements in the sensitivity of planetary radars had permitted the initial detections of echoes from Venus, Mercury, and Mars; see Thomson (1963) and Pettengill and Shapiro (1965) for historical accounts of the initial detections of those targets.

During the 1960s, radar ranging refined our knowledge of the astronomical unit and permitted calculation of ephemerides accurate enough to guide the first interplanetary space probes. Radar revealed the unusual rotations of Venus and Mercury and furnished the earliest indications of the topographic character of those objects and Mars. Venus has been imaged at increasingly finer resolution since the late 1960s; most recently, global mapping by the Magellan radar has revealed its surface with resolution as fine as ~ 100 m.

In the early 1970s, the detection of echoes from Saturn's rings offered the first strong evidence that a large fraction of the ring particles were centimeter-sized or larger. Radar first detected a near-Earth asteroid (1566 Icarus) in 1968, a mainbelt asteroid (1 Ceres) in 1977, a short-period comet (Encke) in 1980, and a long-period comet (IRAS-Araki-Alcock) in 1983. Echoes from a total of 69 asteroids and five comets (Table I) have provided new information about these objects' dimensions, spin vectors, surface structure, and composition. Radar has discovered large-particle clouds around two comets, has revealed two Earth-approaching asteroids to have contact-binary shapes, and has provided the most persuasive identifications to date of metallic objects in the mainbelt and near-Earth populations.

In the mid 1970s, shortly after the completion of the powerful 13-cm radar at the Arecibo Observatory, echoes from Europa, Ganymede, and Callisto revealed these icy moons' backscattering of circularly polarized waves to be outside the realm of previous radar experience and in want of a satisfactory explanation. Only recently has it become clear that coherent backscatter, or "weak localization," a process initially discovered in laboratory studies of the scattering of electrons and of light, accounts for the radar echoes from these objects.

In the late 1980s, the 21-km-diameter Martian moon Phobos was detected and found to have surface characteristics more reminiscent of some of the largest mainbelt asteroids than of near-Earth asteroids. During the past five years, the first radar detections of Titan have yielded large, variable albedo estimates at odds with predictions of a deep, global ocean of low-molecular-weight organics, and the first full-disc radar images of Mars and Mercury have led to the surprising discovery on each planet of polar caps with radar properties like those of the icy Galilean satellites. Most recently, radar echoes from asteroid 4179 Toutatis have provided the sharpest images yet of an object whose orbit can intersect that of the Earth.

III. INSTRUMENTATION AND TECHNIQUES

A. Echo detectability

Several factors determine whether a radar echo from a target at a range R is detectable. The received power $P_{\rm rcv}$ is given by the radar equation

$$P_{\rm rcv}=P_{\rm tx}G_{\rm ant}^2\lambda^2\sigma/(4\pi)^3R^4\ . \tag{1}$$

Here λ is wavelength, $P_{\rm tx}$ is transmitted power, and the antenna's gain $G_{\rm ant}$ is $4\pi/\lambda^2$ times the antenna's effective aperture $A_{\rm eff}$. The target's radar cross section σ, defined as 4π times the backscattered power per steradian per unit incident flux at the target, can be thought of as the

[1]Radar studies of the Earth's surface, atmosphere, or ionosphere are usually not considered part of planetary radar astronomy. Radar studies of the Sun involve such specialized methods and physical considerations that solar radar astronomy is considered separately from planetary radar astronomy. Similar distinctions apply to occultation experiments performed on planetary targets when they interrupt a spacecraft's radio transmissions.

TABLE I. Radar-detected planetary targets.

Year of first detection	Planets, satellites, rings	Mainbelt asteroids	Near-Earth asteroids	Comets
1946	Moon			
1961	Venus			
1962	Mercury			
1963	Mars			
1968			1566 Icarus	
1972			1685 Toro	
1973	Saturn's rings			
1974	Ganymede			
1975	Callisto		433 Eros	
	Europa			
1976	Io		1580 Betulia	
1977		1 Ceres		
1979		4 Vesta		
1980		7 Iris		
		16 Psyche	1862 Apollo	Encke
1981		97 Klotho	1915 Quetzalcoatl	
		8 Flora	2100 Ra-Shalom	
1982		2 Pallas		Grigg-Skjellerup
		12 Victoria		
		19 Fortuna		
		46 Hestia		
1983		5 Astraea	1620 Geographos	IRAS-Araki-Alcock
		139 Juewa	2201 Oljato	Sugano-Saigusa-Fujikawa
		356 Liguria		
		80 Sappho		
		694 Ekard		
1984		9 Metis	2101 Adonis	
		554 Peraga		
		144 Vibilia		
1985		6 Hebe	1627 Ivar	Halley
		41 Daphne	1036 Ganymed	
		21 Lutetia	1866 Sisyphus	
		33 Polyhymnia		
		84 Klio		
		192 Nausikaa		
		230 Athamantis		
		216 Kleopatra		
		18 Melpolmene		
1986		393 Lampetia	1986 DA	
		27 Euterpe	1986 JK	
			3103 1982 BB	
			3199 Nefertiti	
1987		532 Herculina	1981 Midas	
		20 Massalia	3757 1982 XB	
1988	Phobos	654 Zelinda	3908 1980 PA	
		105 Artemis		
1989	Titan		4034 1986 PA	
			1989 JA	
			4769 Castalia	
			1917 Cuyo	
1990		78 Diana	1990 MF	
		194 Prokne	1990 OS	
			4544 Xanthus	
1991		324 Bamberga	1991 AQ	
		796 Sarita	1991 JX	
			1991 EE	
1992			5189 1990 UQ	
			4179 Toutatis	

projected area of a perfectly reflective metal sphere that would give the same echo power as the target if observed at the target's location. This monostatic (single-station) equation is easily modified to accommodate observations that use separate antennas for transmitting and receiving.

The received power might be small compared to the receiver noise power, $P_{\rm noise}=kT_{\rm sys}\Delta f$, where k is Boltzmann's constant, $T_{\rm sys}$ is the system temperature, and Δf is the data's frequency resolution. However, the mean level of $P_{\rm noise}$ usually constitutes a stable background that can be estimated and removed, so $P_{\rm rcv}$ will be detectable as long as it significantly exceeds the noise power's standard deviation, $P_{\rm noise}/(\Delta f\Delta t)^{1/2}$, where Δt is the data's total integration time. In most work $\Delta t=N_{\rm coh}/\Delta f$, where $N_{\rm coh}$ is the number of independent estimates of $P_{\rm rcv}$, or "looks," that have been incoherently summed. The fluctuations in $P_{\rm noise}$ are chi-square distributed with $2N_{\rm coh}$ degrees of freedom, but that distribution approaches a Gaussian as $N_{\rm coh}$ increases (Kendall and Stuart, 1977).

The signal-to-noise ratio, $SNR=P_{\rm rcv}/\Delta P_{\rm noise}$, will be maximized for a frequency resolution comparable to the echo's intrinsic bandwidth, which will be proportional to $D/\lambda P$, where D and P are the target's diameter and spin period. Defining the radar albedo $\hat{\sigma}$ as the ratio of the target's radar cross section to its projected area, we can write

$$SNR\sim(\text{System factor})\,(\text{Target factor})\,(\Delta t)^{1/2}\ , \quad (2)$$

where

$$\text{System factor}\sim P_{\rm tx}A_{\rm eff}^2/\lambda^{3/2}T_{\rm sys}$$
$$\sim P_{\rm tx}G_{\rm ant}^2\lambda^{5/2}/T_{\rm sys} \quad (2a)$$

and

$$\text{Target factor}\sim\hat{\sigma}D^{3/2}P^{1/2}/R^4\ . \quad (2b)$$

Sensitive radar telescopes that incorporate large antennas, powerful transmitters, and low-noise amplifiers are needed to overcome the inverse fourth-power dependence of the echo strength on distance.

B. Antennas and transmitting/receiving systems

The two active planetary radar facilities are the Arecibo ($\lambda=13$ and 70 cm) and Goldstone (3.5 and 13 cm) instruments. For each instrument, the shorter-wavelength system is the more sensitive; typical 1992 characteristics are $P_{\rm tx}\sim450$ kW, $G_{\rm ant}\sim10^{7.1}$, and $T_{\rm sys}\sim25$ K.

The Arecibo radio-radar telescope (Fig. 1) in Puerto Rico is part of the National Astronomy and Ionosphere Center, operated by Cornell University for the National Science Foundation. The instrument consists of a 305-m-diameter fixed reflector, whose surface is a section of a 265-m-radius sphere, and aberration-correcting line feeds suspended some 130 m above the reflector. The motion of the feeds along elevation and azimuth rails enables the telescope, at latitude 18° N, to track targets as far as 20° from the zenith. (See the Arecibo Observatory's User's Manual, 1989.) The Arecibo telescope is being upgraded to increase its sensitivity by more than an order of magnitude. The improvement is to be achieved by constructing a ground screen around the periphery of the dish, replacing high-frequency line feeds with a Gregorian subreflector configuration, doubling the transmitter power, and installing a fine-guidance pointing system.

The Goldstone Solar System Radar (Dvorsky *et al.*,

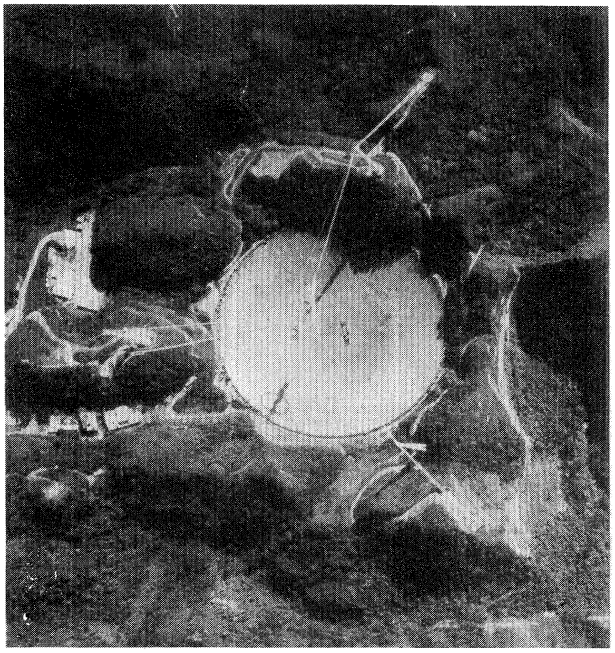

(a)

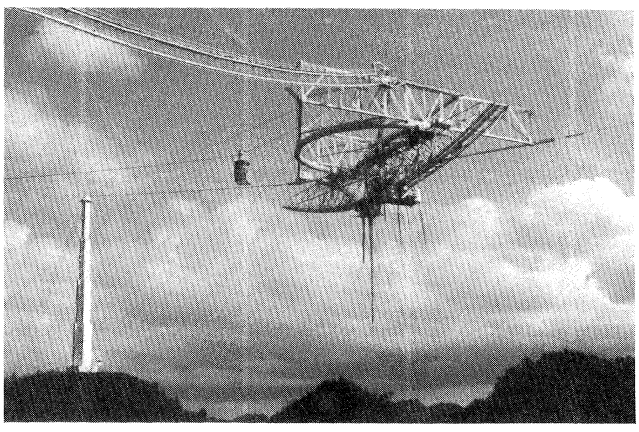

(b)

FIG. 1. The Arecibo Observatory in Puerto Rico: (a) aerial view; (b) the structure suspended above the reflector. Antenna feeds extend from the bottom of two carriage houses that contain the transmitter and the maser amplifier. Courtesy National Astronomy and Ionosphere Center.

1992; Priest, 1993) in California is part of NASA's Deep Space Network, which is operated by the Jet Propulsion Laboratory/California Institute of Technology. The Goldstone main instrument (Fig. 2) is a fully steerable, 70-m, Cassegrain antenna with horn feeds. The 1992 Arecibo 13-cm (S band, 2380 MHz) system is twice as sensitive as the Goldstone 3.5-cm (X band, 8510 MHz) system, but Goldstone can track targets continuously for much longer periods and has access to the whole sky north of $-40°$ declination. Bistatic experiments employing 3.5-cm transmission from Goldstone and reception of echoes at the 27-antenna Very Large Array (VLA) in New Mexico achieve about 50% more sensitivity than the 1992 Arecibo for targets whose echo bandwidths are at least as large as the VLA's finest frequency resolution. The Goldstone-VLA system can synthesize a beamwidth as small as 0.24 seconds of arc, vs 2 minutes of arc for single-dish observations.

Figure 3 shows the relative sensitivities of planetary radar systems as a function of target declination. In the mid 1990s, it is expected that Arecibo will have twice the range and will see 3 times the volume of Goldstone, while Goldstone will see twice the sky solid angle and will have 3 times the hour angle coverage of Arecibo.

Both Arecibo and Goldstone rely on transmitters built around one or more klystron vacuum-tube amplifiers (e.g., Cormier and Mizuhara, 1992; Edde, 1993). These tubes magnetically focus electrons falling through a $\sim$50-kV potential drop and impose a carrier-frequency modulation on their velocities and hence on the local electron density. Parasitic resonant cavities enhance this modulation, and about half of the input DC power is converted to carrier-frequency power, passed through a waveguide to the antenna feed or horn, and radiated. The rest of the input power is waste heat that must be transported away from the klystron by cooling water. The impact of the electrons on the collector anode generates x rays that must be contained by heavy metal shielding surrounding the tube. Cooling and shielding requirements raise the transmitter system's weight, complexity, and cost. Figure 4(a) shows a klystron similar to the two that currently power the Goldstone 3.5-cm radar.

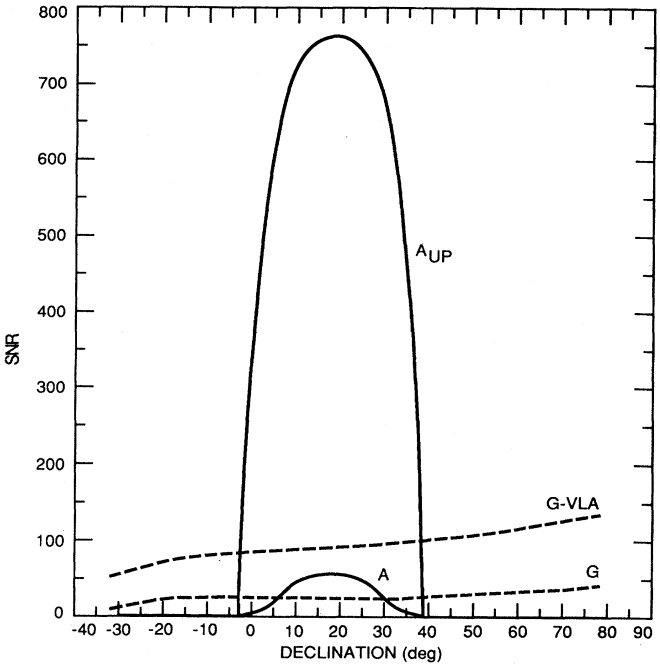

FIG. 3. Radar system sensitivities. The single-date SNR of echoes from a typical 1-km asteroid at a distance of 0.1 AU is plotted against declination for Goldstone (G), the Goldstone-VLA system (G-VLA), Arecibo (A), and the upgraded Arecibo (A_{UP}).

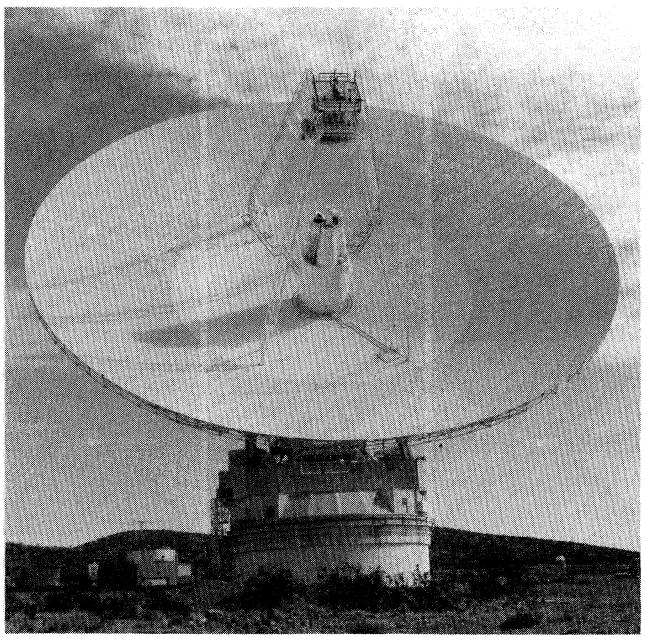

FIG. 2. The 70-m Goldstone Solar System Radar antenna (DSS 14) in California. Planetary radar equipment is at the secondary focus in the nearest of the three cones.

Figure 5 is a highly simplified block diagram of a single-antenna planetary radar system. A waveguide switch is used to connect the antenna to the transmitter or to the receiver. The front end of the superheterodyne receiving system is a helium-cooled ruby-maser amplifier like the one shown in Fig. 4(b) (Jet Propulsion Laboratory, 1983; Kraus, 1986, p. 7-44). The signal is mixed with a reference frequency to convert it down to intermediate frequencies for which transmission line losses are small, passed from the proximity of the antenna feed to a remote control room containing additional stages of signal processing equipment, converted to very low ("baseband") frequencies, filtered, and amplified (e.g., Edde, 1993). The Arecibo 13-cm system converts the received signal from 2380 MHz to 30 MHz and then to baseband, and the Goldstone 3.5-cm system uses four in-

termediate frequencies (325, 75, 50, and 7 MHz) in the conversion from 8510 MHz to baseband. Digital samples of the complex voltage are taken rapidly enough to avoid aliasing within the bandwidth of interest, generally between 100 Hz and 10 MHz. The nature of the final processing prior to recording of data on tape or disk depends on the experiment's objectives and on the time/frequency modulation of the transmission.

C. Measurements, observables, and target properties

1. Albedo and polarization ratio

In most modern radar observations, the transmission is circularly polarized and two parallel receiving channels are used to receive echoes in the same circular polarization as transmitted (the SC sense) and simultaneously in the opposite (OC) sense. The handedness, or helicity, of a circularly polarized wave is reversed on normal reflection from a plane mirror, so single backreflections from dielectric interfaces whose sizes and radii of curvature greatly exceed the wavelength yield echoes almost entirely in the opposite circular (OC) polarization. Same circular (SC) echo power can arise from multiple scattering, from single backscattering from interfaces with wavelength-scale radii of curvature (e.g., rocks), or from subsurface refraction effects. Therefore the circular polarization ratio

$$\mu_C = \sigma_{SC}/\sigma_{OC} \tag{3}$$

is a useful gauge of the target's near-surface, wavelength-scale complexity, or "roughness." When linear polarizations are used, it is convenient to define the linear polarization ratio

$$\mu_L = \sigma_{OL}/\sigma_{SL} \, . \tag{4}$$

Both μ_L and μ_C would be zero for a perfectly smooth target. A target consisting of randomly oriented dipoles would give $\mu_L = \frac{1}{3}$ and $\mu_C = 1$ (Long, 1965). For all radar-detected planetary targets, $\mu_L < 1$ and $\mu_L < \mu_C$.

A primary objective of the initial radar reconnaissance of a planetary target is to estimate its radar cross sections in the OC and SC [and occasionally the SL (same linear) and OL (opposite linear)] polarizations. Uncertainties in

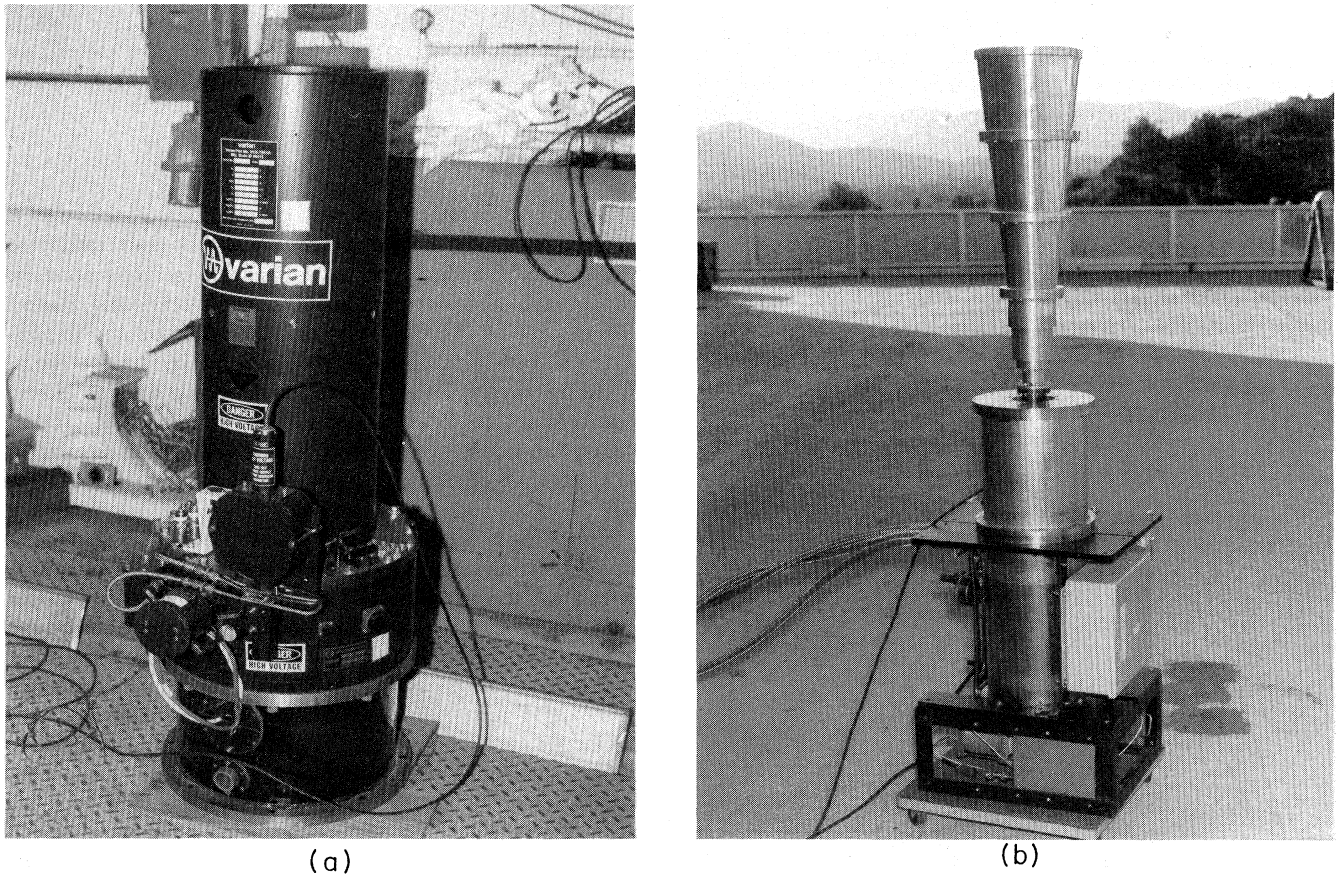

FIG. 4. Transmitter and receiver components: (a) A 250-kW, 8510-MHz klystron mounted in its solenoid and sitting in its stand. The tube is 1.5 m tall and weighs 835 lb. (b) 8510-MHz traveling-wave maser and feed horn. The maser's closed-cycle refrigeration system uses recirculating helium gas. The entire apparatus stands 1.7 m tall (JPL/NASA).

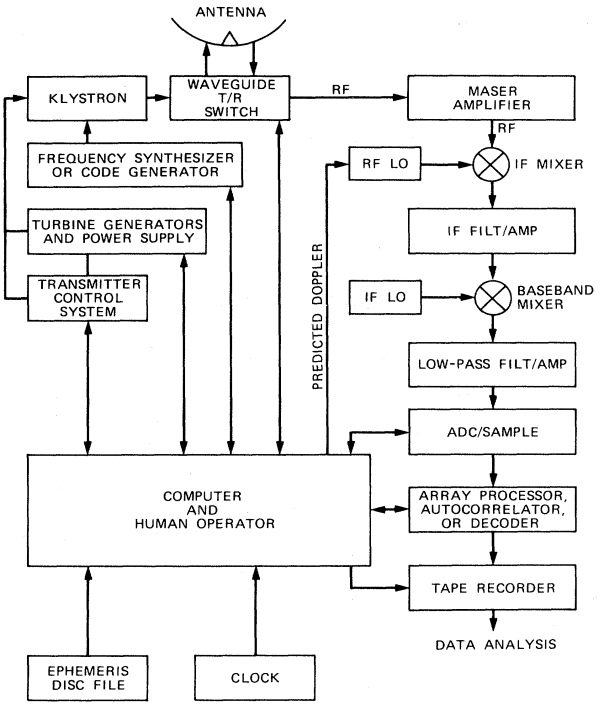

FIG. 5. Block diagram of a planetary radar system. RF LO and IF LO denote radio frequency and intermediate frequency local oscillators, and ADC denotes analog-to-digital conversion.

radar system parameters usually place a floor of ~25% on absolute measurement of radar cross sections and ~5% on relative (run-to-run and date-to-date) measurements, but the polarization ratios are much less sensitive to systematic effects. The most widely used measures of radar reflectivity are the OC radar albedo

$$\hat{\sigma}_{OC}=\sigma_{OC}/A_{proj}\ , \tag{5}$$

where A_{proj} is the target's projected area (estimated optically or with radar), and the total power (OC +SC=OL+SL) radar albedo $\hat{\sigma}_T$, which is 4 times the geometric albedo used in optical planetary astronomy. A perfectly smooth metallic sphere would have $\hat{\sigma}_{OC}=\hat{\sigma}_{SL}=1$.

The disc-integrated radar properties μ_C and $\hat{\sigma}_{OC}$ have been estimated for some six dozen targets (Table II and Fig. 6) and reveal striking diversity among surfaces in the solar system. Subsequent sections of this paper focus on the radar properties of bodies that occupy different parts of Fig. 6.

For solid-surfaced targets with low μ_C, the physical interpretation of the radar albedo is clear-cut, as the surface must be smooth at all scales within about an order of magnitude of the wavelength and the subsurface must lack structure at those scales down to several $1/e$ power absorption lengths L. Here we may interpret the radar albedo as the product gR, where R is the Fresnel power

TABLE II. Radar properties of some solar system targets. Typical 13-cm (2380 MHz) values are given for the OC radar cross section σ_{OC}, the OC radar albedo $\hat{\sigma}_{OC}$, the circular polarization (SC/OC) ratio μ_C, the delay and Doppler dispersions, and the product of those dispersions. Here τ_{min} is the minimum echo time delay for radar observations to date. IAA denotes comet IRAS-Araki-Alcock.

Target	τ_{min} (min)	σ_{OC} (km^2)	$\hat{\sigma}_{OC}$	μ_C	Maximum dispersions Delay (ms)	Maximum dispersions Doppler (Hz)	Product
Moon	0.04	6.6×10^5	0.07	0.1	12	60	0.7
Mercury	9.1	1.1×10^6	0.06	0.1	16	110	2
Venus	4.5	1.3×10^7	0.11	0.1	40	110	4
Mars	6.2	2.9×10^6	0.08	0.3	23	7600	170
Phobos	6.2	22	0.06	0.1	0.1	100	10^{-2}
1 Ceres	26	3.3×10^4	0.05	0.0	3	3100	9
2 Pallas	25	2.1×10^4	0.09	0.0	2	2000	4
12 Victoria	17	2.1×10^3	0.15	0.1	0.5	590	3
16 Psyche	28	1.4×10^4	0.29	0.1	0.8	2200	2
324 Bamberga	13	2.9×10^3	0.06	0.1	0.8	230	0.2
1685 Toro	2.3	1.7	0.1	0.2	0.02	14	10^{-4}
1682 Apollo	0.9	0.2	0.1	0.4	0.01	16	10^{-4}
2100 Ra-Shalom	3.0	1.0	0.1	0.2	0.01	5	10^{-4}
2201 Adonis	1.5	0.02	?	1.0	?	2	?
4769 Castalia	0.6	0.2	0.15	0.3	0.01	10	10^{-4}
IAA nucleus	0.5	2.4	?	0.1	?	4	?
IAA cloud	0.5	0.8	?	0.01	?	600	?
Io	66	2×10^6	0.2	0.5	12	2400	29
Europa	66	8×10^6	1.0	1.5	10	1000	11
Ganymede	66	1×10^7	0.6	1.4	18	850	15
Callisto	66	5×10^6	0.3	1.2	16	330	5
Saturn's rings	134	10^8–10^9	0.7	0.5	1600	6×10^5	10^6

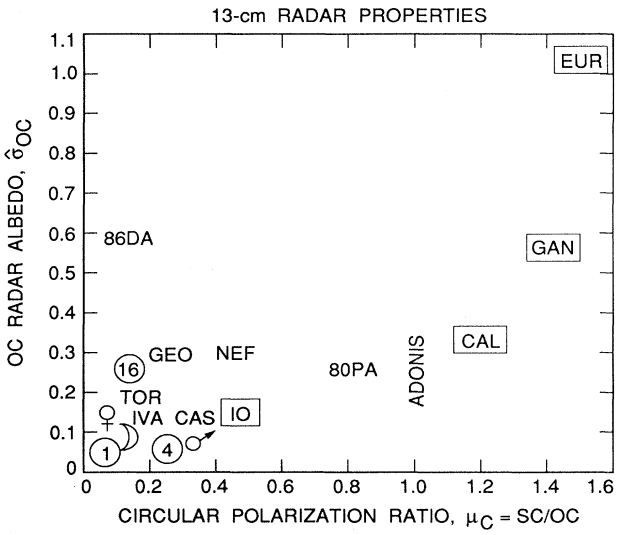

FIG. 6. 13-cm radar properties for selected planetary targets. Symbols are used for the Moon, Venus, and Mars. The circled numbers denote the mainbelt asteroids 1 Ceres, 4 Vesta, and 16 Psyche. Rectangles identify the Galilean satellites Io, Europa, Ganymede, and Calllisto. Note the diverse properties of the near-Earth asteroids 1986 DA, 3199 Nefertiti, 1620 Geographos, 1980 PA, 1685 Toro, 1627 Ivar, 4769 Castalia, and 2101 Adonis, whose albedo is uncertain. See Table II.

reflection coefficient at normal incidence and the backscatter gain g depends on target orientation, shape, and the distribution of surface slopes with respect to that shape. For most applications to date, g is $\sim 10\%$ larger than unity, so the radar albedo provides a reasonable first approximation to R. Both R and L depend on interesting characteristics of the surface material, including bulk density, porosity, particle-size distribution, and metal abundance. For example, L is several wavelengths for solid assemblages (rocks) of common silicate minerals and is of order ten wavelengths for powdered assemblages with porosities $\sim 45\%$, a typical value for the regoliths of loose, unconsolidated, fragmental debris that cover the Moon and most other planetary radar targets (Campbell and Ulrichs, 1969). Corresponding values of L for water ice are orders of magnitude larger (Warren, 1984). For dry, unconsolidated powders, R depends primarily on surface bulk density; several simple empirical expressions have proven useful (Garvin *et al.*, 1985; Ulaby *et al.*, 1990). For solids, small volume concentrations of metal particles in a silicate matrix can increase R by an amount that depends on the electrical properties of each phase as well as the particles' dimensions and packing geometry (Kelly *et al.*, 1953; Nielson, 1974; Bergman, 1978; Pettengill, Ford, and Chapman, 1988; Sihvola and Kong, 1988).

If $\mu_C \gg 0.1$, then physical interpretations are more complicated and less unique, because models must allow not just for the nature of the surface/space interface but also for the regolith's structural and electrical properties, including the size distribution, spatial distribution, and scattering properties of subsurface rocks (Sec. IV.E.2). A similar statement applies to echoes from multiparticle distributions, i.e., Saturn's rings and large-particle comet clouds. Section IV.F addresses the especially interesting case of $\mu_C > 1$.

2. Time delay and Doppler frequency

A typical transmit/receive cycle, or run, consists of signal transmission for a duration close to the round-trip light time between the radar and the target (until the first echoes are about to come back), followed by reception of echoes for a similar duration. In continuous wave (cw) observations, one transmits an unmodulated, nearly monochromatic wave form and measures the distribution of echo power as a function of frequency. In ranging observations, time coding of the wave form permits measurement of the distribution of echo power in time delay (range) as well.

Time and frequency measurements have paramount importance in radar astronomy, because the delay/Doppler distribution of echo power is the source of the finest spatial resolution, and also because delay and Doppler are fundamental dynamical observables. The echo time delay and Doppler frequency shift change continuously due to the relative motion of the target with respect to the radar. To avoid smearing of accumulated echoes in time and frequency, one tunes the receiver's front-end local oscillator according to an ephemeris based on an orbit determined from optical, and perhaps radar, "astrometric" observations. In some cases it is more convenient to take out the Doppler on the uplink, that is, to continuously tune the transmitter so the receiver sees a constant carrier frequency. In time-resolved experiments, one drifts the sampling time base according to the predicted rate of change of time delay to maintain constant registration of the samples with respect to the target's center of mass.

Reliable, precise time/frequency measurements are made possible by high-speed data-acquisition systems and stable, accurate clocks and frequency standards. Radar measurements and site ephemerides are referenced to Coordinated Universal Time (UTC), which differs from International Atomic Time (TAI) by an integral number of seconds and is maintained within ± 0.9 s of Universal Time (UT1) through the introduction of leap seconds by the International Earth Rotation Service (e.g., Seidelman *et al.*, 1992). UT1 is derived from UT0, the location-dependent time scale based on observations of the diurnal motions of stars, by correcting UT0 for the shifts in longitude of observing sites caused by polar motion. The unit of all these time scales is the *Système International* (SI) second, defined as the duration of 9 192 631 770 cycles of radiation from the transition between the two hyperfine levels of the ground state of cesium 133. The fractional

accuracy of cesium atomic clocks is better than 10^{-13} (Ramsey, 1988, 1990; see also Beehler *et al.*, 1965). TAI, the most precisely determined time scale available for astronomical use, is established by the *Bureau International des Poids et Mesures* in Paris from analyses of data from cesium clocks in many countries. The independent argument for apparent geocentric ephemerides, Terrestrial Dynamical Time (TDT), equals TAI+32.184 s and uses a unit, the TDT day, equal to 86400 s at mean sea level. The independent argument of dynamical theories and of planetary ephemerides referred to the solar system's barycenter is Barycentric Dynamical Time (TDB), which differs from TDT by periodic variations. In the language of general relativity, TDT and UTC are proper times and TDB is a coordinate time (see, for example, Karttunen *et al.*, 1987, and Seidelmann *et al.*, 1992).

A radar observatory's timekeeping centers on a stable master oscillator that drives a time code generator and serves as the frequency reference for oscillators used in the various stages of frequency generation/conversion in the receiver and transmitter systems. For instance, the Arecibo Observatory's master oscillator is a hydrogen maser, which over periods of several hours is stable to 10^{-15} (Ramsey, 1988, 1990). The maser is backed up by a cesium clock with much greater long-term stability. The observatory receives radio transmissions from (1) Global Positioning System (GPS) satellites that simultaneously view Arecibo and the National Institute of Standards and Technology (NIST) in Boulder, Colorado, and provide UTC accurate to 10^{-8} s; (2) GPS satellites that view Arecibo, but not the NIST, and provide UTC accurate to 10^{-7} s; and (3) Loran-C (Florida), which provides an estimate of UTC by the U.S. Naval Observatory accurate to 0.3 μs modulo 5 μs. The differences between the time code generator and the local clocks are recorded daily. Several times per hour a GPS satellite viewing both Arecibo and Boulder transmits UTC according to Rb/Cs clocks on the satellite, and each ground station records the difference between its local clocks and the satellite clocks. (The GPS system is discussed by Leick, 1990, and the GPS common-view technique is described by Weiss and Allan, 1987.) The NIST computer system phones Arecibo daily and retrieves a record of these differences. Periodically, the NIST pools globally distributed Cs clocks to define TAI and publishes *a posteriori* estimates of the relation between Arecibo's Cs clock time and TAI. The observatory's time code generator is linked through a computer to the timing generator that triggers the transmitter and the sampler at the back end of the receiver.

In simple terms, the round-trip-time delay, τ, between transmission of a signal and reception of its echo is approximately $2R/c$, with c the speed of light and R the distance to the target. For a target 1 astronomical unit (AU) from the radar, the time delay would be 988 s; delays encountered in actual experiments range from 2.5 seconds for the Moon to 2.5 hours for Saturn's rings and Titan. The echo's Doppler frequency ν is approximately $-2F_{tx}v/c$, where F_{tx} is the transmitter carrier frequency and v is the target's radial velocity; thus the magnitude of ν in hertz is simply the radial velocity in half wavelengths per second. Dopplers within an order of magnitude of $\pm 10^5$ Hz are common in Arecibo/Goldstone experiments.

Different parts of a rotating target have different velocities relative to the radar, so the echo will be dispersed in Doppler as well as in delay. The dispersion and the functional form of the delay-Doppler distribution of echo power $\sigma(\tau,\nu)$ depend on the target's size, shape, scattering characteristics, and orientation. For a sphere with diameter D and apparent rotation period P, echoes would have a delay dispersion (depth) given by $\Delta\tau_{tar}=D/c$ and a frequency dispersion, or bandwidth, $\Delta\nu_{tar}=(4\pi D\cos\delta)/\lambda P$, where δ is the angle between the radar line of sight and the target's equatorial plane. For any rigid target, contours of constant frequency are defined by planes parallel to both the line of sight and the apparent spin vector.

The basic strategy of most radar experiments is to constrain the target's properties by measuring $\sigma(\tau,\nu)$, perhaps with more than one combination of transmitted and received polarizations and perhaps as a function of time, i.e., as a function of the target's orientation and direction. Ideally, one would like to obtain $\sigma(\tau,\nu)$ with very fine resolution, sampling that function within cells whose dimensions $\Delta\tau\times\Delta\nu$ are (1) small compared to the echo dispersions $\Delta\tau_{tar}\times\Delta\nu_{tar}$, to achieve fine fractional spatial resolution of the target, and (2) small compared to the magnitudes of the echo's mean delay and Doppler, to permit refinement of the target's orbit. Table II lists delay/Doppler dispersions and minimum delays for selected targets.

Planetary radar systems work with wave forms that provide time resolution as fine as 10^{-7} s. This limit, set by the $\sim$10-MHz maximum modulation bandwidth of klystron amplifiers, corresponds to 15-m range resolution. Bounds on frequency resolution are set by certain hardware limitations as well as by the coherence times of recordable data sets; subhertz resolutions are quite common.

3. Wave forms and signal processing

In cw experiments, complex voltage samples of the received signal are Fourier transformed, and the resultant real and imaginary components are squared and summed to obtain an estimate of the power spectrum. The frequency resolution equals the reciprocal of the time series' length, i.e., of the coherence time. The number of fast Fourier transforms (FFTs) applied to data from a single transmit/receive cycle can range from 1 to tens of thousands. Most planetary radar targets are sufficiently narrow band for power spectra to be computed, accumulated, and recorded in real time. Even so, sometimes it is preferable to record voltages so FFTs of different lengths

can be used later to view the echoes at different spectral resolutions. For wideband echoes (e.g., $\sim 10^6$ Hz for Saturn's rings at 13 cm), the sampling-rate requirements are met by passing the signal through a digital correlator, recording autocorrelation functions, and then doing the spectral analysis (Jenkins and Watts, 1968; Kraus, 1986, p. 7-60).

Delay resolution requires a modulated wave form. For example, with a coherent-pulsed cw wave form (e.g., Pettengill, *et al.*, 1962, 1967), the transmitter's carrier-frequency oscillator operates continuously, but power is radiated only during intervals that are one delay resolution cell long and occur at intervals called the pulse repetition period (PRP). A PRP greater than the target's delay depth avoids delay aliasing by ensuring that the echo will consist of successive, nonoverlapping range profiles. However, a time-delay measurement with any repetitive ranging wave form is ambiguous modulo the PRP. This ambiguity is irrelevant if the PRP is much greater than the *a priori* uncertainty in the delay-prediction ephemeris. Otherwise, one must do two observations with noncommensurate PRPs whose product then defines a joint ambiguity that can be made arbitrarily large compared to the formal delay-prediction uncertainty.

The maximum effective sampling rate at any given delay, 1/PRP, sets the unaliased bandwidth of the received signal. Fourier transformation of N samples of the signal's complex voltage taken at the same position (i.e., the same delay relative to the delay of hypothetical echoes from the target's center of mass) within each of N successive range profiles yields the echo spectrum for the corresponding range cell on the target, with a frequency resolution $1/(N\,\mathrm{PRP})$. The bandwidth, and hence the recording rate and the spectral resolution achievable with a given FFT length, can be reduced by a factor of N_{coh} in real time by coherently summing N_{coh} successive, PRP-long time series of voltage samples.

Modern planetary radar systems use a binary-phase-coded cw wave form to simulate a coherent-pulsed cw wave form (e.g., Pettengill, 1970). This alternative to amplitude modulation has several advantages: By transmitting power continuously, one maximizes average output power and hence signal-to-noise ratio (SNR). One also extends the klystron's lifetime by avoiding on-off switching intervals comparable to the tube's internal thermal time constants. The basic time interval of the phase-coded wave form, called the baud, sets the delay resolution $\Delta\tau$. Once every $\Delta\tau$ seconds, the phase of the transmitted signal is either shifted by 180° or not, according to the value of the corresponding element in a preset binary code. Shift-register, "pseudo-random" codes, which are easy to generate and have very sharply peaked autocorrelation functions, are ubiquitous in radar astronomy. Shift-register code lengths equal 2^M-1, with M a whole number typically between 7 and 13. In most delay/Doppler experiments, the code is repeated continuously during the transmission, so the PRP is the product of the baud and the code length. The received signal is decoded by cross-correlating it with a replica of a single code cycle. The ambiguity function (i.e., the delay-Doppler response to a point target; Deley, 1970) for a radar system using binary-phase-coded cw resembles that of a coherent-pulsed cw system.

For coherent-pulsed cw and repetitive binary-phase-coded cw wave forms, the time/frequency nonaliasing requirements noted above preclude complete, simultaneous delay-Doppler investigation of targets if $\Delta\tau_{\mathrm{tar}}\Delta\nu_{\mathrm{tar}} > 1$. The inner planets, the Galilean satellites, the largest asteroids, and Saturn's rings are "overspread" at the primary Arecibo and Goldstone frequencies. Some aliasing may be acceptable, depending on the experimental objectives and the nature of the echo. Virtually all planetary radar observations since the mid 1970s have used cw or phase-coded cw wave forms. However, delay-Doppler imaging of targets overspread by factors > 100 almost always requires different wave forms. For example, a frequency-stepped wave form was used (Ostro, Pettengill *et al.*, 1982) to image Saturn's rings, which are overspread by $\sim 10^6$ at 13 cm. Frequency-swept, or "chirped," wave forms have been used in some planetary radar experiments (e.g., Kotel'nikov, 1965) and are widely used in radar remote sensing of the Earth.

For observations of Mars, overspread by a factor of several hundred, a new technique uses a nonrepeating, binary-phase-coded cw wave form (Harmon, Sulzer, *et al.*, 1992). The received signal for any given delay cell is decoded by multiplying it by a suitably lagged replica of the code. Developed for observations of the ionosphere (Sulzer, 1986, 1989), this "coded-long-pulse" or "random-code" wave form redistributes delay-aliased echo power into an additive white-noise background. The SNR is reduced accordingly, but this penalty is acceptable for strong targets. More elaborate wave forms, involving a combination of random noise modulation and polarization modulation, have also been studied (Hagfors and Kofman, 1991).

D. Ephemerides

The fine precision of radar time/frequency measurements places stringent demands on the accuracy of planetary ephemerides, because the predictions of delay and Doppler [$\tau_{\mathrm{eph}}(t)$ and $\nu_{\mathrm{eph}}(t)$] must be accurate enough to prevent smearing of echoes, which would compromise the data's SNR and delay/Doppler resolution. Since (see Shapiro, Ash, and Tausner, 1966)

$$d\tau(t)/dt = -\nu(t)/F_{\mathrm{tx}} \ . \tag{6}$$

a Doppler prediction error of $\Delta\nu_{\mathrm{eph}}$ will cause echoes integrated over one round-trip time (RTT) to be smeared in time delay by $(-\Delta\nu_{\mathrm{eph}}/F_{\mathrm{tx}})RTT$. This quantity sets a floor on delay measurement precision that often exceeds the ~ 0.1-μs limit set by the klystron modulation bandwidth.

Considerable effort is devoted to delay-Doppler astrometry of newly discovered Earth-approaching asteroids and comets. For these objects, errors in prediction ephemerides are large and grow rapidly, because orbits must be estimated from optical astrometric data that span very short arcs. During initial radar observations of such an object at 0.04 AU (RTT ~40 s), the delay uncertainty might be 0.4 s (~10 Earth radii) and the 2380-MHz Doppler uncertainty might be 1 kHz (or 17 μs of delay smear during a 40-s receive period). A delay measurement with a 40-μs baud could reduce the instantaneous delay uncertainty by four orders of magnitude, allowing one to generate more accurate delay-Doppler predictions, which would permit much more precise radar astrometry, and so on.

This iterative, "bootstrapping" process has always been a fundamental part of radar astronomy, not just in orbit improvement but also in the refinement of the planetary and lunar ephemerides themselves, i.e., their underlying theories, model parameters, and computational methods (Shapiro, 1968; Newhall *et al.*, 1983). Whereas analytical techniques had sufficed to calculate ephemerides when there existed only angular positional measurements of solar system bodies, the advent of radar observations in the 1960s and subsequent improvements in radar instruments required development of increasingly comprehensive physical models along with numerical integration methods able to match the precision of the measurements. The current needs of radar astronomy are served by the programs PEP770 at the Center for Astrophysics and DE200 at the Jet Propulsion Laboratory.

1. Physical model and numerical implementation

The foundation of the ephemeris programs are equations of motion that model point-mass interactions, terrestrial and lunar figure effects, Earth tides, and lunar physical librations (Standish *et al.*, 1992). The model treats the Sun, the Moon, and the nine planets as point masses in the isotropic, parametrized post-Newtonian (PPN) n-body metric with Newtonian gravitational perturbations from large mainbelt asteroids. As discussed in detail by Will (1984, 1987), the accuracy of the post-Newtonian (slow motion, weak field) limit is adequate for all foreseeable solar system tests of general relativity and other metric theories of gravity, in which the only gravitational field entering the equations of motion is the space-time metric $\mathbf{g}$. In the post-Newtonian limit, $\mathbf{g}$ can be expanded in terms of dimensionless gravitational potentials of varying degrees of smallness; different metric theories assign different numerical values to the coefficients that multiply the potentials. The PPN formalism writes those coefficients in terms of parameters that measure or indicate properties of metric theories. For example, the Eddington-Robertson-Schiff parameters γ and β are used to describe the "classical" tests of general relativity, and α_1, α_2, α_3 measure whether a theory predicts post-Newtonian preferred frame effects.

The ephemeris programs use equations for point-mass accelerations that are derived from the variation of a time-dependent Lagrangian action integral referenced to a nonrotating solar system barycentric coordinate frame. The barycenter is given by

$$\sum_i \mu_i^* \mathbf{r}_i = \mathbf{0}, \tag{7}$$

where

$$\mu_i^* = \mu_i \{ 2c^2 + v_i^2 - \sum_{j \neq i} \mu_j / |\mathbf{r}_j - \mathbf{r}_i| \} / 2c^2 . \tag{7a}$$

Here μ_i is the mass of body i times the gravitational constant G; $\mathbf{r}_i$ is the barycentric position of body i; and $v_i = |\dot{\mathbf{r}}_i|$. Each of these equations depends on the other, and they must be iterated in each step in the integration of the equations of motion. For each body i, the point-mass acceleration can be written (Newhall *et al.*, 1983) as

$$\begin{aligned}\ddot{\mathbf{r}}_i = \sum_{j \neq i} \frac{\mu_j (\mathbf{r}_j - \mathbf{r}_i)}{r_{ij}^3} \Bigg\{ 1 - \frac{2(\beta+\gamma)}{c^2} \sum_{k \neq i} \frac{\mu_k}{r_{ik}} - \frac{2(\beta-1)}{c^2} \sum_{k \neq j} \frac{\mu_k}{r_{jk}} + \gamma \left[\frac{v_i}{c} \right]^2 + (1+\gamma) \left[\frac{v_j}{c} \right]^2 - \frac{2(1+\gamma)}{c^2} \dot{\mathbf{r}}_i \cdot \dot{\mathbf{r}}_j \\ - \frac{3}{2c^2} \left[\frac{(\mathbf{r}_i - \mathbf{r}_j) \cdot \dot{\mathbf{r}}_j}{r_{ij}} \right]^2 + \frac{1}{2c^2} (\mathbf{r}_j - \mathbf{r}_i) \cdot \ddot{\mathbf{r}}_j \Bigg\} \\ + \frac{1}{c^2} \sum_{j \neq i} \frac{\mu_j}{r_{ij}^3} \{ [\mathbf{r}_i - \mathbf{r}_j] \cdot [(2+2\gamma)\dot{\mathbf{r}}_i - (1+2\gamma)\dot{\mathbf{r}}_j] \} (\dot{\mathbf{r}}_i - \dot{\mathbf{r}}_j) + \frac{3+4\gamma}{2c^2} \sum_{j \neq i} \frac{\mu_j \ddot{\mathbf{r}}_j}{r_{ij}} + \sum_{m=1}^{5} \frac{\mu_m (\mathbf{r}_m - \mathbf{r}_j)}{r_{im}^3} .\end{aligned} \tag{8}$$

where $\mathbf{r}_i$ is the barycentric position of body i, $r_{ij} = |\mathbf{r}_j - \mathbf{r}_i|$, and the PPN parameters β and γ equal unity in general relativity. Quantities with the m subscript refer to the five asteroids (1 Ceres, 2 Pallas, 4 Vesta, 7 Iris, and 324 Bamberga) found to have the most pronounced effects on the motion of Mars. The barycentric acceleration of each body j due to Newtonian effects of the remaining bodies and the asteroids is denoted by $\ddot{\mathbf{r}}_j$.

The ephemeris generated by the numerical integration program is a file of planetary positions, velocities, and accelerations at equally spaced epochs. The integrator requires the input of various parameters, including adopted constants (c, G, planetary mass ratios, etc.), and parameters that are estimated from fits to observational data (e.g., corrections to planetary orbital elements). The distinction between constants and estimated parameters is

flexible, since any quantity can be assigned arbitrary freedom via adjustment of its *a priori* variance.

Much attention once was devoted to the accuracy of numerical integration/estimation techniques and the validity and completeness of the physical model. At present, the greatest concern is the fitting of ephemerides to new data types whose quality, quantity, variety, and time coverage directly determine the accuracy of the results (Standish, 1990). The major data types are optical transit circle timings, optical plate data, radar delay/Doppler astrometry, spacecraft transponderer ranging, and lunar laser ranging. Recent planetary ephemerides result from least-squares fits of ~ 100 parameters to some 7×10^5 observations (Standish and Hellings, 1989).

2. Reduction of delay/Doppler astrometry

A radar astrometric measurement consists of an estimate of $\tau(t)$ or $\nu(t)$ for echoes received at the telescope's reference point at a specified UTC epoch t. The reference point for most Arecibo observations is the center of curvature of the main reflector, and the reference point for most Goldstone observations with the 70-m antenna (DSS 14) is the top of the antenna cone. The Earth-fixed coordinates of those points are tabulated by Yeomans *et al.* (1992). Usually it is adequate to think of the offsets $[\tau_0(t)=\tau(t)-\tau_{\rm eph}(t)$ and $\nu_0(t)=\nu(t)-\nu_{\rm eph}(t)]$ of the echoes from the ephemeris predictions as being constant over the pertinent measurement time scales, typically between one round-trip time and a few hours. In practice, one measures τ_0 or ν_0 and reports $\tau(t)$ or $\nu(t)$ for a convenient epoch near the weighted mean time of the measurements.

For the terrestrial planets and large satellites, mean radii are now well known, but topography introduces uncertainty into the difference between a range profile's reference point [perhaps the peak or the leading edge of $\sigma(\tau)$] and the delay of hypothetical echoes from the target's center of mass. Much of the effect of topography on the ephemeris refinement process can be eliminated by observing a particular subradar point on two dates when the orbital positions of the Earth and target are different. Such "closure-point" measurements will be largely immune to topographic "noise" and therefore can provide sharpened sensitivity to quantities in physical theories that are otherwise difficult to constrain, e.g., solar oblateness.

The modeling of radar delay/Doppler measurements requires light-time solutions for the upleg and downleg portions of the signal path. The formulations, which are solved iteratively (e.g., Ash *et al.*, 1967; Shapiro, 1968; Yeomans *et al.*, 1992), consider target size, electron density along paths through the solar corona and the troposphere, geodetic positions of the reference points on the (not necessarily colocated) transmitting and receiving antennas, and corrections for general relativistic effects, as follows (Standish, 1990). With the TDB and UTC times of an echo's reception denoted by t_r and $\mathrm{UTC}(t_r)$, the echo's UTC time delay is

$$\tau=\mathrm{UTC}(t_r)-\mathrm{UTC}(t_r-\tau_D-\tau_U)\ , \tag{9}$$

where

$$\tau_U=|\mathbf{r}_{\rm tar}(t-\tau_D)-\mathbf{r}_{\rm tx}(t-\tau_D-\tau_U)|/c + \Delta\tau_U[\mathrm{rel}]+\Delta\tau_U[\mathrm{cor}]+\Delta\tau_U[\mathrm{tro}] \tag{9a}$$

and

$$\tau_D=|\mathbf{r}_{\rm rcv}(t)-\mathbf{r}_{\rm tar}(t-\tau_D)|/c+\Delta\tau_D[\mathrm{rel}] + \Delta\tau_D[\mathrm{cor}]+\Delta\tau_D[\mathrm{tro}]\ . \tag{9b}$$

Here τ_U and τ_D are the upleg and downleg TDB light times; $\mathbf{r}_{\rm tx}$, $\mathbf{r}_{\rm rcv}$, and $\mathbf{r}_{\rm tar}$ are the solar system barycentric positions of the reference points on the transmitting antenna, the receiving antenna, and the target. The station location vectors are rotated into the (presumably inertial) frame of the ephemerides, using an Earth model that incorporates effects of precession, nutation, polar motion, and variable rotation rate (Sovers and Fanselow, 1987; Wahr, 1988).

The $\Delta\tau[\ ]$ terms in Eqs. (9) are corrections due to general relativity and propagation through the solar corona and the Earth's troposphere. For each leg, the integrated relativistic contribution to the delay is (Shapiro, 1964, 1980; Shapiro, Pettengill, *et al.*, 1971)

$$\Delta\tau[\mathrm{rel}]=(1+\gamma)\mu_{\rm sun}c^{-3}\ln|(\mathrm{SE}+\mathrm{ST}+\mathrm{ET})/(\mathrm{SE}+\mathrm{ST}-\mathrm{ET})|\ , \tag{10}$$

where SE, ST, and ET are distances between the positions of the Sun, the Earth, and the target at appropriate epochs. The frequency-dependent contribution from the solar corona is found by integrating over the density of ionized electrons along the signal path (Anderson *et al.*, 1978).

The Doppler frequency shift ν includes indirect terms due to the dependence of the reflection and transmission times on the time delay as well as relativistic corrections for expressing UTC in terms of TDB (Yeomans *et al.*, 1992). Those authors give the following equation for the Doppler shift accurate to second order in v/c (see also Shapiro, Ash, and Tausner, 1966; Moyer, 1971):

$$\nu=-(F_{\rm tx}/c)(\dot R_{\rm tx}+\dot R_{\rm rcv})-(F_{\rm tx}/c^2)[(\mathbf{R}_{\rm tx}\cdot\mathbf{v}_{\rm tx})(\dot R_{\rm tx}/R_{\rm tx})-(\mathbf{R}_{\rm rvc}\cdot\mathbf{v}_{\rm rcv})(\dot R_{\rm rcv}/R_{\rm rcv})-\dot R_{\rm tx}\dot R_{\rm rcv} +\mu_{\rm sun}(1/|\mathbf{r}_{\rm tx}-\mathbf{r}_{\rm sun}|-1/|\mathbf{r}_{\rm rcv}-\mathbf{r}_{\rm sun}|)+(|\dot{\mathbf{r}}_{\rm tx}|^2-|\dot{\mathbf{r}}_{\rm rcv}|^2)/2]\ . \tag{11}$$

Here $\mathbf{r}_{sun}$ is the barycentric position of the Sun's center of mass; $\mathbf{v}$ denotes a barycentric velocity; the upleg and downleg vectors are

$$\mathbf{R}_{rcv}=\mathbf{r}_{tar}(t_r-\tau_D)-\mathbf{r}_{rcv}(t_r) \tag{11a}$$

and

$$\mathbf{R}_{tx}=\mathbf{r}_{tar}(t_r-\tau_D)-\mathbf{r}_{tx}(t_r-\tau_D-\tau_U)\ ; \tag{11b}$$

and the rates of change of the corresponding distances are

$$\dot{R}_{tx}=(1/R_{tx})\mathbf{R}_{tx}\cdot\dot{\mathbf{R}}_{tx} \tag{11c}$$

and

$$\dot{R}_{rcv}=(1/R_{rcv})\mathbf{R}_{rcv}\cdot\dot{\mathbf{R}}_{rcv}\ . \tag{11d}$$

IV. OBSERVATIONAL RESULTS

A. The scale of the solar system

In the International Astronomical Union (IAU) System of units (Seidelmann and Wilkins, 1992), the defining constants are the speed of light, $c=299\,792\,458$ m s^{-1}, and the Gaussian constant, $k=0.017\,202\,098\,95$ AU$^{3/2}$ d^{-1}, which by Kepler's third law defines the astronomical system of units of mass (the Sun's mass), time (1 day$=86\,400$ seconds of dynamical time), and length (the astronomical unit). The dimensions of k^2 are those of G; in the least-squares fits of the planetary ephemerides, $k^2=\mu_{sun}$ is fixed at $(0.017\,202\,098\,95)^2$ AU^3 d^{-2} and the meter equivalent of the AU is treated as a free parameter. Prior to the advent of planetary radar 30 years ago, solutions rested on optical angle measurements alone, and the fractional uncertainty in the meter equivalent of the AU was of order 10^{-3}. For this reason, refinement of the AU helped drive the first Venus radar experiments, which improved the optical value by nearly three orders of magnitude (Shapiro, 1965; see also Muhleman *et al.*, 1962) and enabled navigation of the Mariner II spacecraft to Venus. During the mid 1960s, more precise radar observations led to improvements in estimates of many parameters: the Earth-Moon mass ratio; the masses of the inner planets; the orbital elements of Mercury, Venus, and the Earth; and the radii of Mercury and Venus, as well as commensurate further refinement in the AU (e.g., Ash *et al.*, 1967, 1971). Currently, the data type with the strongest influence on solutions for the AU is the set of Viking Lander ranging points, which have *a priori* standard deviations ~ 20 ns$=6$ m (Williams and Standish, 1989; Standish, 1990). In the IAU system of constants, 1 AU$=449.004\,783\,7$ light-seconds, or $149\,597\,870.66$ km.

B. Tests of physical theories

Radar refinement of planetary orbits has allowed increasingly decisive tests of physical theories for light, gravitational fields, and their interactions with matter and each other. For example, radar furnished the initial experimental verification of the second-order, "longitudinal" term in the special relativistic Doppler formula (Fig. 7; Shapiro, Ash, and Tausner, 1966). As noted by those authors, the same theory of light propagation that leads to the Doppler formula is intimately woven into the process by which optical and time-delay astrometry is used to calculate planetary orbits. Hence Fig. 7 represents a test of the consistency of the laws of planetary dynamics and the theory of light propagation.

Radar also provided the initial measurements (Shapiro, Pettengill, *et al.*, 1968; Shapiro, Ash, Ingalls, *et al.*, 1971) of the non-Newtonian, "extra" retardation $\Delta\tau$[rel] of electromagnetic signals that pass close to a massive body (Shapiro, 1964). For propagation within several solar radii of the Sun, as in a Mercury or Venus radar experiment with the target near superior geocentric conjunction, $\Delta\tau$[rel] is approximately $(1+\gamma)$ $[120-10\ln(d^2/r)]$ μs, where r is the radar-target distance in AU and d is the minimum distance, in solar radii, between the path and the center of the Sun (Shapiro, 1964; see also Will, 1987). The magnitude of $\Delta\tau$[rel] for a Sun-grazing path would be of order 250 μs, or considerably more than the intrinsic uncertainty in time-delay

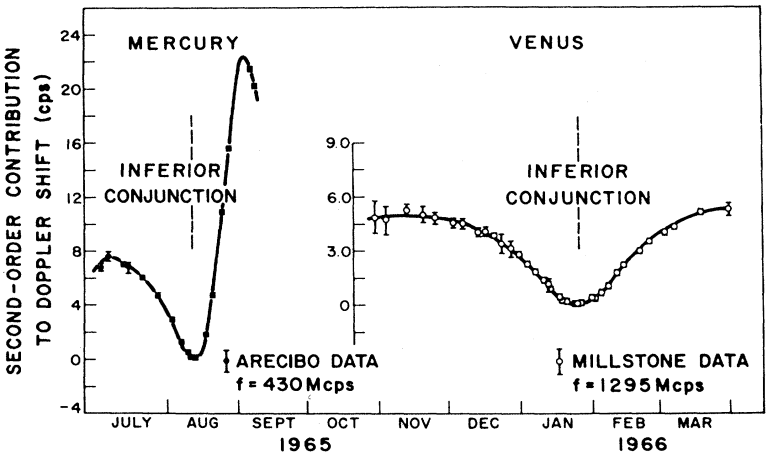

FIG. 7. Comparison of theory (solid curves) and radar observations for second-order velocity contributions to the special relativistic Doppler formula (Shapiro *et al.*, 1966). The plotted points were obtained from the measured Dopplers by subtracting the first-order theoretical contributions.

measurements even with 1960s equipment. However, $\Delta\tau$[rel] is not a direct observable but rather a function of imprecisely known parameters (e.g., target masses and orbital elements) that are themselves to be constrained by time-delay measurements. That is, time-delay measurements must be used simultaneously to refine ephemerides and to discriminate between relativistic and Newtonian predictions (Shapiro, 1966). This difficulty, which is distinct from instrumental limitations as well as from systematic sources of uncertainty due to topographic noise and coronal propagation, can be overcome because $\Delta\tau$[rel] decreases logarithmically away from superior conjunction and is very small between elongation and inferior conjunction. One approach (Shapiro, Pettengill, *et al.*, 1968) is to measure delays for a variety of Earth-target-Sun geometries and then separate the data into two sets, one composed of measurements far from superior conjunction and hence not expected to be influenced very much by solar gravity, and one consisting of measurements near superior conjunction. The first set constrains orbital parameters; the second is compared with predictions based on the relativistic theory and the ephemerides estimated from the first set.

Figure 8 shows a sample of postfit residuals for Earth-Venus time-delay experiments, with respect to the excess retardation predicted by general relativity (Shapiro, Pettengill, *et al.*, 1971). Those author's estimate of the PPN parameter γ, 1.03 ± 0.04, was improved in the 1970s by spacecraft ranging, particularly to the Viking Orbiters and Landers. An analysis by Reasenberg *et al.* (1979) yielded $\gamma=1.000\pm0.002$, where the uncertainty is intended to encompass systematic effects assessed in part from a variety of test solutions based on different data and parameter sets.

The sensitivity of certain physical parameters to combinations of data has been central to the study of the excess advance of Mercury's perihelion. The extra shift that remains after accounting for precesssion of the equinoxes and perturbations by other planets is known to about 0.5% from planetary radar measurements (e.g., Shapiro, Pettengill, *et al.*, 1972) and is in excellent agreement with the general relativistic prediction (42.98" per century; Nobili and Will, 1986) if the Sun's quadrupole moment J_2 is $\sim1\times10^{-7}$, which corresponds to the oblateness expected for a uniformly rotating Sun. For that value of J_2, the Newtonian quadrupole gravitational field would contribute only ~0.01" per century. However, values of J_2 several hundred times larger have been offered on various observational and theoretical grounds (see Will's 1984 and 1987 discussions), raising the possibility that the solar quadrupole moment accounts for up to $\sim10\%$ of the excess shift. Accordingly, a current challenge is separation of the effects of J_2 and relevant PPN parameters. The separation is possible because J_2 and relativistic gravity induce different periodic perturbations in a planet's orbit and because different planets undergo different perihelion shifts.

The ephemeris software of the Jet Propulsion Laboratory and the Center for Astrophysics lets one use the data types noted earlier and lunar laser ranges to estimate various parameter subsets [e.g., J_2, PPN parameters, the time derivative ($\dot{G}$) of the gravitational constant, and parameters that represent the ratio of passive gravitational mass to inertial mass for solar system bodies (Anderson *et al.*, 1978)]. Hellings (1984) described separation of β, γ, α_1, and J_2, and Shapiro, Smith, Ash, Ingalls, and Pettengill (1971) placed an upper limit of 4×10^{-10} yr^{-1} on $\dot{G}/G$, using planetary radar time delays, primarily to Mercury. Analyses incorporating the other data types, including Viking lander ranges, have yielded upper limits on $\dot{G}/G\sim10^{-11}$ yr^{-1} (e.g., Hellings *et al.*, 1983; Reasenberg, 1983). Although the Viking data are very precise, the orbit of Mars is perturbed by

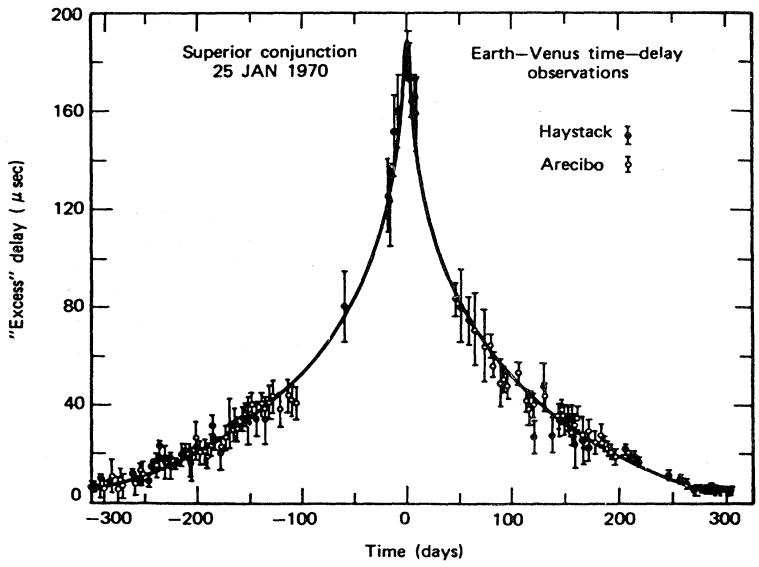

FIG. 8. Comparison of measured and predicted effects of general relativity on Earth-Venus time delays. After Shapiro, Ash, Ingalls, *et al.* (1971).

mainbelt asteroids, and uncertainties in asteroid masses limit the leverage of Mars spacecraft data in determination of $\dot{G}/G$ (Williams, 1984). This situation can be mitigated somewhat by incorporating precise Mercury and Venus radar ranges (e.g., Anderson *et al.*, 1991). Inclusion of data from the Pioneer Venus Orbiter and from the Galileo spacecraft's Venus flyby yields a null result for $\dot{G}/G$ with a standard error of $\pm 2.0 \times 10^{-12}$ yr^{-1} (Anderson *et al.*, 1992).

There is promise for shrinking the variances and covariances associated with estimates of J_2 and $\dot{G}/G$ by extending the time base of Mercury radar ranging and by improving the accuracy of the measurements through closure-point and simultaneous Arecibo/Goldstone observations. Better estimates of the mass distribution in the main asteroid belt would also strengthen the estimations. Whereas the three largest asteroids, 1 Ceres, 2 Pallas, and 4 Vesta, have large periodic effects in the Earth-Mars range that are separable and allow reliable estimation of their masses (Hellings *et al.*, 1983; Standish and Hellings, 1989), the ~200 next largest asteroids have well-determined sizes but poorly known compositions and densities. Radar is a powerful source of information about asteroid physical properties and orbits.

C. Asteroids and comets

1. Dynamical experiments, orbits, and ephemerides

The most reliable pre-radar values for the AU and the mass of the Earth-Moon system were based on optical observations of the Mars-orbit-crossing asteroid 433 Eros (Brouwer and Clemence, 1961; McGuire *et al.*, 1961; Rabe, 1971). Soon after the object's 1898 discovery, it became clear that Eros astrometry could also yield an accurate estimate of the Mars/Sun mass ratio (Russell, 1900). Precedents for using asteroid astrometry to constrain the AU and planetary masses had been set by various nineteenth-century scientists (Hill, 1873; Harkness, 1891).

Whereas spacecraft tracking has supplanted the use of asteroids for planetary mass determination, a subset of Earth-approaching asteroids are potentially of interest for testing gravitational theories. The subkilometer object 1566 Icarus, discovered in 1949, is in an orbit ($a=1.1$ AU, $e=0.83$, $i=23°$) that brings it to about 0.1 AU from Earth once every ~19 years and that is expected to show a relativistic precession of about 10" per century (Gilvarry, 1953). For optical astrometry over a specified time interval, Icarus might provide a more stringent test of relativistic predictions than Mercury, because of its closer approaches, larger orbital eccentricity, and smaller size (Shapiro, Ash, and Smith, 1968). Unfortunately, as discussed by Shapiro, Smith, Ash, and Herrick (1971), available optical observations are undermined by inadequacies in star catalogs used to reduce the photographic plates, and the radar data (Goldstein, 1968; Pettengill, Shapiro, *et al.*, 1969) are limited to low-SNR cw measurements over two days. On the other hand, improved astrometric data will be obtainable during future Icarus close approaches: In 1996, Arecibo should provide time-delay estimates tied to the asteroid's center of mass with uncertainties ~1 μs (~150 m).

Icarus is unlikely to be the only "dynamically useful" asteroid accessible to radar. Earth resides in an Earth-crossing[2] asteroid (ECA) swarm thought to contain thousands of objects larger than Icarus and $\sim 10^8$ larger than ~10 m, which is the size of the smallest asteroid discovered so far and also corresponds to the finest delay resolution achievable with existing radars. Most of the ~300 known near-Earth asteroids (NEAs; roughly half ECAs and half Mars crossers) have been discovered since 1987. The completeness of the current census of ECAs larger than 10, 1, 0.1, and 0.01 km is thought to be about 1, 0.05, 0.0003, 0.000 001. A two-decade effort with dedicated optical telescopes (Morrison, 1992) could discover ~100 000 ECAs, of which some 30% can be expected to traverse the detectability windows of the upgraded Arecibo and Goldstone telescopes at least once during any several-decade period. Some may be in orbits ideal for radar studies of relativistic effects, with eccentricity slightly over 0.9 and semimajor axis near 0.6 AU, aligned to make annual close Earth approaches (Shapiro, 1987). The recently discovered object 1991 RC is in an Icarus-like orbit ($a=1.1$, $e=0.83$, $i=24°$), but is not a strong radar target in the near future.

There are strong motivations to discover NEAs, refine their orbits, and determine their physical properties. These objects include fragments of mainbelt asteroids (MBAs) and devolatilized comet nuclei; some might be parent bodies of meteorites, which are the sources of key constraints on the origin and evolution of the solar system (Wetherill, 1988; Wetherill and Chapman, 1988; Weissman *et al.*, 1989). A subset of the NEAs might be derived from remnants of the planetesimal swarm from which the Earth formed (Wetherill, 1977). Many NEAs are more accessible than the Moon in terms of spacecraft propulsion requirements and therefore are candidates for flyby, rendezvous, and sample-return missions (Swindle *et al.*, 1991).

Our telescopic knowledge of NEA characteristics is

[2]The term "Earth crossing" applies to orbits that might intersect the orbit of the Earth as a consequence of secular perturbations by the planets (Shoemaker *et al.*, 1979, 1990). For orbits that overlap Earth's, intersections are caused primarily by precession of the asteroid's orbital major axis. If the overlap is continuous, as with Icarus, four crossings occur during each precession cycle (10^3 to 10^5 years). All asteroid orbits with one node outside Earth's orbit and the other inside are Earth crossing. For asteroids on orbits that approach within about 0.3 AU of Earth's orbit but do not overlap it, secular variations in eccentricity can lead to part-time overlap, and a study of secular perturbations (e.g., Williams, 1969) or numerical integration of the orbit is required to determine whether it is Earth crossing.

meager, because most of those objects are optically so dim and spatially unresolvable (McFadden *et al.*, 1989). In addition, uncertainties in NEA orbits and hence ephemerides are rendered very large by the frequency of close planetary encounters and in some cases by orbital resonances. The orbits become chaotically unpredictable over time scales of order 10^4 yr; that is, a minute change in initial conditions leads to exponential divergence of the calculated orbit, which after such a long time span can lie virtually anywhere in a large region of the phase space (e.g., Wisdom, 1987; Milani *et al.*, 1989). However, predictions of trajectories from orbital integrations lose their accuracy over much shorter time scales, hardly ever longer than several centuries, because of the astrometric measurements' uncertainties and short time base. For NEAs observed during a single apparition, the interval over which an integration yields accurate prediction ephemerides can be less than a year or, in some cases, only a few months. Consequently some 10% of newly discovered NEAs are lost.

Radar astrometry during the discovery apparition can ensure optical recovery of newly discovered NEAs, because delay-Doppler measurements have fine fractional precision and are orthogonal to optical, angular-position measurements (Yeomans *et al.*, 1987). Radar commonly improves upon the accuracy of optical-only ephemerides of newly discovered NEAs by one to three orders of magnitude. Even for asteroids with very long astrometric histories and secure orbits, radar measurements can significantly shrink their positional uncertainties for decades, with implications for the navigation of spacecraft to asteroids and also for predictions of extremely close approaches of asteroids to Earth. Ostro, Campbell, Chandler, Shapiro, *et al.*, (1991) give pre-1991 asteroid radar astrometry, and Yeomans *et al.* (1992) give orbits for 34 targets based on the combined radar and optical data. As an example of recent radar astrometry, observations of 1991 JX with a 0.2-μs baud yielded a time-delay estimate whose fractional precision is five parts in 10^9 (Ostro, Harmon, *et al.*, 1991).

2. Surface morphology, metal abundance, and meteoritic association

The ability of delay-Doppler radar observations to synthesize spatial resolution is its key advantage for investigation of small bodies, but disc-integrated radar properties also provide useful constraints on surface characteristics. The dispersion of NEA albedos and polarization ratios (Fig. 6) implies great diversity among these objects' surface compositions and morphologies. The very large values of μ_C of some NEAs (Ostro, Campbell, Chandler, Shapiro, *et al.*, 1991) indicate extreme small-scale roughness, perhaps due to impact-produced structure on or near the surface. One of the roughest NEAs 3908 (1980 PA), has the optical spectroscopic signature of a differentiated basaltic surface. It may be similar in this respect to Vesta, although the visible-infrared data imply a regolith with larger grain sizes and more exposed bare rock on 3908 (Cruikshank *et al.*, 1991). Vesta, with a moderately rough surface ($\mu_C \sim 0.24$), is the largest asteroid thought to have undergone extensive melting, geochemical differentiation, and volcanic resurfacing. 3908's diameter is about 1 km; this object's extreme roughness ($\mu_C \sim 0.75$) might reflect the nature of impact cratering and debris retention on small basaltic bodies. Cruikshank *et al.* (1991) suggest that 3908 may be a fragment of a source body of the relatively rare meteorites called basaltic achondrites. That source body may have been Vesta, but it seems more likely that it was either excavated from Vesta (Binzel and Xu, 1993) or formed independently.

Undifferentiated meteorites (nonigneous rocks called chondrites) are relatively primitive and far more abundant than differentiated meteorites (achondrites, irons, and stony irons, all of which are igneous rocks). Laboratory studies of chondrites have furnished our most direct constraints on conditions in the solar nebula and on processes that led to formation of the planets (e.g., Wasson, 1985; Wood, 1985; Cassen and Boss, 1988) and of presolar, circumstellar, and interstellar material (Zinner, 1985; Anders, 1988). Similarly, the differentiated meteorites offer insights into the melting and chemical fractionation of planets and large satellites, and also into primordial thermal events in the early solar system (e.g., Hewitt and Newsom, 1988; Bell *et al.*, 1989). Since almost all meteorites are thought to be fragments of asteroids, much astronomical effort is devoted to obtaining and interpreting information about asteroid mineralogy. Many MBAs and a few NEAs have been classified on the basis of their photometric colors and albedos. Visible-infrared reflectance spectra have established important mineralogical characteristics, thereby limiting the set of plausible meteorite analogs for the most populous classes (Gaffey *et al.*, 1989; Lipschutz *et al.*, 1989; Britt *et al.*, 1992). For example, C asteroids contain hydrated silicates, carbon, and organic compounds and are analogous to carbonaceous chondrites. S asteroids contain pyroxene, olivine, and NiFe metal and probably correspond to stony irons and/or ordinary chondrites. M asteroids contain NiFe metal and/or assemblages of enstatite (a magnesium iron silicate) and NiFe metal and probably correspond to irons and/or enstatite chondrites.

Radar observations can constrain asteroid-meteorite relations, because metal concentration influences radar reflectivity dramatically and because iron and stony iron meteorites are much more metallic than chondrites. There is at least a fivefold variation in the radar albedos of MBAs, implying substantial variations in these objects' surface porosities or metal concentrations, or both (Ostro, Campbell, and Shapiro, 1985). The lowest MBA albedo estimate, $\hat{\sigma}_{OC}=0.05$ for Ceres (Fig. 6), indicates a slightly lower surface bulk density than on the Moon ($\hat{\sigma}_{OC}=0.07$), consistent with the inference from Ceres' reflectance spectra of a mineralogy resembling that of carbonaceous chondrites (Gaffey *et al.*, 1989). The radar

properties of the Martian satellite Phobos resemble those of large ($\geq$ 100 km) C-class mainbelt asteroids like Ceres (Ostro, Jurgens, *et al.*, 1989). The highest MBA albedo estimate, 0.29 for the 250-km-diameter, M object 16 Psyche, is consistent with lunar porosities and a metal concentration near unity. Psyche might be the collisionally stripped core of a differentiated asteroid and the largest piece of refined metal in the solar system.

Ostro, Campbell, Chandler, Hine, *et al.*, (1991) reported radar observations of C, S, and M NEAs and argued in favor of two hypotheses about NEA-meteorite associations: (1) that 1986 DA, the only radar-detected M NEA, is a relatively regolith-free iron-meteorite analog; and (2) that most S NEAs either are relatively regolith-free ordinary chondrite analogs or are relatively regolith-covered stony-iron analogs. The first hypothesis supports the idea that 1986 DA is derived from the interior of a much larger object that melted, differentiated, cooled, and subsequently was disrupted in a catastrophic collision. This 2-km asteroid, which appears smooth at centimeter-to-meter scales but irregular and possibly bifurcated at much larger scales, might be (or have been a part of) the parent body of some iron meteorites. The second hypothesis lends support to the view that many of the S objects are associated with ordinary chondrites, which are the most common kind of meteorite that falls on the Earth (Lipschutz *et al.*, 1989). This possibility is favored on dynamical grounds but runs counter to the currently favored interpretation of VIS/IR spectral signatures of large S MBAs as stony-iron assemblages. The flybys of the S asteroids 951 Gaspra and 243 Ida by the Galileo spacecraft may shed some light on this so-called spectroscopic paradox. Initial results from the Gaspra encounter suggest the presence of a regolith of uncertain thickness (Belton *et al.*, 1992). Eventually, a very long-term program of accurate radar ranging to mainbelt asteroids that perturb Mars may yield useful constraints on the masses, and hence the densities and mineralogies, of S asteroids (Standish and Hellings, 1989). As noted earlier, that work may also help improve the accuracy with which relativistic effects on the orbits of the inner planets and NEAs can be measured.

3. Shapes of near-Earth asteroids: delay-Doppler imaging

Radar observations can image asteroids and comets if the echoes are strong enough. Continuous wave (cw) observations yield echo spectra, $\sigma(\nu)$, that can be thought of as one-dimensional images, or brightness scans across the target through a slit parallel to the asteroid's apparent spin vector (Fig. 9). As shown in that figure, the bandwidth of a target's instantaneous echo power spectrum is proportional to the breadth, measured normal to the line of sight, of the target's pole-on silhouette. Measurements of echo edge frequencies as functions of rotation phase can be used to estimate the shape (and the size in units of km/cosδ) of the convex envelope, or hull, of the pole-on silhouette (Ostro, Connelly, and Belkora, 1988; Ostro, Rosema, and Jurgens, 1990). The hull can be thought of as the shape of a rubber band stretched around that silhouette. The hull's shape and the projected location within the hull of the asteroid's center of mass (c.m.) are coupled to the Doppler frequency f_0 of hypothetical echoes from the c.m.

Time-modulated wave forms yield a delay-Doppler image $\sigma(\tau,\nu)$, which can be thought of as the projection of the target's radar brightness onto its apparent equatorial plane. The image generally is "north/south ambiguous," because a constant-delay, constant-Doppler locus can intersect two points on opposite sides of the apparent equatorial plane: such points return echo with the same delay and Doppler. Measurement of $\sigma(\tau,\nu)$ as a function of rotation phase can remove the N/S ambiguity and also can provide enough information to permit accurate estimation of the three-dimensional shape, the spin vector, and the delay-Doppler trajectory of the c.m. Subradar latitude/longitude coverage and interferometry can strengthen such an estimation. Detailed reconstruction of target shapes (Hudson, 1993) is possible if the SNR

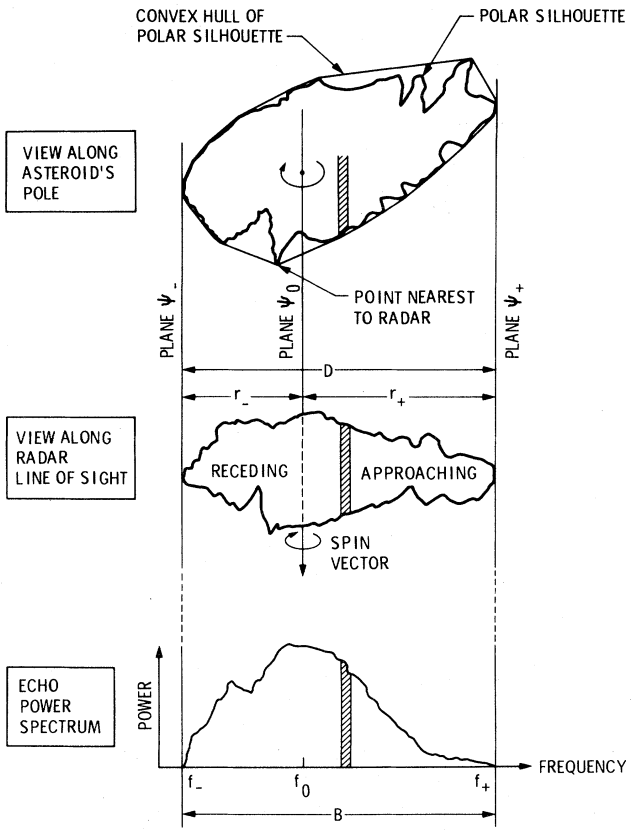

FIG. 9. Geometric relationships between an asteroid's shape and its echo power spectrum. The plane ψ_0 contains the line of sight and the asteroid's spin vector. Echo from any portion of the asteroid intersecting ψ_0 has Doppler frequency f_0. The crosshatched strip of power in the spectrum corresponds to echoes from the crosshatched strip on the asteroid. The x,y coordinate system (dark lines) rotates with the asteroid (Ostro, Connelly, and Belkora, 1988).

and subradar longitude/latitude coverage are adequate, and telescope upgrades should enable such work to be done routinely by the mid 1990s.

NEA echoes suggest an abundance of exotically shaped objects in the population. Pole-on silhouettes range from slightly noncircular to highly elongated and distinctly nonelliptical (e.g., Fig. 10). Delay-Doppler images of 1627 Ivar show this ~7-km object to be elongated, irregular, nonconvex, and bifurcated (Ostro, Campbell, Hine, *et al.*, 1990). Spectra of several other NEAs, including 2201 Oljato and 3908 (1980 PA), are double peaked at certain rotation phases, suggesting a bimodal distribution of mass.

Very strong evidence for contact-binary asteroids was obtained in 1989, when the Earth crosser 4769 Castalia (then designated 1989 PB) came deep inside the Arecibo detectability window two weeks after it was discovered by Helin (1989) at Palomar. Delay-Doppler observations yielded an image sequence [Fig. 11(a)] that shows two distinct, kilometer-sized lobes apparently in contact (Ostro, Chandler, Hine, *et al.*, 1990). In December 1992, when this article was being finalized, Goldstone observations of the Earth crosser 4179 Toutatis yielded images with thousands of on-target pixels (vs a few dozen for each Castalia frame), again revealing a double-lobed object (Ostro *et al.*, 1993). Preliminary reductions of selected Toutatis images [Fig. 11(b)] show each lobe to be irregular and pocked with craters that document a complex collisional history.

The most plausible scenario for a contact-binary asteroid's formation is that two previously independent components joined in a low-velocity collision. Hartmann (1979) suggested that a collision between two comparable-sized, large, mainbelt asteroids that shatters and disrupts them might disperse a fraction of the fragments with relative velocities low enough to produce gravitationally bound pairs, or larger groups, of fragments. Martelli *et al.* (1993) have described the origin of close asteroid binaries during the collisional fragmentation of larger asteroids.

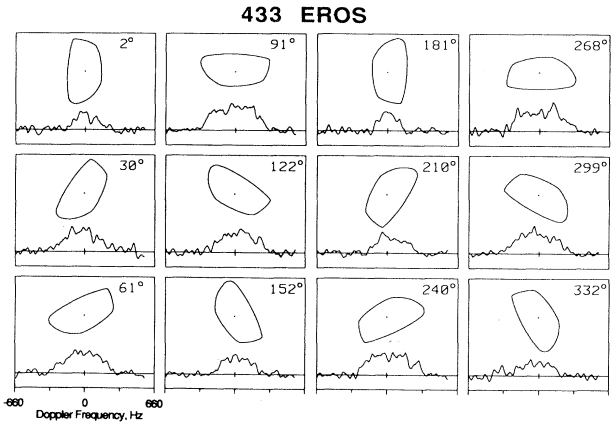

FIG. 10. Eros echo spectra and hull at 12 rotational phases. The hull is estimated from OC spectra whose phase coverage is uniform and thorough. Weighted sums of spectra within 30° windows have been filtered to a frequency resolution of 40 Hz and plotted on identical, linear scales of echo power vs frequency. A horizontal line is drawn at zero echo power, and a vertical bar at the origin indicates ±1 standard deviation of the noise. A replica of Eros's hull estimate is drawn above each spectrum at the same scale as the Doppler-frequency axis and at the indicated weighted-mean rotational phase. Note how the spectral bandwidth tracks the horizontal breadth of the hull (Ostro, Rosema, and Jurgens, 1990).

The radar evidence for the existence of contact-binary ECAs has implications for theories of the evolution of asteroids and meteorite parent bodies as well as for our understanding of the cratering history of the inner planets. For example, numerous impact-crater pairs on Earth and the Moon apparently were created by the nearly simultaneous impact of two separated projectiles of comparable size. On Earth, three out of the 28 known impact craters with diameters >20 km are widely separated doublets. Melosh and Stansberry (1991) argue that the occurrence of such doublet craters cannot be explained adequately by tidal disruption of gravitationally bound contact-binary asteroids beyond the Roche limit, by low-angle impact, or by atmospheric or tidal breakup of an object just prior to impact. Noting that cometary breakup near the Sun separates components too widely (Hut *et al.*, 1991), Melosh and Stansberry suggest that some 10% of the estimated ~2000 kilometer-sized ECAs may be well-separated binary asteroids. Weidenschilling *et al.* (1989) speculated that both primordial and recent binaries might exist and noted that knowledge of the abundance of binary asteroids could constrain the collisional history of the mainbelt population. Farinella (1992; see also Chauvineau *et al.*, 1991) has shown that tidal energy exchange during close planetary encounters would cause an initial Earth-crossing population of binaries with separations several times the radii of the components to evolve into a distribution of configurations, including both decreased separations (possibly leading to contact binaries) and increased separations (possibly leading to escape of the components from each other). An abundance of binary or contact-binary ECAs would suggest that subcatastrophic collisions play an important role in delivering material from the mainbelt into the inner solar system. Observations with the upgraded Arecibo and Goldstone instruments may permit reliable estimation of the abundance of "double" ECAs within a decade.

4. Cometary nuclei and large-particle clouds

Since a cometary coma is nearly transparent at radio wavelengths, radar is much more capable of unambiguous detection of a cometary nucleus than are optical and infrared methods (e.g., Kamoun *et al.*, 1982), and radar observations of several comets (Table I) have provided useful constraints on nuclear dimensions, spin vectors, and surface morphologies. The radar signature of comet IRAS-Araki-Alcock, which came within 0.03 AU of

Earth in 1983, was exceptionally informative (Harmon, Campbell, *et al.*, 1989; see also Goldstein *et al.*, 1984). The echoes (Fig. 12) show a narrow-band component from the nucleus as well as a much weaker broadband component attributed to large particles ejected mostly from the sunlit side of the nucleus. Models of the echoes suggest that the nucleus is very rough on scales larger than a meter, that its maximum overall dimension is

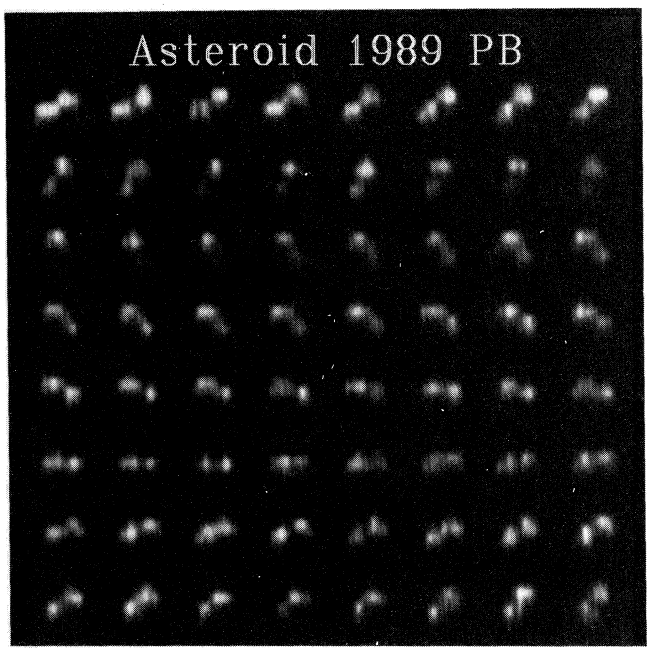

(a)

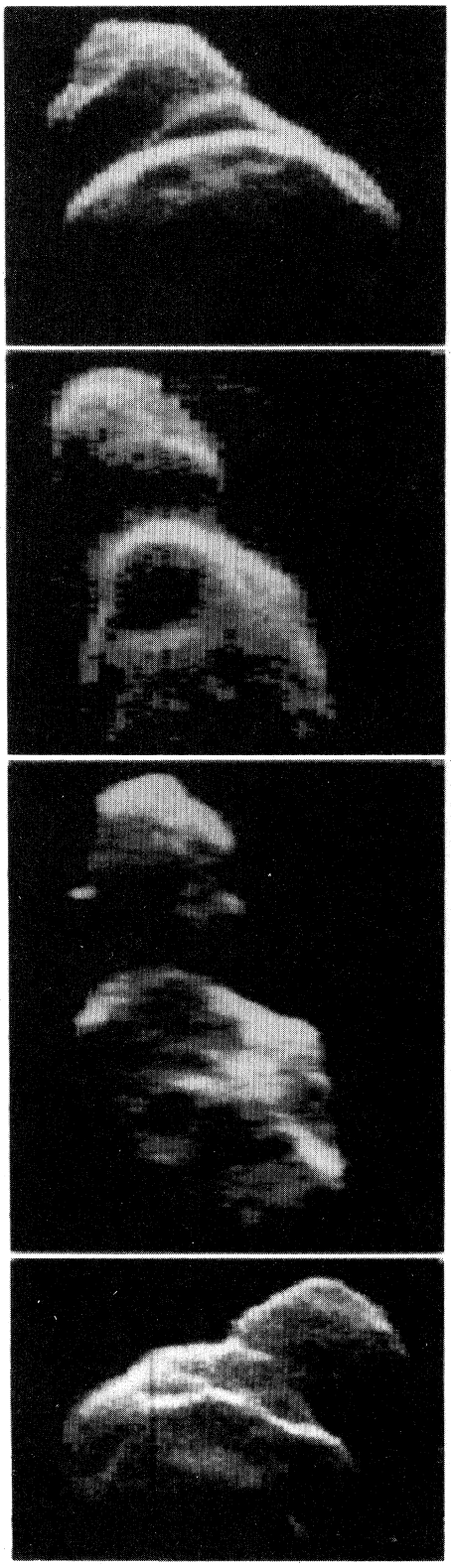

(b)

FIG. 11. Radar images of Earth-crossing asteroids: (a) This 64-frame Arecibo "movie" of 4769 Castalia (1989 PB) is to be read like a book (left to right in the top row, etc.). The radar lies toward the top of the page in the image plane, which probably is within a few tens of degrees of the asteroid's equator. In each frame, OC echo power (i.e., the brightness seem by the radar) is plotted vs time delay (increasing from top to bottom) and frequency (increasing from left to right). The radar illumination comes from the top of the screen; so parts of the asteroid facing toward the bottom are not seen in these images. The object, each of whose lobes is about a kilometer in diameter, is seen rotating through about 220° during the 2.5-h sequence. (Ostro, Chandler, Hine, *et al.*, 1990. Copyright 1990 by the AAAS.) (b) Goldstone radar images of asteroid 4179 Toutatis, made during the object's very close approach to Earth in December 1992, reveal two irregularly shaped, cratered objects about 2.5 and 1.5 kilometers in maximum dimension, probably in contact with each other. The four frames here were obtained on (from top to bottom) Dec. 8, 9, 10, and 13, with Toutatis an average of about 10 lunar distances from Earth. On each date, the asteroid was in a different orientation. The images sum data taken over intervals of 55, 14, 37, and 85 minutes, respectively. The radar illumination comes from the top of the page, so parts of each component facing toward the bottom are not seen in the images. The data's range (vertical) resolution is 0.125 μs (19 m). Doppler frequency increases from right to left. The distance equivalent of the frequency resolution (0.033 Hz) in each frame is a function of the instantaneous, apparent spin vector, which had not been estimated at the time these images were prepared; arbitrary conversions from hertz to kilometers were used here. The large crater in the Dec. 9 image is roughly 700 meters in diameter (JPL/NASA; Ostro *et al*, 1993).

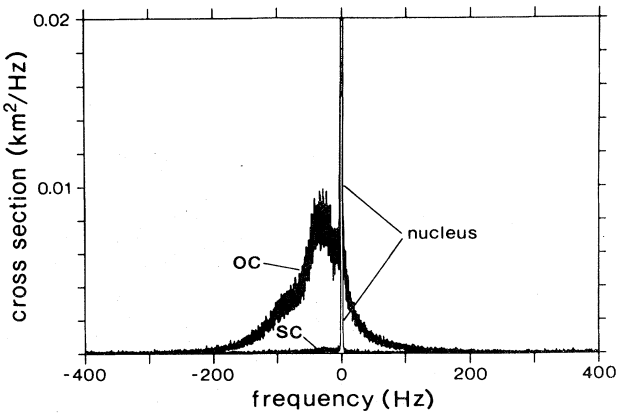

FIG. 12. Arecibo OC and SC echo spectra obtained for comet IRAS-Araki-Alcock, truncated at 2% of the maximum OC amplitude. The narrow-band echo from the nucleus is flanked by broadband echo from large (≥ 1 cm) particles in a 1000-km-radius cloud surrounding the nucleus (Harmon *et al.*, 1989).

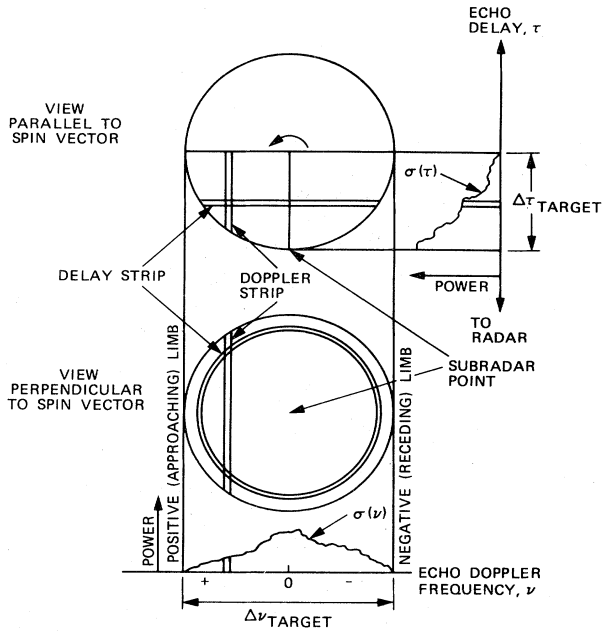

FIG. 13. Time-delay and Doppler-frequency resolution of the radar echo from a rotating spherical target.

within a factor of 2 of 10 km, and that its spin period is 2–3 days. The particles are probably several centimeters in size and account for a significant fraction of the particulate mass loss from the nucleus. Most of them appear to be distributed within ~1000 km of the nucleus, in the volume filled by particles ejected at several meters per second over a few days. The typical particle lifetime may have been this short, or perhaps the particle ejection rate was highly variable.

Radar spectra of comet Halley (Campbell, Harmon, and Shapiro, 1989) are broad and show no hint of a component as narrow as that expected from the nucleus, whose dimensions and spin vector were constrained by Giotto and Vega spacecraft images. The echo's bandwidth and radar cross section suggest that it arises predominantly from coma particles with radii >2 cm. The nondetection of Halley's nucleus implies a surface with a very low bulk density, consistent with arguments based on observed nongravitational motions and jet activity that the nucleus's bulk density may be as low as 0.1 g cm^{-3} (Whipple, 1987; Peale, 1989).

Future radar observations should be able to obtain high-resolution delay-Doppler images of cometary nuclei and any accompanying large-particle clouds. Despite the richness of the information about comet Halley gleaned from the spacecraft flybys, detailed knowledge of these objects' characteristics is lacking (A'Hearn, 1988) and the field of competing models is large. The apparently complex spin state of comet Halley (e.g., Belton *et al.*, 1991; Samarasinha and A'Hearn, 1991; Peale, 1992) raises questions about the homogeneity and mechanical properties of comet nuclei and motivates ground-based efforts to study the rotations of other comets. Radar astronomy, which "cut its teeth" with the determination of the rotations of Venus and Mercury three decades ago, is uniquely suited for this task.

D. Rotations of Venus and Mercury

In principle, echo bandwidth measurements obtained from a sufficiently wide variety of target directions can yield all three scalar components of the sidereal (intrinsic) spin vector $\boldsymbol{\omega}_s$. This capability follows from the fact that the apparent spin vector $\boldsymbol{\omega}$ is the vector sum of $\boldsymbol{\omega}_s$ and the contribution $\boldsymbol{\omega}_0=\dot{\mathbf{e}}\times\mathbf{e}$ arising from the changing direction of the target-to-radar unit vector $\mathbf{e}$. Variations in $\mathbf{e}$, $\dot{\mathbf{e}}$, and hence $\boldsymbol{\omega}_0$, all of which are known, lead to different values of $\boldsymbol{\omega}$, allowing determination of $\boldsymbol{\omega}_s$. In practice, this process is SNR limited and is coupled to estimation of the target's size, shape, and surface characteristics. For Mercury and Venus, high SNRs are available, size and shape have long been well known, and $\dot{\mathbf{e}}$ is substantial.

Radar determination of the spin vectors of these planets has exploited the simple relation between surface coordinates and delay-Doppler coordinates for a sphere (Fig. 13) and the consequently simple form of $\sigma(\tau,\nu)$, which for a target of radius a is (Simpson, 1973; see also Green, 1962)

$$\sigma(\tau,\nu)=(2a^2/\nu_0\tau_0)\frac{\sigma_0(\theta)}{[1-(\nu/\nu_0)^2-(1-\tau/\tau_0)^2]^{1/2}}\ . \tag{12}$$

Here

$$\tau_0=2a/c=\Delta\tau_{\rm tar}\ , \tag{12a}$$

$$\nu_0=\Delta\nu_{\rm tar}/2=(2a\omega F_{\rm tx}/c)(\cos\delta)\ , \tag{12b}$$

and

$$\sigma_0(\theta)=d\sigma/dA \tag{12c}$$

is the radar scattering law, with dA an element of surface area and θ the angle of incidence measured from the element's outward normal. On the plane of the sky, constant-delay contours project as circles, and constant-Doppler contours project as straight lines parallel to the spin vector. For any delay resolution cell, the greatest overlap with any Doppler resolution cell occurs on the apparent equator, where the Jacobian representing the transformation from spherical to delay-Doppler coordinates is singular (Shapiro, 1967). Consequently, the power spectrum within a delay cell has maxima at the extreme echo frequencies occurring at that delay (Fig. 14). The bandwidth between those frequencies is

$$B(\tau)=\Delta\nu_{\rm tar}[(2\tau/\tau_0)-(\tau/\tau_0)^2]^{1/2}\ . \tag{13}$$

Estimates of the limb-to-limb echo bandwidth $\Delta\nu_{\rm tar}=B(\tau_0)$ can, in principle, be used to constrain ω. However, the frequencies of the peaks in delay-gated spectra are more readily perceived than edge frequencies, so stronger constraints can be derived from estimates of $B(\tau)$. With enough SNR, still greater accuracy can be achieved by fitting a full delay-Doppler template for $\sigma(\tau,\nu)$ to images obtained for a variety of target directions. If compact surface features are prominent in the radar images, then observations of their delay-Doppler trajectories provide especially powerful leverage for spin vector refinement. Analysis of data accumulated over many apparitions (i.e., for Mercury and Venus, many inferior conjunctions) further shrinks uncertainties in estimates of ω, in part by eliminating certain systematic effects. These various approaches led to the first accurate determinations of the rotations of Venus and Mercury three decades ago (Fig. 15) and to improved results since then, as telescope sensitivity has increased.

Venus's rotation is retrograde with a 243-day sidereal period. Radar evidence for retrograde rotation with a period within 20% of the correct value was first presented by Carpenter (1964) and Goldstein (1964); see also Kotel'nikov *et al.* (1963). The period is remarkably close to the value, 243.16 d, characterizing a resonance with the relative orbits of Earth and Venus, wherein Venus would appear from Earth to rotate exactly four times between successive inferior conjunctions with the Sun. Nevertheless, results of Venus observations from the 1970s and 1980s (Shapiro, Campbell, and De Campli,

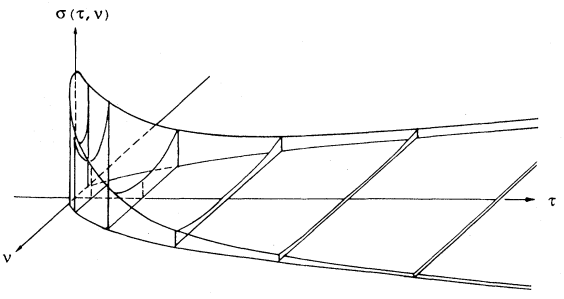

FIG. 14. Typical scattering function $\sigma(\tau,\nu)$ for a smooth sphere (after Fig. 9 of Simpson, 1973).

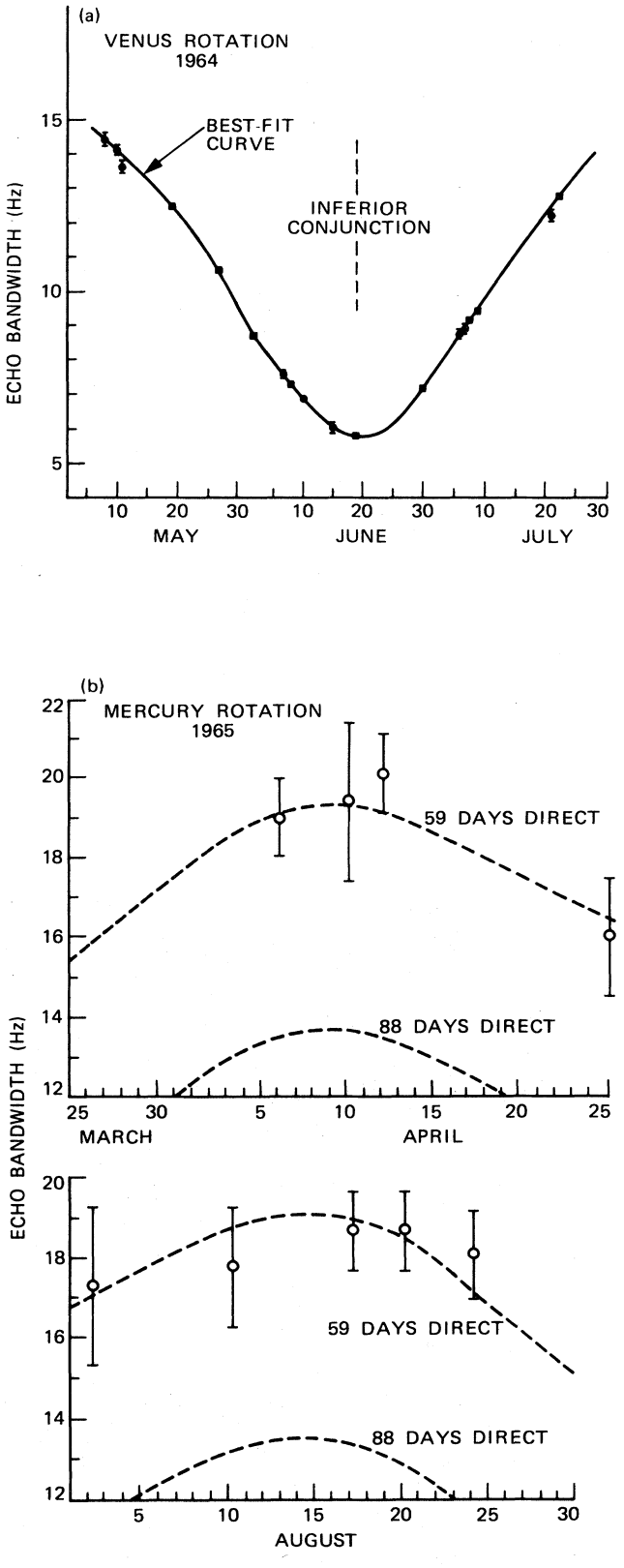

FIG. 15. Measurements of echo bandwidth used to determine the rotations of Venus and Mercury (Dyce, Pettengill, and Shapiro, 1967).

1979; Shapiro, Chandler, *et al.*, 1990; Slade *et al.*, 1990) and most recently an estimate (243.0185±0.0001 d) from analysis of control points in Magellan images (Davies *et al.*, 1992) have conclusively demonstrated nonresonance rotation. The difference between the period and the resonance value is several orders of magnitude too large for the spin to be librating about the resonance value. Moreover, the pole direction is several degrees from the normal to Venus's orbital plane and also is several degrees from the angular momentum vector of the solar system. To date, a satisfactory theory for the evolution of Venus's curious spin state is lacking.

For Mercury, long imagined on the basis of optical observations to rotate once per 88-day revolution around the Sun, radar measurements during two conjunctions in 1965 demonstrated direct rotation with a period, 59 d, equal to 2/3 of the 88-day orbital period (Pettengill and Dyce, 1965; Dyce *et al.*, 1967; Goldstein, 1971). Measurements of shadow positions in images taken during consecutive Mariner 10 spacecraft flybys (Klaasen, 1976) show the spin period to be within 0.01 d of the resonance value, 58.6457 d. The spin-orbit resonance is such that during two Mercury years, the planet rotates 3 times with respect to the stars but only once with respect to the Sun; so a Mercury-bound observer would experience alternating years of daylight and darkness.

Tidal dissipation apparently slowed Mercury's initially rapid rotation until it was captured into the current nonsynchronous but commensurate state (Colombo, 1965; Colombo and Shapiro, 1966; Goldreich and Peale, 1966; Burns, 1976). A molten core would have greatly enhanced the capture probability (Counselman, 1969). Strong constraints on the core and on the tidal dissipation function Q follow from Mercury's having passed through the resonance with a 44-day rotation (Peale, 1988, and references therein) and from the discovery by the Mariner 10 spacecraft that Mercury possesses an intrinsic global magnetic field (see, for example, Connerney and Ness's 1988 review).

Mercury's spin is understood as being in a so-called Cassini state, with the pole fixed in the orbit frame of reference at a constant, nonzero obliquity (the angle between the spin and orbital angular momenta) while that frame precesses about the normal to the plane of the solar system (Peale, 1969). Mercury's current obliquity is no more than a few degrees (Gault *et al.*, 1977). Precise determination of the obliquity, the lowest gravitational harmonics, and the physical librations about the commensurate rotation period could reveal the extent of any liquid core (Peale, 1976, 1988). A Mercury-orbiting spacecraft could make these measurements and could also reduce the uncertainty in the contribution of the spin-orbit coupling to the perihelion advance of Mercury's orbit through determination of the difference between the planet's equatorial moments of inertia (Shapiro, 1980). Proposals for a dedicated Mercury mission are compelling on many grounds (Stern and Vilas, 1988). Until they reach fruition, radar closure measurements can improve upon available estimates of Mercury's figure and spin vector at the same time that altimetry and

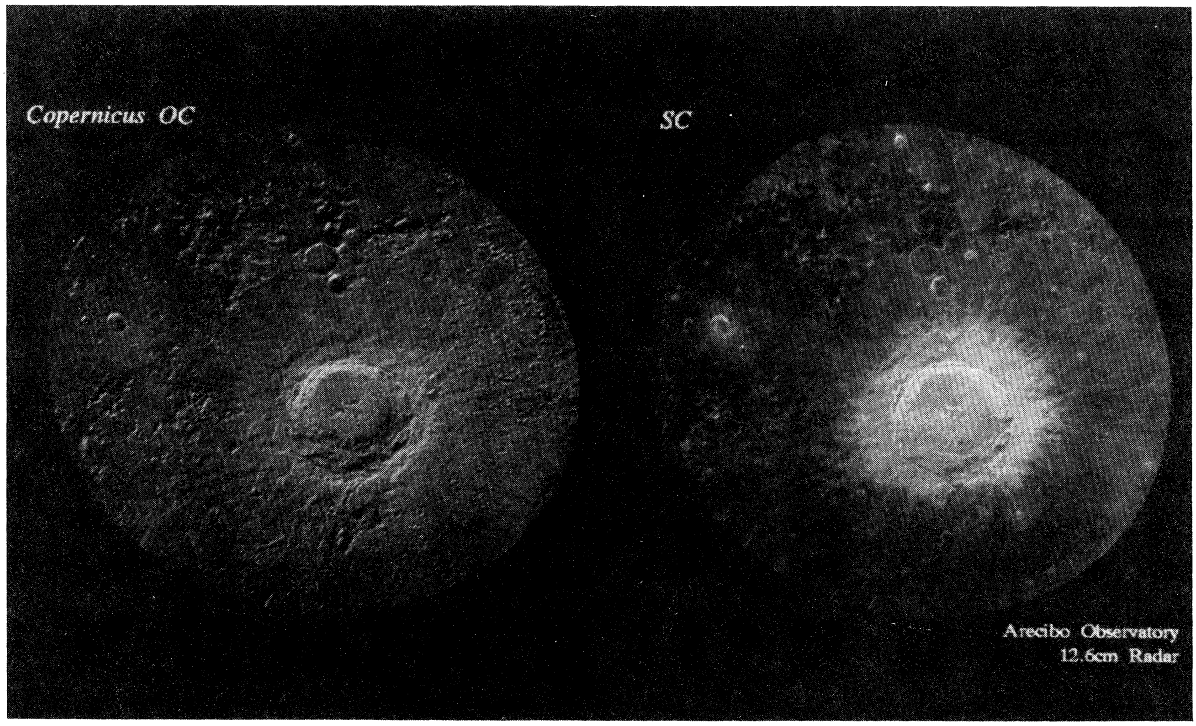

FIG. 16. Arecibo OC and SC delay-Doppler maps of the 93-km-diameter lunar crater Copernicus (10° N, 20° W), courtesy of N. J. S. Stacy and D. B. Campbell. The resolution is 900 m.

dual-polarization reflectivity mapping provide unique information about the large-scale global properties of the surface, only half of which was imaged by Mariner 10.

E. Radar mapping of planetary surfaces

1. Overview of techniques and results

The term "radar image" usually refers to a measured distribution of echo power in delay, Doppler, and/or angular coordinates. The term "radar map" usually refers to a display in suitable target-centered coordinates of residuals with respect to a model that parametrizes the target's average scattering properties and possibly its size, shape, apparent spin, and motion with respect to the prediction ephemerides. Thorough descriptions of ground-based radar imaging/mapping experiments are available for Mercury (Harmon and Slade, 1992; Slade *et al.*, 1992), Venus (Campbell and Burns, 1980; Jurgens *et al.*, 1988; Campbell, Head, *et al.*, 1989), Mars (Muhleman *et al.*, 1991; Harmon, Slade, and Hudson, 1992; Simpson *et al.*, 1992), the Moon (Stacy, 1993), and the icy Galilean satellites (Ostro *et al.*, 1992).

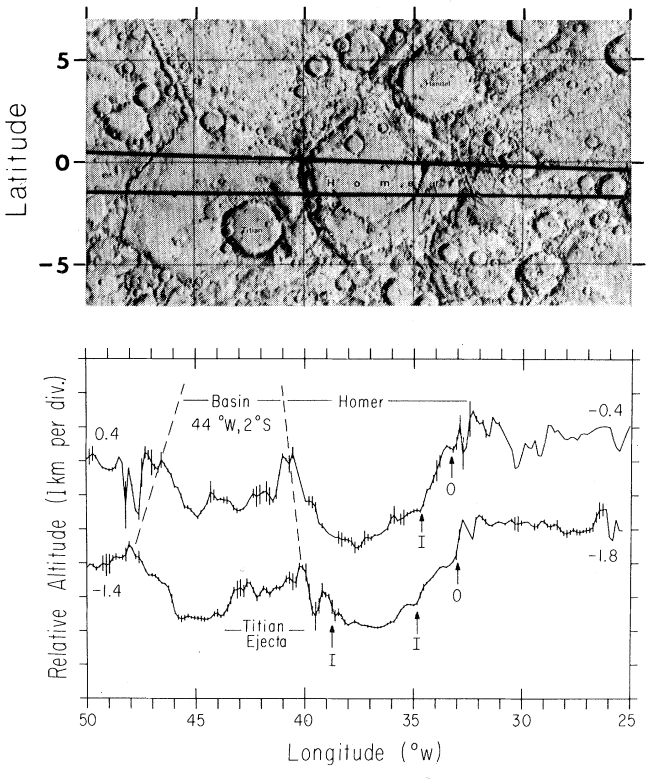

FIG. 17. Mercury altitude profiles (bottom) showing topography across Homer Basin and a large, un-named basin to the west, estimated from observations whose subradar tracks are shown on the shaded-relief map (top). Broken lines indicate approximate locations of the basin rims as seen in Mariner 10 images. Arrows locate Homer's inner/outer (*I*/*O*) basin rings (Harmon, Campbell, and Bindschadler *et al.*, 1986).

As noted earlier, cw observations yield a one-dimensional image, and delay-Doppler observations yield a two-dimensional image with a north/south ambiguity. The N/S ambiguity can be avoided if the radar beam is smaller than the target's angular radius, as with lunar observations from Earth (Fig. 16) and side-looking radar observations from spacecraft. For Venus and Mercury, whose angular radii never exceed several tens of seconds of arc, one can point the antenna slightly north or south of the target, so as to place a null of the illumination pattern on the undesired hemisphere. If two receiving antennas are available, ambiguous cells can be separated interferometrically (e.g., Hagfors and Campbell, 1973). With only a single receiving antenna, one can use delay-Doppler images as a function of rotation phase at one or more nonzero subradar latitudes to estimate the radar reflectivities of any two ambiguous cells. This is possible because each cell follows a different delay-Doppler-phase trajectory (e.g., Goldstein and Rumsey, 1972). If the phase coverage is sufficiently thorough, one can use a similar approach with cw spectra (Hudson and Ostro, 1990). This Doppler-mapping technique has been applied to Mars (Harmon, Slade, and Hudson, 1992), the icy Galilean satellites (Hudson, 1991; Ostro *et al.*, 1992), and even the Moon (Hagfors *et al.*, 1968; Thomson and Ponsonby, 1968), for which libration-induced wander of the apparent spin vector provides the effective geometric leverage.

If multiple interferometric baselines are provided either instantaneously by multiple antennas or over the course of an observing period by the changing projection of a two-antenna baseline, then unambiguous full-disc images can be made via direct angular resolution of the echoes. This technique has been implemented by using the Goldstone 70-m antenna as a cw transmitter and the Very Large Array as a synthetic aperture receiver (e.g., Muhleman *et al.*, 1991). The 27-antenna VLA constitutes a 351-baseline interferometer whose smallest synthesized beam at 3.5 cm provides resolutions of roughly 80, 40, and 70 km for Mercury, Venus, and Mars at closest approach. (The finest resolutions in published ground-based delay-Doppler maps of those planets are approximately 15, 1, and 40 km, respectively, but the maps cover small fractions of the surface at such fine resolutions.) The Goldstone-VLA system has achieved marginal angular resolution of mainbelt asteroid echoes (de Pater *et al.*, 1992) and could readily image any large-particle comet clouds as radar detectable as the one around comet IRAS-Araki-Alcock. Imaging of small asteroids and comet nuclei is impaired by the VLA's maximum baseline, coarse spectral resolution (> 380 Hz), and an inability to accommodate time-modulated wave forms.

With multiple interferometric baselines, delay-Doppler measurements can yield altimetric maps as well as reflectivity maps (e.g., Shapiro, Zisk, *et al.*, 1972; Goldstone *et al.*, 1978; Jurgens *et al.*, 1980), but most radar altimetry to date has used single-antenna ranges. Topographic profiles like those of Mercury and Mars in Figs.

17 and 18 have enhanced the interpretability of radar and optical images of those planets (e.g., Roth *et al.*, 1980, 1989; Kotel'nikov *et al.*, 1983; Harmon, Campbell, *et al.*, 1986; Zisk *et al.*, 1992).

Longitude/latitude coverage strengthens any radar mapping technique by helping to distinguish among the factors that might be responsible for features: surface electrical properties, viewing geometry, and roughness at various scales. Similarly, it is desirable to obtain maps in two orthogonal polarizations [opposite circular (OC) and same circular (SC), or opposite linear (OL) and same linear (SL)] to clarify the scattering process.

2. Scattering models and surface properties

At centimeter-to-meter wavelengths, echoes from the Moon and the inner planets are dominated by a strong glint from the subradar region near the center of the target's disk, in the polarization (OC or SL) expected for coherent backreflections from smooth, normally oriented surface elements. The scattering law for this so-called quasispecular component of the echo can, under assumptions like perfect conductivity and geometric optics, be related to the slope probability density function $p(\theta)$ and the rms slope s_0 by (Simpson and Tyler, 1982; Tyler

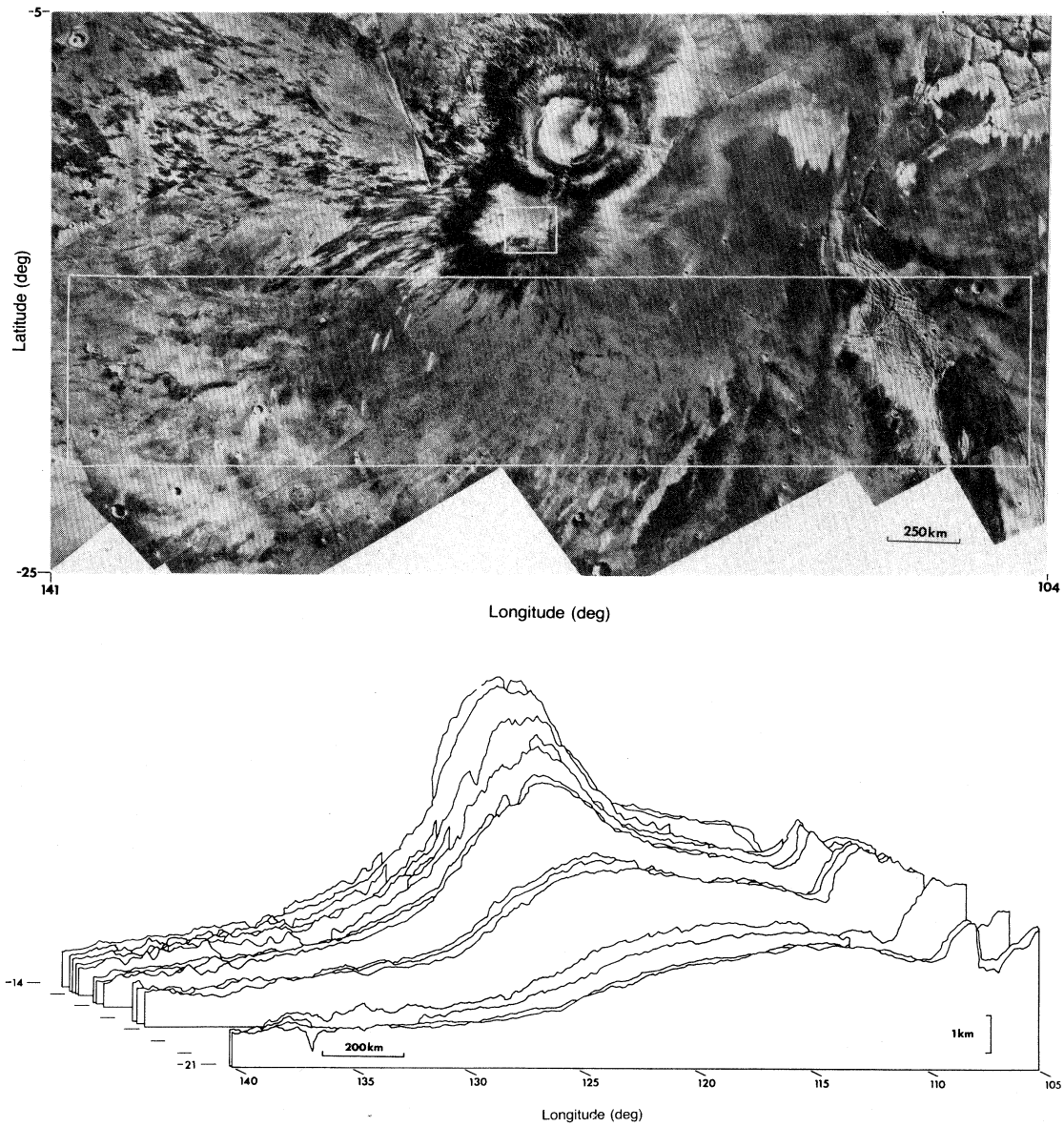

FIG. 18. Topographic contours for the southern flank (large rectangle) of the Martian shield volcano Arsia Mons, obtained from radar altimetry (Roth *et al.*, 1980).

et al., 1992)

$$p(\theta)=2\sigma_0(\theta)\cos\theta \tag{14}$$

and

$$s_0^2=\langle\tan^2\theta_{\rm rms}\rangle=\int_0^{\pi/2}\tan^2\theta\, p(\theta)\sin\theta\, d\theta\ . \tag{15}$$

Simpson (1973) compared several methods for modeling wave scattering from mildly rough surfaces (physical-optics scalar, physical-optics vector, and geometric optics). A more recent review is given by Ogilvy (1991); see also Kim and Rodriguez (1992) and references therein.

Examples of scattering laws applied most widely and used in planetary radar astronomy are the Hagfors law,

$$\sigma_0(\theta)\sim s_0^{-2}(\cos^4\theta+s_0^{-2}\sin^2\theta)^{-3/2}\ , \tag{16}$$

which assumes a Gaussian height distribution and an approximately exponential surface autocorrelation function (Hagfors, 1964); and the Gaussian law,

$$\sigma_0(\theta)\sim[s_0^{-2}\exp(-s_0^{-2}\tan^4\theta)]\cos^{-4}\theta\ , \tag{17}$$

which assumes a Gaussian form for both the height distribution and the surface autocorrelation function, and for which s_0 represents the adirectional rms slope in radians (Beckmann, 1963). With the Hagfors law, s_0 is interpreted as referring to a version of the surface that has been smoothed by a wavelength-scale filter (Hagfors, 1967); it pertains to horizontal scales determined in part by the height distribution (Tyler, 1976; Bahar *et al.*, 1983). For surfaces consisting of two or more discrete terrain types, each with a different slope distribution, radar measurements may underestimate s_0 (McCollom and Jakosky, 1993). The backscatter gain g (Sec. III.C.1) is approximately $1+s_0^2$ for the quasispecular part of the echo from a spherical target.

Radar estimates of slopes on the Moon and inner planets average about 7° at decimeter wavelengths. Surfaces characterized by such shallow slopes have been described as "gently undulating." However, for many terrains on those bodies, the spectra show only a subdued central peak, indicating an abundance of steep slopes or lots of wavelength-scale structure near the surface (e.g., Fig. 19). For mainbelt asteroids, steep slopes apparently characterize the surfaces of even the largest objects, many of which may possess extreme topographic relief or irregular shapes (e.g., Fig. 20).

Lunar estimates of s_0 increase with decreasing wavelength, from ~4° at 20 m to ~8° at 10 cm and ~33° at 1 cm. At optical wavelengths, the Moon's scattering law is entirely diffuse due to the fine-grained complexity of the regolith. At decimeter wavelengths the fraction of echo power that is diffusely scattered is ~0.3 for the Moon, Mercury, and Venus, but 2 to 3 times higher for Mars. That fraction, $A_{\rm dif}$, can be determined by assuming that all the SC echo is diffuse and then modeling the OC image with a composite scattering law of the form (e.g., Evans and Pettengill, 1963; Lipa and Tyler, 1976; Harmon, Campbell, and Ostro, 1982)

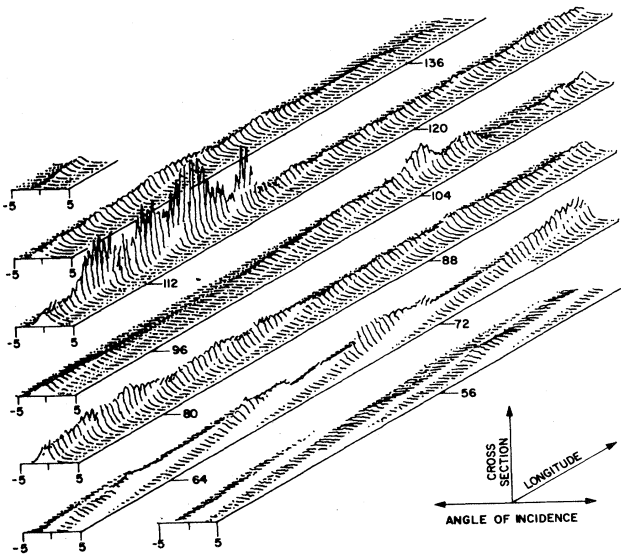

FIG. 19. Mars 13-cm, OC power spectra as a function of longitude obtained along a subradar track at 16° S latitude. The most sharply peaked spectra correspond to the smoothest regions (i.e., the smallest rms slopes). Downs *et al.*, 1975.

$$\sigma_0(\theta)=A_{\rm dif}\sigma_{\rm dif}+(1-A_{\rm dif})\sigma_{\rm qs}(\theta)\ , \tag{18}$$

where $\sigma_{\rm qs}$ is one of the quasispecular laws and $\sigma_{\rm dif}\sim\cos^n\theta$. Estimated values of n usually fall between unity (geometric scattering, which describes the optical appearance of the full Moon) and 2 (Lambert scattering). Another expression that encompasses quasispecular and diffuse scattering components is a function derived heuristically by Muhleman (1966),

$$\sigma_0(\theta)\sim\cos\theta(\alpha\cos\theta+\sin\theta)^{-3}\ , \tag{19}$$

where α is an arbitrary roughness parameter.

Physical interpretations of the diffusely scattered echo employ information about albedo, scattering law, and polarization to constrain the size distributions, spatial densities, and electrical properties of wavelength-scale rocks near the surface (e.g., Pollack and Whitehill, 1972; Ulaby *et al.*, 1982; Harmon and Ostro, 1985; Elachi, 1987; Muhleman *et al.*, 1991; Tryka and Muhleman, 1992). This work draws on the same theory of multiple light scattering (e.g., van de Hulst, 1980; Chandrasekhar, 1960) applied to radiative transfer problems in other astrophysical contexts, including optical scattering from planetary regoliths (Hapke, 1993) and atmospheres (Hansen and Travis, 1974).

Bistatic radar studies that employ transmission by an orbiting spacecraft and Earth-based reception of echoes have been carried out for the Moon and Mars and have provided estimates of slope and dielectric constant for regions beyond the possible coverage of ground-based subradar tracks. Analyses of the lunar observations indicated that fundamental differences in scattering among

locales in the maria cannot be accommodated by any single law (Tyler and Simpson, 1970), spurring efforts to extract slope probability density functions from bistatic echoes in a manner free from restrictions on a model law's functional form (Parker and Tyler, 1973; Parker, 1974). Tyler (1979) showed that wavelength-dependent values of rms slopes in the maria, estimated from bistatic, dual-wavelength data, can be understood in terms of the variance of the distribution of surface curvature, which he estimated from photogrammatically determined heights. Wavelength dependence of quasispecular parameters has also been observed for Mars, with surfaces appearing rougher and less reflective at 3.5 cm than at 13 cm (Harmon, Slade, and Hudson, 1992).

3. The radar exploration of Venus

Radar has revealed Venus in progressively finer detail during the past three decades. Ground-based images and altimetry led initially to the discovery of elevation variations (e.g., Campbell, Dyce, *et al.*, 1972) and reflectivity features (e.g., Goldstein, 1965; Jurgens, 1970) and then to tentative geologic identification of those features (e.g., Campbell, Head, *et al.*, 1983, 1984; Burns and Campbell, 1985). Eventually, images with resolution as fine as that in Fig. 21 permitted inferences about the surface's age and the relative importance of volcanism, tectonics, and impact cratering (e.g., Campbell, Head, *et al.*, 1989; Campbell, Senske, *et al.*, 1991).

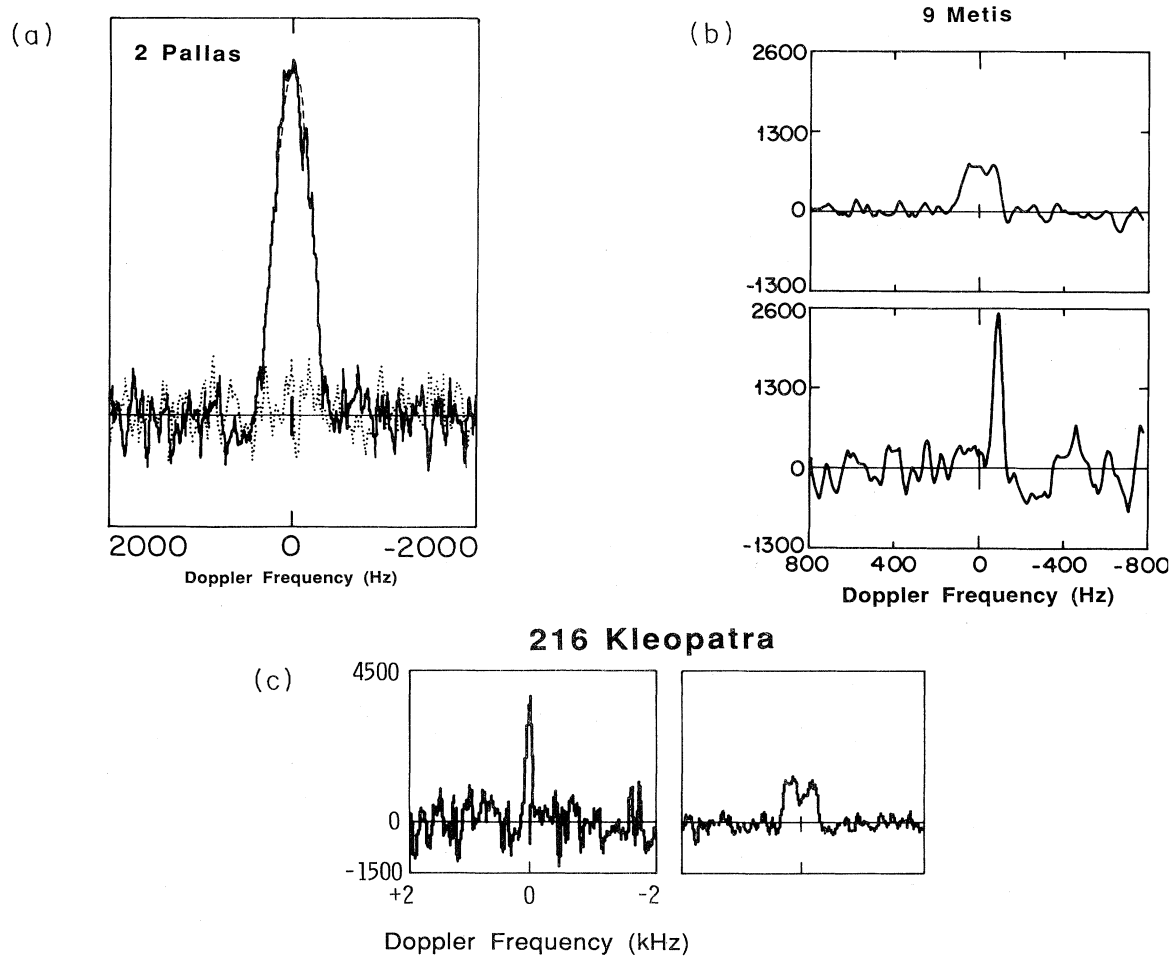

FIG. 20. Echo spectra of three mainbelt asteroids from Arecibo 13-cm observations. Echo power density is plotted on a different linear scale for each object. Vertical bars at (0,0) show ± 1 standard deviation of the noise. (a) OC and SC spectra (solid and dotted curves) obtained for 2 Pallas ($D \sim 523$ km). The circular polarization ratio μ_C is 0.05 ± 0.02, indicating an extremely smooth surface at decimeter scales. However, the Gaussian model [dashed curve; see Eq. (17)] fit to the OC spectrum indicates that the surface is very rough at meter-to-kilometer scales, with rms slopes $\sim 25°$ (Ostro, Campbell, and Shapiro, 1985; copyright 1990 by the AAAS). (b) OC spectra for 9 Metis ($D \sim 170$ km) from data obtained by Ostro, Campbell, and Shapiro (1985). The top curve is a 15-run sum spanning 300° of rotational phase. The bottom curve, from one of those runs, spans $\sim 28°$; its asymmetry may be due to a huge flat area on the asteroid's receding side, oriented nearly normal to the line of sight during that run. (c) OC spectra for 216 Kleopatra ($D \sim 140$ km) at rotational phases $\sim 90°$ apart (Ostro, Campbell, and Shapiro, 1986). The bandwidth variation indicates a very elongated pole-on silhouette. The bifurcated spectrum supports Weidenschilling's (1980) conjecture that this M-class object is dumbbell-shaped.

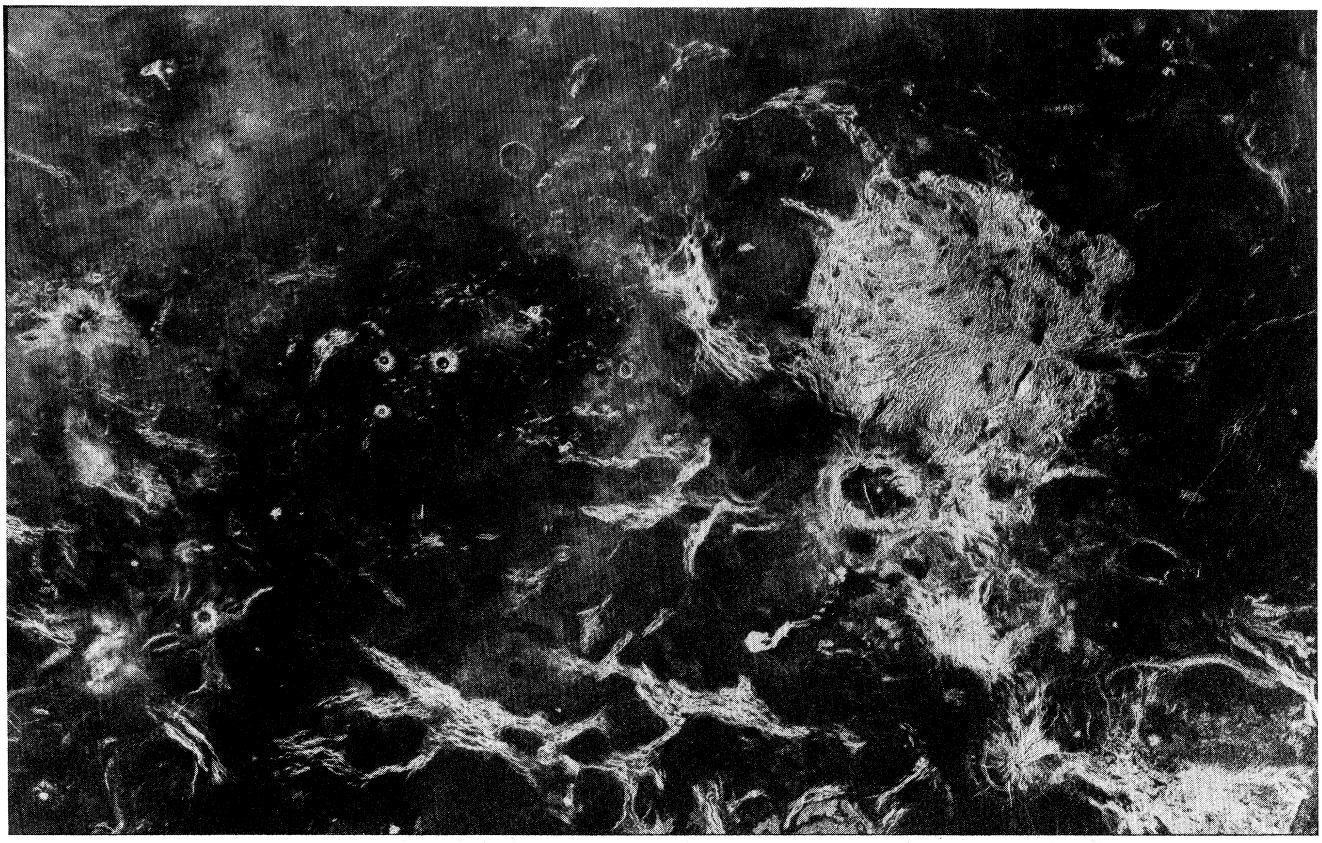

FIG. 21. Arecibo OC delay-Doppler map of Venus. In the middle of the right half of the figure is the bright 1200-km-wide Alpha Regio, a complex of intersecting ridges. Just south of Alpha is the 300-km-diameter circular feature Eve. The three prominent craters in the middle of the left half of the figure are seen close-up in Fig. 22(d). Courtesy of D. B. Campbell.

Beginning in 1979, the Pioneer Venus Spacecraft Radar Experiment gave us our first global look at the planet's distributions of topography, radar reflectivity, and surface slopes (e.g., Pettengill, Eliason, *et al.*, 1980). During the 1980s, maps having sparse coverage but resolution down to ~2 km were obtained from the Soviet Venera 15 and 16 orbiters (e.g., Barsukov *et al.*, 1986) and from ground-based observations with improved systems. In 1990 the Magellan spacecraft entered Venus orbit and for two years explored the planet with a single scientific instrument operating as a radar imager, an altimeter, and a thermal radiometer (Pettengill, Ford, *et al.*, 1991). Magellan's imaging resolution (~100 m) and altimetric resolution (5 to 100 m) improve upon previous measurements by an order of magnitude. Ultimately, analysis of Magellan data is expected to help resolve such key issues as the interior heat budget, mechanisms of heat transport through the lithosphere, crustal formation processes, global tectonic styles, and scales of mantle dynamics (Solomon and Head, 1991).

Figure 22 is a gallery of Magellan radar views of Venus. The formation and evolution of the planet's cratered and tectonically deformed surface have clearly been dominated by widespread volcanism, whose legacy includes pervasive volcanic planes, thousands of tiny shield volcanoes, monumental edifices, sinuous lava flow channels, pyroclastic deposits of material thrown out by explosive eruptions, and pancakelike domes (Head *et al.*, 1991). The nature and distribution of volcanic features suggest they are the surface manifestation of mantle plumes or hot spots (Head *et al.*, 1992). The superposition of volcanic and elaborate tectonic signatures has recorded a history of episodic crustal deformation and volcanism. Diverse responses to mantle dynamic processes are evident in deformational features of various styles and spatial scales (Solomon *et al.*, 1991, 1992). Terrestrial plate tectonics, in which rigid plates 10^3 to 10^4 km across are bounded by narrow deformational zones, are not seen on Venus; instead, deformational zones 10 to 10^2 km wide are separated by relatively undeformed 10^2-km blocks (Solomon *et al.*, 1992).

The radar-bright ejecta blankets around Venus craters are reminiscent of the radar signatures of lunar craters (e.g., Fig. 16 and Thompson *et al.*, 1981). The multilobed, asymmetrical appearance of many large craters presumably results from atmospheric breakup of the projectile before impact (Phillips *et al.*, 1991; Schaber *et al.*, 1992). The paucity of impact craters smaller than 25 km and the lack of any as small as a few kilometers attest to the protective effect of the dense Venus atmosphere,

which has prevented formation of 98% of the 2-to-35-km craters that would have formed in the absence of an atmosphere. The crater distribution suggests that resurfacing of the planet erased the cratering record 0.5×10^9 y ago (Phillips *et al.*, 1992).

Among the youngest surface markings are parabolic, crater-related features that may have arisen from deposits of small particles injected into the atmosphere during impact and transported by zonal winds (Campbell, Stacy, *et al.*, 1992). Other features suggest slow modification of

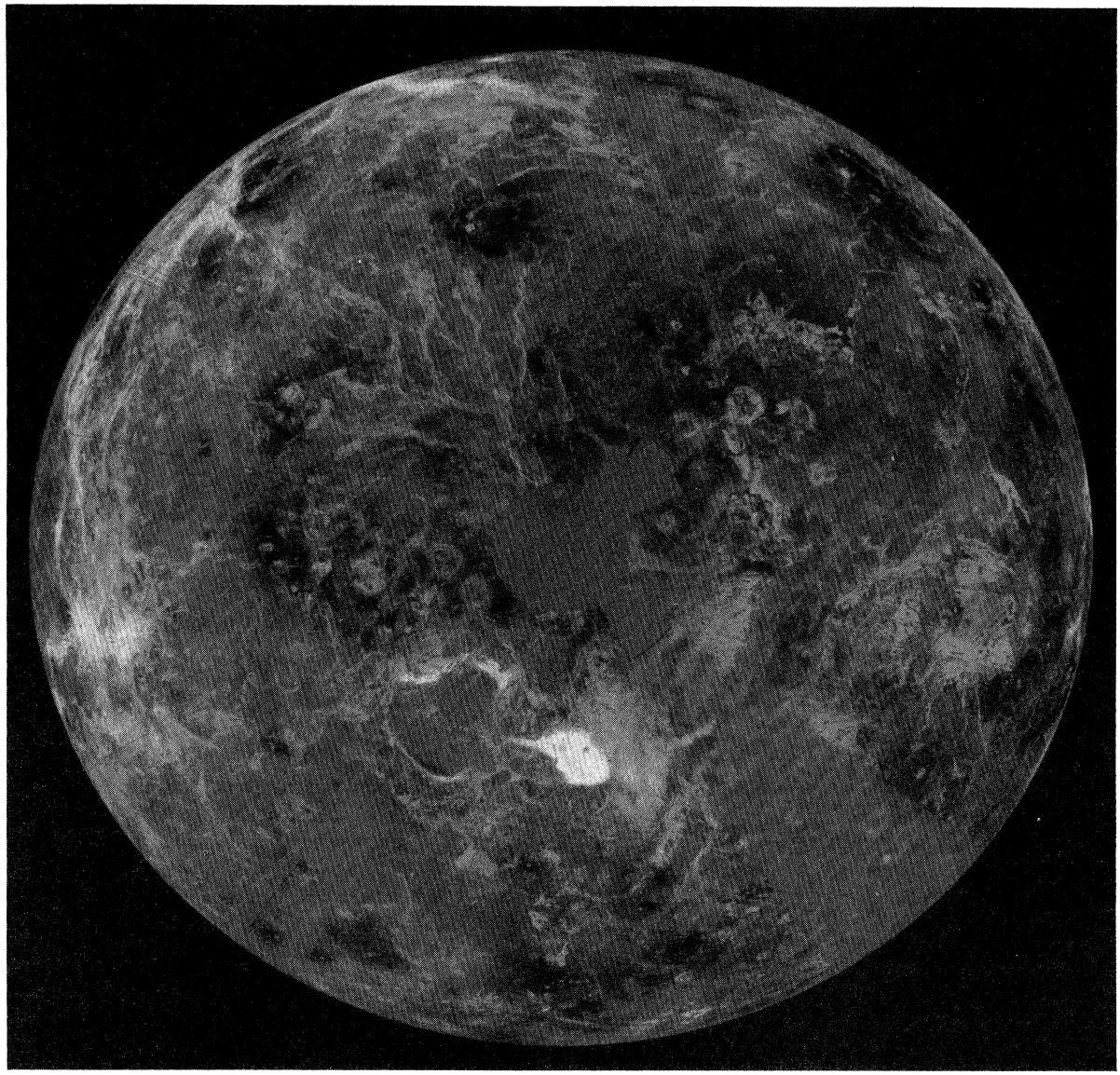

(a)

FIG. 22. Magellan 13-cm SL radar maps of Venus: (a) Northern-hemisphere projection of mosaics. The north pole is at the center with 0° and 90° E longitudes at the 12 and 9 o'clock positions. Gaps use Pioneer Venus data or interpolations. The bright porkchop-shaped feature is Maxwell Montes, a tectonically produced mountain range first seen in ground-based images. (b) 120-m-resolution map of Cleopatra, a double-ringed impact basin on the eastern slopes of Maxwell Montes. The diameter of the outer ring is about 100 km. (c) A 350-km-wide portion of the Atla region of Venus's southern hemisphere. Several types of volcanic features are crisscrossed by numerous superimposed, and hence more recent, surface fractures. Various flower-shaped patterns formed from linear fissures or lava flows emanate from circular pits. Near the center, a 10-by-20-km collapse formation is drained by a 40-km lava channel. (d) Mosaic of part of Lavinia showing three large craters, with diameters ranging from 37 to 50 km, that were discovered in Arecibo images; see Fig. 21. Note the abundant fractured planes and numerous small volcanic domes. (e) Pancakelike volcanic domes located southeast of Alpha Regio. These ~25-km-diameter edifices probably formed from extrusion of viscous magmas from central conduits (Ford *et al.*, 1991; JPL/NASA).

the surface by physical and chemical interaction with the atmosphere (Arvidson *et al.*, 1992; Greeley *et al.*, 1992). Overall, the Magellan data set reveals striking diversity in the planet's topography (Ford and Pettengill, 1992) and radar scattering properties (Tyler *et al.*, 1991, 1992), with high-reflectivity, low-emissivity surfaces occurring preferentially at high elevations (Pettengill, Ford, and Wilt, 1992).

4. Anomalous features on Mars and Mercury

Maps of Mars from Goldstone-VLA images (Fig. 23) and monostatic echo spectra (Fig. 24) show several SC enhancements associated with individual volcanoes in Tharsis in addition to a 2000-km-long band that cuts an extremely low-reflectivity swath across that region (Muhleman *et al.*, 1991; Harmon, Slade, and Hudson, 1992). The radar darkness of that so-called Stealth feature probably arises from an underdense, unconsolidated blanket of pyroclastic deposits at least 1 meter deep. The high 13-cm values of μ_c in Tharsis probably are due to the extreme decimeter-scale roughness of lava flows; that 3.5-cm values are lower is attributed to burial of the rough surfaces under a lossy dust mantle several decimeters deep. Regions of extreme small-scale roughness in the Elysium volcanic region are evident in monostatic spectra and random-code delay-Doppler images (Fig. 25). It seems that neither of the rock-strewn Viking landing sites is nearly as rough as Elysium or Tharsis.

The strongest SC feature in Mars maps is the residual south polar ice cap. Surprisingly, the first full-disc radar portraits of Mercury (Figs. 26 and 27) also show anomalously bright polar features (Slade *et al.*, 1992; see also Harmon and Slade, 1992). Mercury's south polar feature appears to be mostly confined to the floor of the 155-km crater Chao Meng-Fu. Similarities between the radar

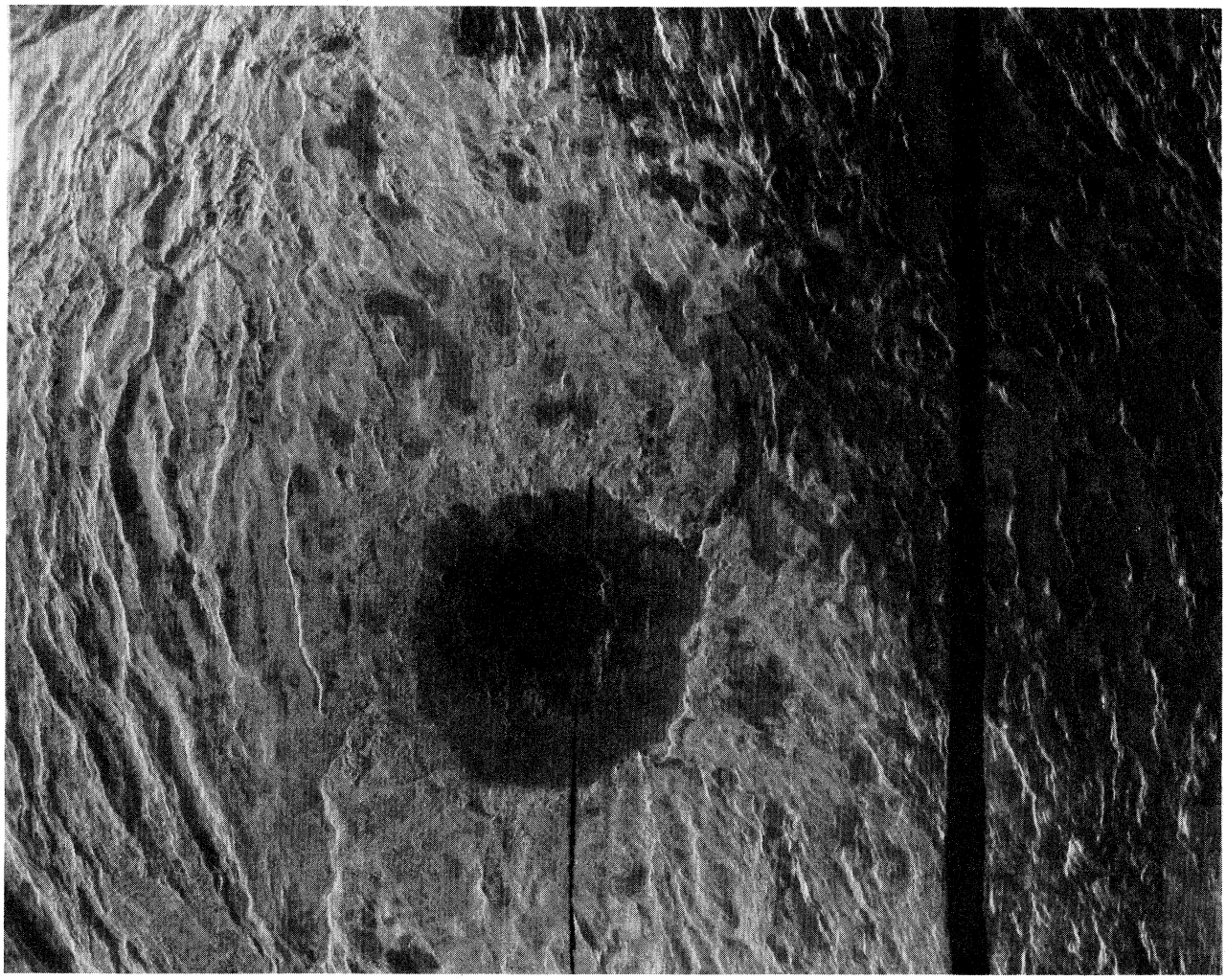

(b)

FIG. 22. (*Continued*).

scattering properties of the Mars and Mercury polar anomalies and those of the icy Galilean satellites support the hypothesis that Mercury's polar features are deposits of water ice inside high-latitude craters and other concavities perpetually shaded from sunlight because of Mercury's low obliquity (Paige *et al.*, 1992). The angle between the orbital planes of Mercury and Earth is 7°, so portions of permanently shadowed regions are visible from Earth. Water ice is thought to be stable against evaporation at temperatures lower than 112 K; temperatures several tens of kelvins lower may exist inside high-latitude craters and perhaps also beneath at least 10 cm of optically bright regolith (Wood *et al.*, 1992). Of course, the ice-cap hypothesis prompts questions about sources, sinks, and transport of water on Mercury (Butler *et al.*, 1993).

F. The icy Galilean satellites

1. Radar signatures

Among all the radar-detected planetary bodies in the solar system, Europa, Ganymede, and Callisto have the most unusual radar properties. Their reflectivities great-

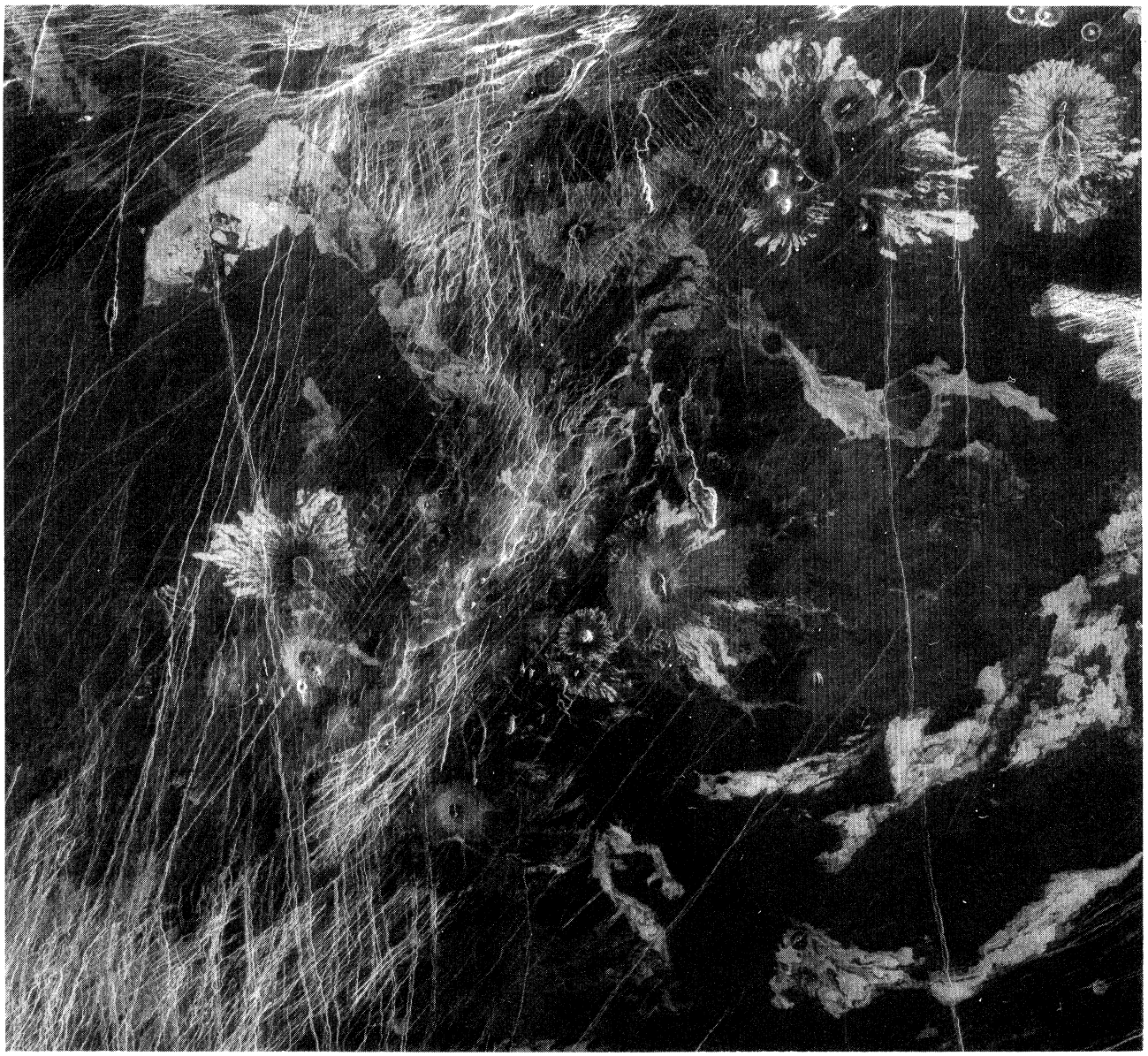

(c)

FIG. 22. (*Continued*).

ly exceed those of the Moon and inner planets (Figs. 6 and 28). The radar and optical albedos and estimates of fractional water frost coverage increase in the order Callisto, Ganymede, Europa; thus, the presence of water ice has long been suspected of playing a key role in the radar signatures even though ice's relatively low dielectric constant makes it less intrinsically reflective than silicates. In spite of the satellites' smooth appearances at the several-kilometer scales of Voyager high-resolution images, a diffuse scattering process and hence a high degree of near-surface structure at centimeter-to-meter scales are suggested by broad spectral shapes and large linear polarization ratios ($\mu_L \sim 0.5$).

The most peculiar aspect of the satellites' echoes is their circular polarization ratios, which exceed unity. That is, in contrast to the situation with other targets, the scattering largely preserves the handedness, or helicity, of the transmission. Mean values of μ_C for Europa, Ganymede, and Callisto are about 1.5, 1.4, and 1.2, respectively. Wavelength dependence in μ_C and $\hat{\sigma}_{OC}$ is negligible from 3.5 to 13 cm and, at least for μ_C, possibly through 70 cm. Significant features are present in the echo spectra and, in a few cases, correspond to geologic features imaged by the Voyager spacecraft.

Ostro *et al.* (1992) summarized the history of radar observations of the satellites, reported results of Arecibo/Goldstone observations during 1987–1991, and reviewed efforts to understand the electromagnetic scattering process responsible for the unusual echoes. The icy satellites' echoes are due not to external surface

(d)

FIG. 22. (*Continued*).

reflections but to volume scattering from within the satellites' regoliths. The high radar transparency of ice compared with that of silicates permits deeper radar sounding, longer photon path lengths, and higher-order scattering from regolith heterogeneities. Consequently, radar is seeing Europa, Ganymede, and Callisto in a manner in which the Moon has never been seen.

Ostro and Shoemaker (1990) outlined geological explanations for the satellites' radar signatures that considered regolith formation theory, ice physics, and the scattering models that prevailed in the 1980s: mode-decoupled refraction scattering (Hagfors *et al.*, 1985; Eshleman, 1986a) and multiple, total-internal reflection (Goldstein and Green, 1980; Eshleman, 1986b). They argued that prolonged meteoroid bombardment probably has led to the development on each of the icy satellites of regoliths similar in structure and particle-size distribution to the lunar regolith, and that diverse heterogeneities in bulk density and hence refractive index are likely to be found within the icy regoliths. They suggested that a variety of subsurface structures and scattering processes might share responsibility for the strange radar echoes.

2. Coherent backscattering

As suggested by Hapke (1990), the satellites' radar behavior apparently involves the coherent backscatter effect, which has been observed in the scattering of electrons in disordered metals (reviewed by Lee and Ramakrishnan, 1985) and more recently in the scattering of photons from weakly absorbing, disordered random media (e.g., van Albada and Lagendijk, 1985; Wolf and Maret, 1985; Etemad *et al.*, 1986; MacKintosh and John,

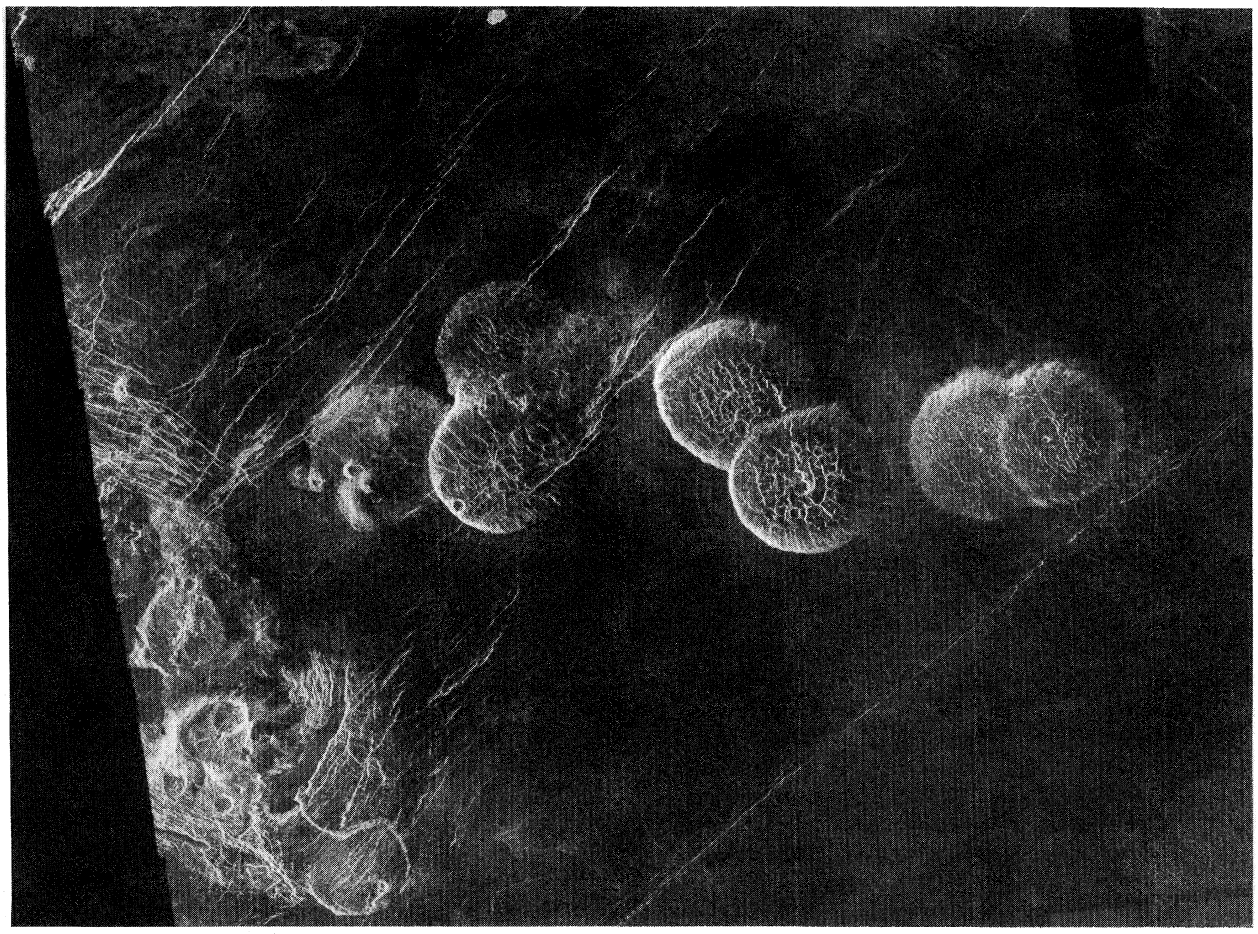

(e)

FIG. 22. (*Continued*).

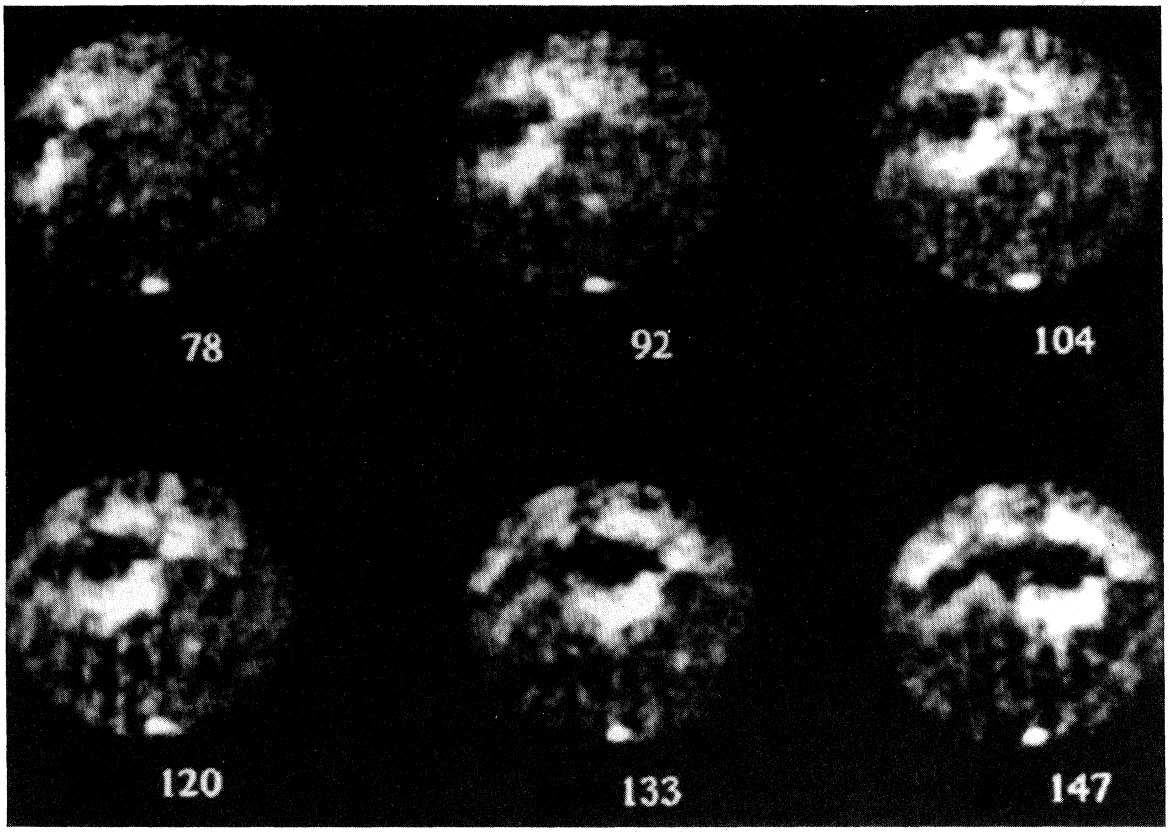

FIG. 23. Goldstone-VLA images of Mars at six west longitudes (deg), made at 3.5 cm in the SC polarization. Note the very bright residual south polar ice cap. In the north hemisphere, the brightest features are in Tharsis, which is traversed by the low-albedo Stealth region (Muhleman *et al.*, 1991).

1988; van Albada *et al.*, 1990). The backscattered intensity is enhanced, and the forward diffusion through the medium reduced, by constructive interference between fields propagating along identical but time-reversed paths (John, 1990, 1991). Coherent backscattering, also known as weak localization, is the causative precursor of strong localization, in which the mutual interference of scattered waves establishes a diffusion threshold in disordered media (Anderson, 1958): the extended normal modes become localized, concentrating the electromagnetic energy in standing waves rather than in traveling waves (Levi, 1991).

MacKintosh and John (1988) noted that the degree of coherent-backscattering enhancement for vector waves depends on the polarizations of the illumination and the detector. Scattering produces a sequence of rotations of the polarization vector, but the rotation matrices do not commute; so only diagonal elements for opposite sequences of scattering events remain coherent. For circularly polarized waves, the amplitudes relating incident and scattered states contain phase factors that express the non-Abelian nature of the rotation group in three dimensions. The coherence of reversed paths is largely preserved for scattering into the SC state (or, when linears are transmitted, the SL state), but largely destroyed for scattering into the OC (or OL) state (MacKintosh and John, 1988, 1989). MacKintosh *et al.* (1989) and Hapke and Blewett (1991) described laboratory experiments that demonstrate the "circular polarization memory" of coherently backscattered light.

Mishchenko (1992a) generalized results of the theory of multiple scattering of scalar waves in discrete random media consisting of independent, randomly oriented spheroids. Using several common representations of polarization, he showed backscattering enhancement factors to depend on incident polarization, absorption, particle size and shape, incidence angle, and the optical depth of the scattering volume. Peters (1992; see also Ozrin, 1992) developed a theory for coherent backscatter of vector waves that accounts for effects of polarization and absorption, and that can explain the Galilean satellite echoes if the scatterers in the regoliths are anisotropic, i.e., forward scattering. His results are consistent with those of Mishchenko's (1992b) studies of scattering from a semi-infinite slab of polydisperse spheroids with refractive index ~ 1.5 and effective radii $\sim \lambda$. In Peters's for-

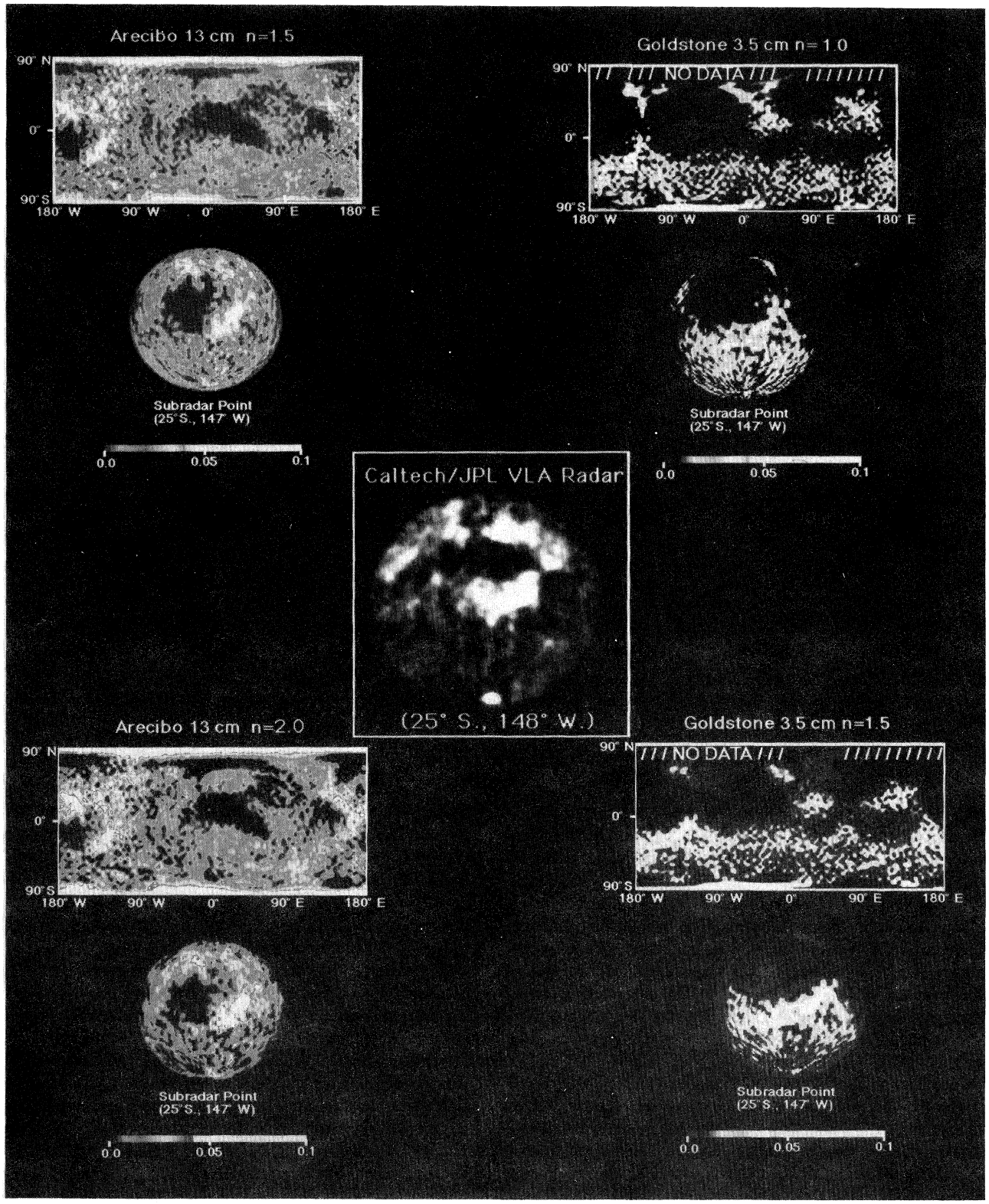

FIG. 24. Mars SC maps made from inversion of echo spectra obtained at Arecibo (left) and Goldstone (right). In the inversion, the albedos of individual surface facets were adjusted using least squares. For each observatory, results are shown for two assumed values of the exponent in a $\cos^n\theta$ scattering law. In the center is one of the Goldstone-VLA images from Fig. 23. After Harmon, Slade, and Hudson, 1992.

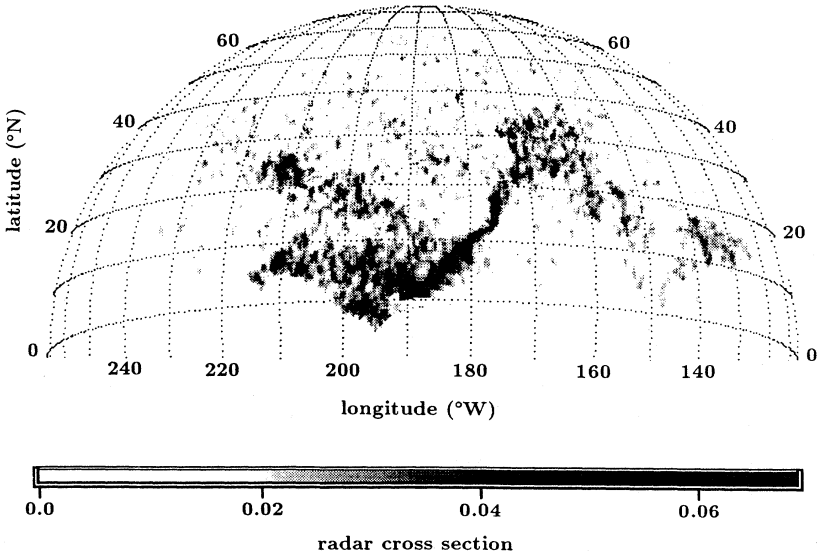

FIG. 25. Arecibo 13-cm SC reflectivity map of the Elysium region of Mars, obtained from random-code observations made at subradar latitude 10° S. The map is *N/S* ambiguous, but more northerly observations confirm that all of the strong features come from the north. The radar-bright regions (shown here as dark) correspond to the volcano Elysium Mons (25° N, 214° W) and the associated flood basin and outflow channel. The SC brightness of these regions probably is caused by extremely rough lava flows (Harmon, Sulzer, *et al.*, 1992).

mulation, the scattering is due to random fluctuations in dielectric constant, so the scatterers can be either particles, e.g., pieces of cratering ejecta dispersed in the regolith, or uncoordinated modulations in bulk density that occur randomly throughout a smoothly heterogeneous regolith (Ostro and Shoemaker, 1990). The possible existence of structure in icy regoliths that does not develop in silicate regoliths is an open question. The simplest hypothesis may be that the icy regoliths are structurally nearly identical to the lunar regolith and that the exotic echoes from the icy satellites arise because of the much longer photon path lengths in ice.

Absorption reduces both μ_C and the albedo, the latter dramatically. For example, for a half space of anisotropic scatterers, increasing the ratio of the inelastic mean free path for absorption to the elastic mean free path for scattering from 2 to ∞ would increase the backscattered intensity by a factor of 2.6 and μ_C by a factor of only 1.2 (Peters, 1992). The prediction of a much greater range in albedo than in polarization ratio is consistent with the radar observations of Europa, Ganymede, and Callisto (Ostro *et al.*, 1992), which show that intersatellite and intrasatellite variations in $\hat{\sigma}_{OC}$ are much greater than the corresponding variations in μ_C. Silicates increase the absorption of ice dramatically. Therefore radar albedo can be taken as a crude indicator of ice purity, which might be lowest for the most ancient terrains and highest for terrains that have experienced recent resurfacing (e.g., McKinnon and Parmentier, 1986).

There are similarities between the icy Galilean satellites' radar properties and those of the radar-bright polar caps on Mars and Mercury. Coherent backscattering may also help to account for echoes with $\mu_C \sim 1$ that have been detected from targets as diverse as Saturn's rings (Goldstein *et al.*, 1977), the Earth-crossing asteroid 2101 Adonis (Ostro, Campbell, Chandler, Shapiro, *et al.*, 1991), and highly reflective regions on Venus (Tryka and Muhleman, 1992). Moreover, the surge in optical brightness seen for solid-surfaced objects as the Sun-object-Earth angle ϕ approaches zero (the opposition effect), as well as ϕ-dependent optical polarization signatures of those bodies, may be caused in part, if not entirely, by coherent backscatter (Muinonen, 1990; Hapke *et al.*, 1993; Kolokolova *et al.*, 1993; Mishchenko, 1993).

G. Io and Titan

Io, Jupiter's innermost Galilean satellite, is the geologically most active planetary body in the solar system. Virtually every characteristic of this object's surface is a product of ongoing volcanism energized by its tidal interaction with Jupiter (Nash *et al.*, 1986). Whereas Voyager imaged parts of the satellite at resolutions of several kilometers and various VIS/IR measurements have probed the surface's microscale properties, the radar data offer insight into the nature of the surface at centimeter-to-kilometer scales.

Echoes from Io were first detected during 1976–1980, but were too weak to establish the satellite's radar properties. Arecibo observations during 1987–1990 yielded convincing echoes from Io on each of 11 dates (Ostro, Rosema, Campbell, *et al.*, 1990). The Arecibo observations provide fairly thorough longitude coverage and reveal significant heterogeneity in Io's radar properties. Io's average μ_C is about 0.5, an order of magnitude larger than the corresponding value for the Moon. Io's total-power radar albedo averages about 3 times the lunar value.

Apart from exploration by landing spacecraft, radar provides the only direct means to study the cloud-shrouded surface of Titan, Saturn's largest satellite. Voyager and ground-based data indicate a surface temperature and pressure of 94 K and 1.5 bar and show that the atmosphere is mostly N_2 with traces of hydrocarbons and nitriles (Hunten *et al.*, 1984, and references therein). Thermodynamic considerations imply a near-surface reservoir of liquid hydrocarbons, possibly consisting of a kilometer-deep global ocean. That configuration, which would give a radar albedo of only several percent, has

been ruled out by Goldstone-VLA detections that yield estimates of $\hat{\sigma}_{OC}$ from 0.05 to 0.75; there are hints that μ_C might be comparable to or greater than unity for certain longitudes (Muhleman *et al.*, 1990, 1992). More work is needed to elucidate Titan's radar properties and to understand them in conjunction with Titan's radio light-curve, which is virtually independent of longitude and yields a 3.5-cm emissivity of 0.88 ± 0.03 (Grossman and Muhleman, 1992).

V. FUTURE WORK

Radar astronomy stands on the threshold of producing an enormously valuable body of new information about asteroids, comets, planets, and their satellites. By the mid 1990s, improvements in telescope sensitivity and data-acquisition hardware will extend the technique to smaller and more distant targets. With the upgraded Arecibo telescope, radar investigations of natural satellites will reap enormous benefits, especially for Io and Titan. Doppler images of Titan may provide a coarse-resolution, nearly global albedo map while the high-resolution radar mapper on the Cassini spacecraft (Elachi *et al.*, 1991) is on its way to Saturn. Iapetus should be detectable, and radar measurements could elucidate near-surface morphology on the disparate hemispheres of this unusual object. Rhea and Amalthea probably will be detectable, and small Saturn satellites like Dione and Hyperion will lie near the limits of radar detectability, where Io and Titan are now.

The Goldstone radar is undergoing several modifications to improve its effectiveness with targets having short round-trip times. In addition, a new high-efficiency 34-m antenna 22 km from the 70-m main antenna will permit radar interferometry of small bodies. Bistatic observations linking either Arecibo or Goldstone to the 100-m Greenbank Telescope now under construction would be advantageous for studies of many targets. Meanwhile, Goldstone-VLA observations should complete the full-disc SC mapping of the terrestrial planets, and Arecibo random-code observations should make SC images of much of Mercury and Mars at resolutions finer than 10 km.

The impact of the Arecibo upgrade on studies of small bodies is likely to be far-reaching. Currently, Arecibo can barely skim the inner edge of the mainbelt, but the upgraded telescope will have access to asteroids throughout the belt (Fig. 29). During its first decade of operation, the instrument should provide several-hundred-pixel images of ~ 100 mainbelt asteroids and

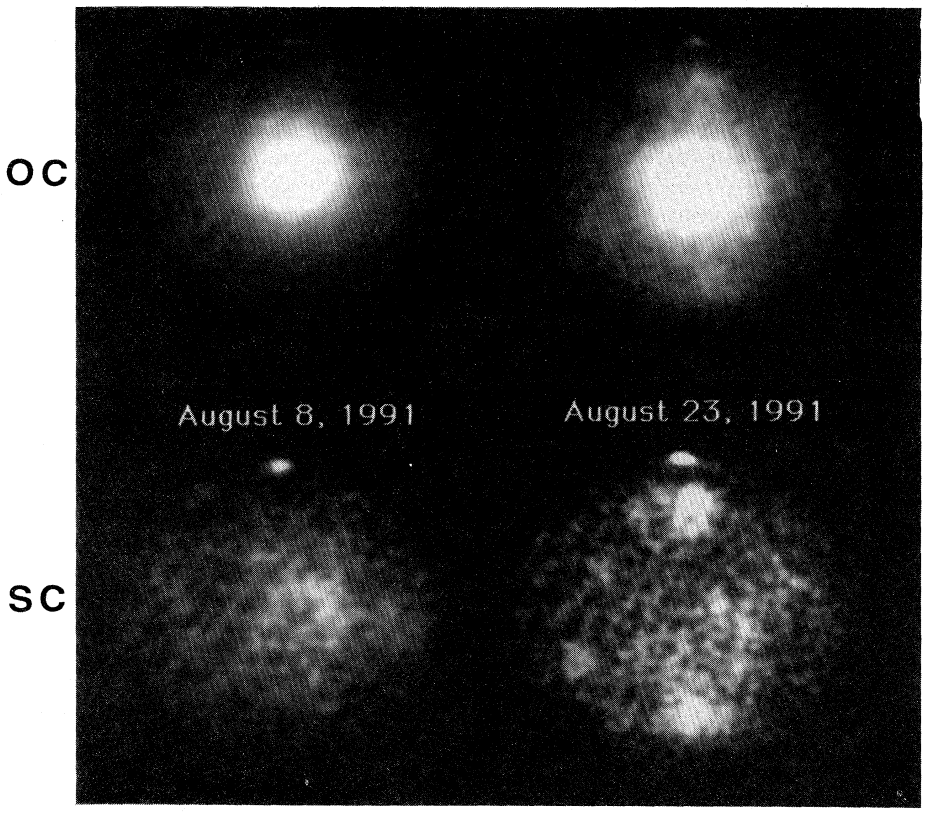

FIG. 26. Goldstone-VLA images of Mercury taken at 3.5 cm in the SC and OC polarizations at 11° N and longitudes 253° W (left) and 354° W. The SC and OC images have different brightness scales (Slade *et al.*, 1992).

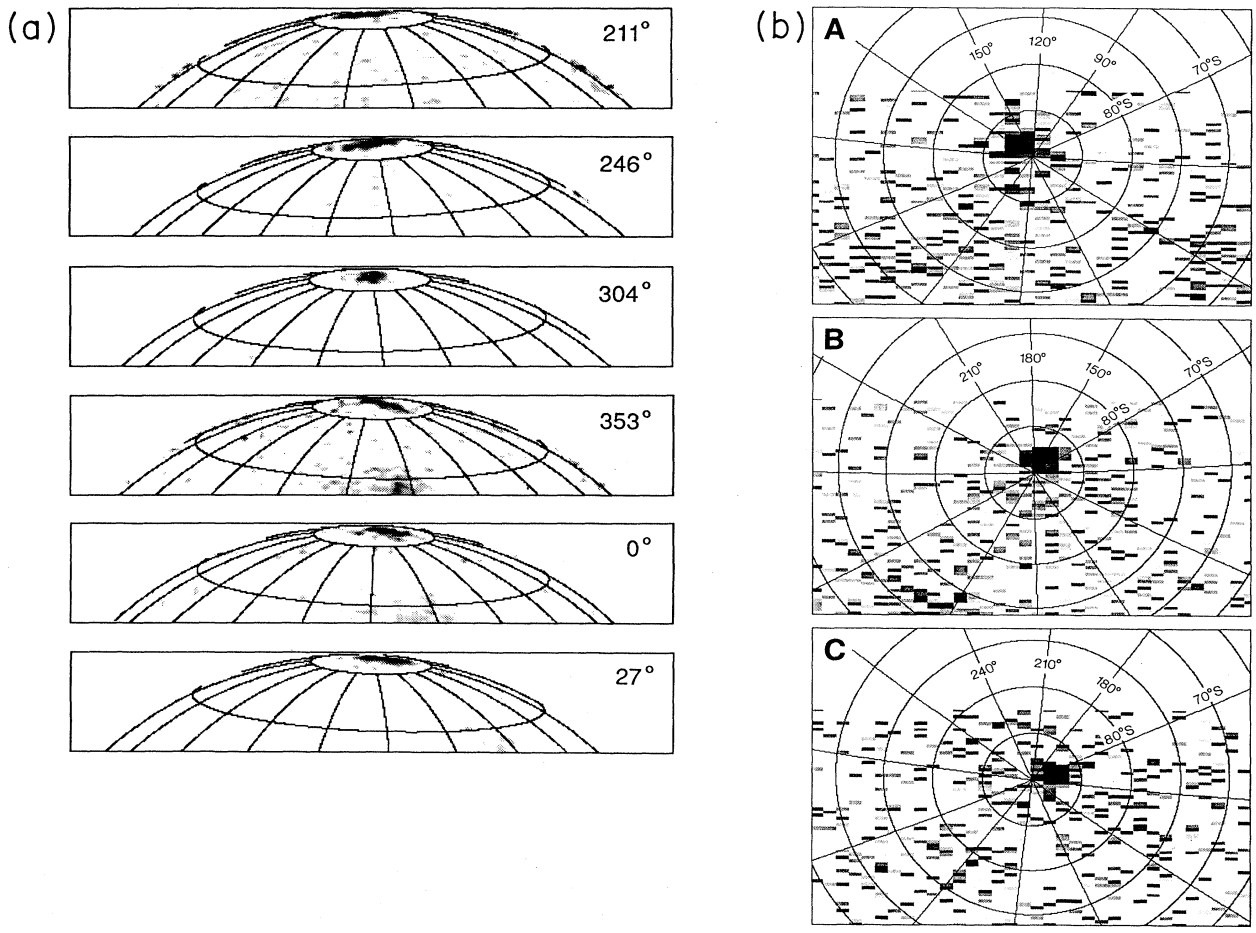

FIG. 27. Arecibo 13-cm SC maps of Mercury's polar regions, made using a random-code wave form: (a) plane-of-sky projections showing the north pole, from images obtained at subradar latitude 10° N and six longitudes; (b) pole-on projections of the south polar region from images obtained at three subradar longitudes, at latitudes between 7° S and 8° S. In (b) the radar's direction was toward the bottom of the page (Harmon and Slade, 1992).

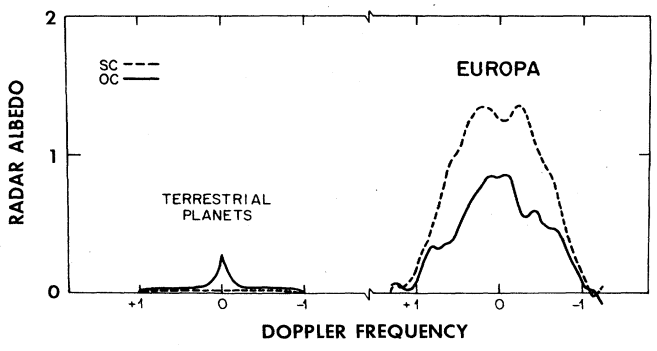

FIG. 28. Typical 13-cm echo spectra for the terrestrial planets compared to echo spectra for Jupiter's icy moon Europa. The abscissa has units of half the echo bandwidth.

several-thousand-pixel images of a comparable number of near-Earth asteroids. Programs to discover and characterize small bodies are growing exponentially and might be accelerated further during the coming decade as a part of efforts to elucidate the nature of potential hazards posed by large Earth-crossing asteroids and comets over very long time scales (Morrison, 1992). Most of the optically discoverable Earth crossers will traverse the Arecibo/Goldstone detectability window at least once every few decades. Dedicated optical telescopes probably could find ~100 000 objects at least as large as several tens of meters. In view of the utility of radar observations for orbit refinement and physical characterization, there is compelling motivation to obtain echoes from new objects as soon as possible after discovery. Eventually, the initial radar reconnaissance of a new Earth-crossing asteroid may become an almost daily event.

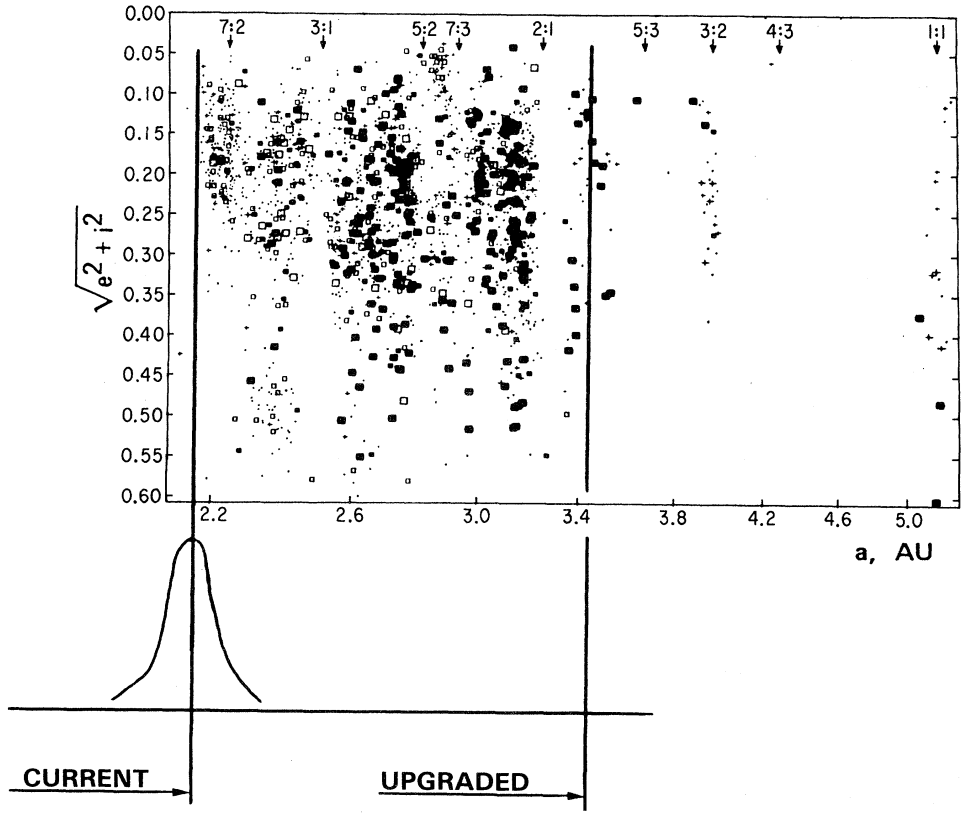

FIG. 29. Effects of the Arecibo upgrade on the radar detectability of mainbelt asteroids. This schematic of the belt from Chapman (1979) shows ~2000 objects coded for size and VIS/IR class: C asteroids are shown as solid boxes, S as open boxes, other classes as crosses, and unclassified objects as dots. The larger boxes and crosses indicate diameters > 80 km. Vertical lines are means of distributions (approximate form sketched at left) of the single-date detectability range of the 1992 Arecibo telescope and after completion of the upgrade now in progress (Ostro, 1987).

ACKNOWLEDGMENTS

Part of this research was conducted at the Jet Propulsion Laboratory, California Institute of Technology, under contract with the National Aeronautics and Space Administration (NASA).

REFERENCES

A'Hearn, M. F., 1988, "Observations of cometary nuclei," Annu. Rev. Earth Planet Sci. **16**, 273.

Anders, E., 1988, "Circumstellar material in meterorites: noble gases, carbon, and nitrogen," in *Meteorites and the Early Solar System,* edited by J. F. Kerridge and M. S. Matthews (University of Arizona, Tucson), p. 927.

Anderson, J. D., J. K. Campbell, R. F. Jurgens, E. L. Lau, X X Newhall, M. A. Slade III, and E. M. Standish, Jr., 1992, "Recent Developments in solar system tests of general relativity," in *Proceedings of the Sixth Marcel Grossmann Meeting on General Relativity,* edited by H. Sato and T. Nakamura (World Scientific, London), p. 353.

Anderson, J. D., M. S. W. Keesey, E. L. Lau, E. M. Standish, Jr., and X X Newhall, 1978, "Tests of general relativity using astrometric and radiometric observations of the planets," Acta Astron. **5**, 43.

Anderson, J. D., M. A. Slade, R. F. Jurgens, E. L. Lau, X X Newhall, and E. M. Standish, Jr., 1991, "Radar and spacecraft ranging to Mercury," Proc. Astron. Soc. Aust. **9**, 324.

Anderson, P. W., 1958, "Absence of diffusion in certain random lattices," Phys. Rev. **109**, 1492.

Arecibo Observatory User's Manual, 1989 (National Astronomy and Ionosphere Center, Arecibo, Puerto Rico).

Arvidson, R. E., R. Greeley, M. C. Malin, R. S. Saunders, V. R. Baker, C. Elachi, N. Izenberg, J. J. Plaut, E. R. Stofan, and M. K. Shepard, 1992, "Surface modification of Venus as inferred from Magellan observations of plains," J. Geophys. Res. **97**, 13 303.

Ash, M. E., I. I. Shapiro, and W. B. Smith, 1967, "Astronomical constants and planetary ephemerides deduced from radar and optical observations," Astron. J. **72**, 338.

Ash, M. E., I. I. Shapiro, and W. B. Smith, 1971, "The system of planetary masses," Science **174**, 551.

Bahar, E., D. E. Barrick, and M. A. Fitzwater, 1983, "Computations of scattering cross sections for composite surfaces and the specification of the wavenumber where spectral splitting occurs," IEEE Trans. Antennas Propag. **AP-31**, 698.

Barsukov, V. L., *et al.*, 1986, "The geology and geomorphology of the Venus surface as revealed by the radar images obtained by Veneras 15 and 16," J. Geophys. Res. **91**, Suppl., D378.

Bay, Z., 1947, "Reflection of microwaves from the Moon," Hung. Acta Phys. **1**, 1.

Beckmann, P., 1963, "Part I—Theory," in *The Scattering of Electromagnetic Waves from Rough Surfaces,* edited by P. Beckmann and A. Spizzichino (Pergamon, New York), p. 3.

Beehler, R. E., R. C. Mockler, and J. M. Richardson, 1965, "Cesium beam atomic time and frequency standards," Metrologia **1**, 114.

Bell, J. F., D. R. Davis, W. K. Hartmann, and M. J. Gaffey, 1989, "Asteroids: the big picture," in *Asteroids II,* edited by R. P. Binzel, T. Gehrels, and M. S. Matthews (University of Arizona, Tucson), p. 921.

Belton, M. J. S., W. H. Julian, A. J. Anderson, and B. E. A. Mueller, 1991, "The spin state and homogeneity of Comet Halley's nucleus," Icarus **93**, 183.

Belton, M. J. S., *et al.*, 1992, "Galileo encounter with 951 Gaspra: first pictures of an asteroid," Science **257**, 1647.

Bergman, D. J., 1978, "The dielectric constant of a composite material—a problem in classical physics," Phys. Rep. C **43**, 377.

Binzel, R. P., and S. Xu, 1993, "Chips off Asteroid 4 Vesta: Evidence for the parent body of basaltic achondrite meteorites," Science **260**, 186.

Breit, G., and M. A. Tuve, 1926, "A test of the existence of the conducting layer," Phys. Rev. **28**, 554.

Britt, D. T., D. J. Tholen, J. F. Bell, and C. M. Pieters, 1992, "Comparison of asteroid and meteorite spectra: classification by principal component analysis," Icarus **99**, 153.

Brouwer, D., and G. M. Clemence, 1961, "Orbits and masses of planets and satellites," in *Planets and Satellites,* edited by G. P. Kuiper and B. M. Middlehurst (University of Chicago, Chicago), p. 31.

Burns, J. A., 1976, "Consequences of the tidal slowing of Mercury," Icarus **28**, 453.

Burns, B. A., and D. B. Campbell, 1985, "Radar evidence for cratering on Venus," J. Geophys. Res. **90**, 3037.

Butler, B., D. O. Muhleman, and M. A. Slade, 1993, "Mercury: full disk radar images and the detection and stability of ice at the north pole," J. Geophys. Res. **98**, 15 003.

Campbell, D. B., and B. A. Burns, 1980, "Earth-based radar imagery of Venus," J. Geophys. Res. **85**, 8271.

Campbell, D. B., R. B. Dyce, R. P. Ingalls, G. H. Pettengill, and I. I. Shapiro, 1972, "Venus: topography revealed by radar data," Science **175**, 514.

Campbell, D. B., J. K. Harmon, and I. I. Shapiro, 1989, "Radar observations of Comet Halley," Astrophys. J. **338**, 1094.

Campbell, D. B., J. W. Head, J. K. Harmon, and A. A. Hine, 1983, "Venus: identification of banded terrain in the mountains of Ishtar Terra," Science **221**, 644.

Campbell, D. B., J. W. Head, J. K. Harmon, and A. A. Hine, 1984, "Venus: volcanism and rift formation in Beta Regio," Science **226**, 167.

Campbell, D. B., J. W. Head, A. A. Hine, J. K. Harmon, D. A. Senske, and P. C. Fisher, 1989, "Styles of volcanism on Venus: New Arecibo high resolution radar data," Science **246**, 373.

Campbell, D. B., D. A. Senske, J. W. Head, A. A. Hine, and P. C. Fisher, 1991, "Venus southern hemisphere: geologic character and age of terrains in the Themis-Alpha-Lada region," Science **251**, 180.

Campbell, D. B., N. J. S. Stacy, W. I. Newman, R. E. Arvidson, E. M. Jones, G. S. Musser, A. Y. Roper, and C. Schaller, 1992, "Magellan observations of extended impact crater related features on the surface of Venus," J. Geophys. Res. **97**, 16 249.

Campbell, M. J., and J. Ulrichs, 1969, "Electrical properties of rocks and their significance for lunar radar observations," J. Geophys. Res. **74**, 5867.

Carpenter, R. L., 1964, "Study of Venus by cw radar," Astron. J. **69**, 2.

Cassen, P., and A. P. Boss, 1988, "Protostellar collapse, dust grains, and solar-system formation," in *Meteorites and the Early Solar System,* edited by J. F. Kerridge and M. S. Matthews (University of Arizona, Tucson), p. 304.

Chandrasekhar, S., 1960, *Radiative Transfer* (Dover, New York).

Chapman, C. R., 1979, "The asteroids: nature, interrelations, origins, and evolution," in *Asteroids,* edited by T. Gehrels (University of Arizona, Tucson), p. 25.

Chavineau, B., P. Farinella, and F. Mignard, 1991, "The lifetime of binary asteroids vs gravitational encounters and collisions," Icarus **94**, 299.

Colombo, G., 1965, "On the rotational period of the planet Mercury," Nature **208**, 575.

Colombo, G., and I. I. Shapiro, 1966, "The rotation of the planet Mercury," Astrophys. J. **145**, 296.

Connerney, J. E. P., and N. F. Ness, 1988, "Mercury's magnetic field and interior," in *Mercury,* edited by F. Vilas, C. R. Chapman, and M. S. Matthews (University of Arizona, Tucson), p. 494.

Cormier, R. A., and A. Mizuhara, 1992, "250-kW cw klystron amplifier for planetary radar," IEEE Trans. Microwave Theory Tech. **40**, 1056.

Counselman, C. C., 1969, "Spin-orbit resonance of Mercury," Ph.D. thesis (Massachusetts Institute of Technology).

Cruikshank D. P., D. J. Tholen, W. K. Hartmann, J. F. Bell, and R. H. Brown, 1991, "Three basaltic Earth-approaching asteroids and the source of the basaltic meteorites," Icarus **89**, 1.

Davies, M. E., T. R. Colvin, P. G. Rogers, P. W. Chodas, W. L. Sjogren, E. L. Akim, V. A. Stepanyantz, Z. P. Vlasova, and A. I. Zakharov, 1992, "The rotation period, direction of the north pole, and geodetic control network of Venus," J. Geophys. Res. **97**, 12 141.

Deley, G. W., 1970, "Waveform Design," in *Radar Handbook,* edited by M. I. Skolnik (McGraw-Hill, New York), p. 3-1.

de Pater, I., P. Palmer, L. E. Snyder, S. J. Ostro, D. K. Yeomans, and D. L. Mitchell, 1992, "Bistatic radar observations of asteroids 324 Bamberga, 7 Iris, and 1991 EE," Bull. Am. Astron. Soc. **24**, 934.

Dewitt, J. M., Jr., and E. K. Stodola, 1949, "Detection of radio signals reflected from the Moon," Proc. IRE **37**, 229.

Downs, G. S., P. E. Reichley, and R. R. Green, 1975, "Radar measurements of Martian topography and surface properties: the 1971 and 1973 oppositions," Icarus **26**, 273.

Dvorsky, J. D., N. A. Renzetti, and D. E. Fulton, 1992, "The Goldstone solar system radar: a science instrument for planetary research" (Jet Propulsion Laboratory, Pasadena, CA), Publication 92–29.

Dyce, R. B., G. H. Pettengill, and I. I. Shapiro, 1967, "Radar determination of the rotations of Venus and Mercury, Astron. J. **72**, 351.

Edde B., 1993, *Radar: Principles, Technology, Applications* (Prentice-Hall, Englewood Cliffs, NJ).

Elachi, C., 1987, *Spaceborne Radar Remote Sensing: Applications and Techniques* (IEEE, New York).

Elachi, C., E. Im, L. E. Roth, and C. L. Werner, 1991, "Cassini Titan radar mapper," Proc. IEEE **79**, 867.

Eshleman, V. R., 1986a, "Mode decoupling during retrorefraction as an explanation for bizarre radar echoes from icy moons," Nature **319**, 755.
Eshleman, V. R., 1986b, "Radar glory from buried craters on icy moons," Science **234**, 587.
Etemad, S., R. Thompson, and M. J. Andrejco, 1986, "Weak localization of photons: universal fluctuations and ensemble averaging," Phys. Rev. Lett. **57**, 575.
Evans, J. V., 1960, "Radar astronomy," Contemp. Phys. **2**, 116.
Evans, J. V., 1962, "Radar echo studies of the Moon," in *Physics and Astronomy of the Moon,* edited by Z. Kopal (Academic, London), p. 429.
Evans, J. V., and G. H. Pettengill, 1963, "The scattering behavior of the Moon at wavelengths of 3.6, 68, and 784 centimeters," J. Geophys. Res. **68**, 423.
Farinella, P., 1992, "Evolution of Earth-crossing binary asteroids due to gravitational encounters with the Earth," Icarus **96**, 284.
Ford, P. G., F. Liu, and G. H. Pettengill, 1992, "Pancakelike domes on Venus," J. Geophys. Res. **97**, 15 967.
Ford, P. G., and G. H. Pettengill, 1992, "Venus topography and kilometer-scale slopes," J. Geophys. Res. **97**, 13 103.
Gaffey, M. J., J. F. Bell, and D. P. Cruikshank, 1989, "Reflectance spectroscopy and asteroid surface mineralogy," in *Asteroids II,* edited by R. P. Binzel, T. Gehrels, and M. S. Matthews (University of Arizona, Tucson), p. 98.
Garvin, J. B., J. W. Head, G. H. Pettengill, and S. H. Zisk, 1985, "Venus global radar reflectivity and correlations with elevation," J. Geophys. Res. **90**, 6859.
Gault, D. E., J. A. Burns, and P. Cassen, 1977, "Mercury," Annu. Rev. Astron. Astrophys. **15**, 97.
Gilvarry, J. J., 1953, "Relativity precession of the asteroid Icarus," Phys. Rev. **89**, 1046.
Goldreich, P., and S. J. Peale, 1966, "Spin-orbit coupling in the solar system," Astron. J. **71**, 425.
Goldstein, R. M., 1964, "Venus characteristics by Earth-based radar," Astron. J. **69**, 12.
Goldstein, R. M., 1965, "Preliminary Venus radar results," Radio Sci. D **69**, 1623.
Goldstein, R. M., 1968, "Radar observations of Icarus," Science **162**, 903.
Goldstein, R. M., 1971, "Radar observations of Mercury," Astron. J. **76**, 1152.
Goldstein, R. M., and R. R. Green, 1980, "Ganymede: radar surface characteristics," Science **207**, 179.
Goldstein, R. M., R. R. Green, G. H. Pettengill, and D. B. Campbell, 1977, "The rings of Saturn: two-frequency radar observations," Icarus **30**, 104.
Goldstein, R. M., R. R. Green, and H. C. Rumsey, 1978, "Venus radar brightness and altitude images," Icarus **36**, 334.
Goldstein, R. M., R. F. Jurgens, and Z. Sekanina, 1984, "A radar study of Comet IRAS-Araki-Alcock 1983d," Astron. J. **89**, 1745.
Goldstein, R. M., and H. C. Rumsey, 1972, "A radar image of Venus," Icarus **17**, 699.
Greeley, R., *et al.*, 1992, "Aeolian features on Venus: preliminary Magellan results," J. Geophys. Res. **97**, 13 319.
Green, P. E., Jr., 1962, "Radar astronomy measurement techniques" (MIT Lincoln Laboratory, Lexington, MA), Technical Report No. 282.
Grieg, D. D., S. Metzger, and R. Waer, 1948, "Considerations of Moon-relay communication," Proc. IRE **36**, 652.
Grossman, A. W., and D. O. Muhleman, 1992, "Observations of Titan's radio light-curve," Bull. Am. Astron. Soc. **24**, 954.
Hagfors, T., 1964, "Backscatter from an undulating surface with applications to radar returns from the Moon," J. Geophys. Res. **69**, 3779.
Hagfors, T., 1967, *Radar Studies of the Moon, Final Report, Vol. 1* (MIT Lincoln Laboratory, Lexington, MA).
Hagfors, T., and D. B. Campbell, 1973, "Mapping of planetary surfaces by radar," Proc. IEEE **61**, 1219.
Hagfors, T., T. Gold, and M. Ierkic, 1985, "Refraction scattering as origin of the anomalous radar returns of Jupiter's satellites," Nature **315**, 637.
Hagfors, T., and W. Kofman, 1991, "Mapping of overspread targets in radar astronomy," Radio Sci. **26**, 403.
Hagfors, T., B. Nanni, and K. Stone, 1968, "Aperture synthesis in radar astronomy and some applications to lunar and planetary studies," Radio Sci. **3**, 491.
Hansen, J. E., and L. D. Travis, 1974, "Light scattering in planetary atmospheres," Space Sci. Rev. **16**, 527.
Hapke, B., 1993, *Theory of Reflectance and Emittance Spectroscopy* (Cambridge University Press, New York).
Hapke, B., 1990, "Coherent backscatter and the radar characteristics of outer planet satellites," Icarus **88**, 407.
Hapke, B., and D. Blewett, 1991, "Coherent backscattering model for the unusual radar reflectivity of icy satellites," Nature **352**, 46.
Hapke, B. W., R. M. Nelson, and W. D. Smythe, 1993, "The opposition effect of the Moon: the contribution of coherent backscatter," Science **260**, 509.
Harkness, W., 1981, *The Solar Parallax and Its Related Constants, Including the Figure and Density of the Earth* (U.S. GPO, Washington, DC).
Harmon, J. K., D. B. Campbell, D. L. Bindschadler, J. W. Head, and I. I. Shapiro, 1986, "Radar altimetry of Mercury: a preliminary analysis," J. Geophys. Res. **91**, 385.
Harmon, J. K., D. B. Campbell, A. A. Hine, I. I. Shapiro, and B. G. Marsden, 1989, "Radar observations of Comet IRAS-Araki-Alcock 1983d," Astrophys. J. **338**, 1071.
Harmon, J. K., D. B. Campbell, and S. J. Ostro, 1982, "Dual-polarization radar observations of Mars: Tharsis and environs," Icarus **52**, 171.
Harmon, J. K., and S. J. Ostro, 1985, "Mars: dual-polarization radar observations with extended coverage," Icarus **62**, 110.
Harmon, J. K., and M. A. Slade, 1992, "Radar mapping of Mercury: full-disk images and polar anomalies," Science **258**, 640.
Harmon, J. K., M. A. Slade, and R. S. Hudson, 1992, "Mars radar scattering: Arecibo/Goldstone results at 12.6-cm and 3.5-cm wavelengths," Icarus **98**, 240.
Harmon, J. K., M. P. Sulzer, P. J. Perillat, and J. F. Chandler, 1992, "Mars radar mapping: strong backscatter from the Elysium basin and outflow channel," Icarus **95**, 153.
Hartmann, W. K., 1979, "Diverse puzzling asteroids and a possible unified explanation," in *Asteroids,* edited by T. Gehrels (University of Arizona, Tucson), p. 466.
Head, J. W., D. B. Campbell, C. Elachi, J. E. Guest, D. P. McKenzie, R. S. Saunders, G. G. Schaber, and G. Schubert, 1991, "Venus volcanism: initial analysis from Magellan data," Science **252**, 276.
Head, J. W., L. S. Crumpler, J. C. Aubele, J. E. Guest, and R. S. Saunders, 1992, "Venus volcanism: classification of volcanic features and structures, associations, and global distribution from Magellan data," J. Geophys. Res. **97**, 13 153.
Helin, E. F., 1989, IAU Circ. No. 4831.
Hellings, R. W., 1984, "Testing relativity with solar system dynamics," in *General Relativity and Gravitation,* edited by B. Bertotti, F. de Felice, and A. Pascolini (Reidel, Dordrecht), p.

365.
Hellings, R. W., P. J. Adams, J. D. Anderson, M. S. Keesey, E. L. Lau, E. M. Standish, V. M. Canuto, and I. Goldman, 1983, "An experimental test of the variability of G using Viking Lander ranging data," Phys. Rev. Lett. **51**, 1609.
Hewitt, R. H., and H. E. Newsom, 1988, "Igneous activity in the early solar system," in *Meteorites and the Early Solar System,* edited by J. F. Kerridge and M. S. Matthews (University of Arizona, Tucson), p. 73.
Hill, G. W., 1873, "On the derivation of the mass of Jupiter from the motion of certain asteroids," Mem. Am. Acad. Arts Sci. **IX**, 417. [Memoir No. 11 in Collected Mathematical Works of G. W. Hill, pp. 105–108.]
Hill, R. D., 1991, "Origins of radar," Eos. Trans. Am. Geophys. Union **72**, 781.
Hudson, R. S., 1991, "Radar imaging for aircraft identification and planetary astronomy," Ph.D. thesis (California Institute of Technology).
Hudson, R. S., 1993, "Three-dimensional reconstruction of asteroids from radar observations," Remote Sensing Rev. **8**, 195.
Hudson, R. S., and S. J. Ostro, 1990, "Doppler radar imaging of spherical planetary surfaces," J. Geophys. Res. **95**, 10 947.
Hunten, D. M., M. G. Tomasko, F. M. Flasar, R. E. Samuelson, D. F. Strobel, and D. J. Stevenson, 1984, "Titan," in *Saturn,* edited by T. Gehrels and M. S. Matthews (University of Arizona, Tucson), p. 671.
Hut, P., E. M. Shoemaker, W. Alvarez, and A. Montanari, 1991, "Astronomical mechanisms and geologic evidence for multiple impacts on the Earth," Lunar Planet. Sci. Conf. XXII, 603.
Jenkins, G. M., and D. G. Watts, 1968, *Spectral Analysis and Its Applications* (Holden-Day, San Francisco), p. 217.
Jet Propulsion Laboratory, 1983, "Technical Manual TN 03704 MP-1, TWM&CCR Assembly" (JPL, Pasadena, CA).
John, S., 1990, "The localization of waves in disordered media," in *Scattering and Localization of Classical Waves in Random Media,* edited by P. Sheng (World Scientific, Singapore), p. 1.
John, S., 1991, "Localization of light," Phys. Today **44**, No. 5, 32.
Jurgens, R. F., 1970, "Some preliminary results of the 70-cm radar studies of Venus," Radio Sci. **5**, 435.
Jurgens, R. F., R. M. Goldstein, H. R. Rumsey, and R. R. Green, 1980, "Images of Venus by three-station radar interferometry—1977 results," J. Geophys. Res. **85**, 8282.
Jurgens, R. F., M. A. Slade, and R. S. Saunders, 1988, "Evidence for highly reflecting materials on the surface and subsurface of Venus," Science **240**, 1021.
Kamoun, P. G., D. B. Campbell, S. J. Ostro, G. H. Pettengill, and I. I. Shapiro, 1982, "Comet Encke: radar detection of nucleus," Science **216**, 293.
Karttunen, H., P. Kröger, H. Oja, M. Poutanen, and K. J. Donner, 1987, Eds., *Fundamental Astronomy* (Springer, Berlin), p. 39.
Kelly, J. M., J. O. Stenoien, and D. E. Isbell, 1953, "Waveguide measurements in the microwave region on metal powders suspended in paraffin wax," J. Appl. Phys. **24**, 258.
Kendall, M., and A. Stuart, 1977, *The Advanced Theory of Statistics, Vol. 1,* 4th ed. (MacMillan, New York), p. 398.
Kim, Y., and E. Rodriguez, 1992, "Comparison of the unified perturbation method with the two-scale expansion," IEEE Trans. Geosci. Remote Sensing **30**, 510.
Klaasen, K. P., 1976, "Mercury's rotation axis and period," Icarus **28**, 469.
Kolokolova, L. O., M. I. Mishchenko, and M. Wolff, 1993, "On the negative polarization of light scattered by subwavelength regolithic grains," Mon. Not. R. Astron. Soc. **260**, 550.
Kotel'nikov, V. A., 1965, "Radar observations of Venus in the Soviet Union in 1964," Radio Sci. D **69**, 1634.
Kotel'nikov, V. A., *et al.*, 1963, "Radar observations of Venus in the Soviet Union in 1962," Dokl. Akad. Nauk SSSR, **151**, 532 [Sov. Phys. Dokl. **8**, 642 (1964)].
Kotel'nikov, V. A., *et al.*, 1983, "39-cm radar observations of Mars in 1980," Astron. Zh. **60**, 422 [Sov. Astron. **27**, 246 (1983)].
Kraus, J. D., 1986, *Radio Astronomy* (Cygnus-Quasar, Powell, OH).
Lee, P. A., and T. V. Ramakrishnan, 1985, "Disordered electronic systems," Rev. Mod. Phys. **57**, 287.
Leick, A., 1990, *GPS Satellite Surveying* (Wiley, New York).
Levi, B. G., 1991, "Light travels more slowly through strongly scattering materials," Phys. Today **44**, No. 6, 17.
Lipa, B., and G. L. Tyler, 1976, "Surface slope probabilities from the spectra of weak radar echoes: application to Mars," Icarus **28**, 301.
Lipschutz, M. E., M. J. Gaffey, and P. Pellas, 1989, "Meteoritic parent bodies: nature, number, size and relation to present-day asteroids," in *Asteroids II,* edited by R. P. Binzel, T. Gehrels, and M. S. Matthews (University of Arizona, Tucson), p. 777.
Long, M. W., 1965, "On the polarization and the wavelength dependence of sea echo," Trans. IEEE **AP-14**, 749.
MacKintosh, F. C., and S. John, 1988, "Coherent backscattering of light in the presence of time-reversal-noninvariant and parity-nonconserving media," Phys. Rev. B **37**, 1884.
MacKintosh, F. C., and S. John, 1989, "Diffusing-wave spectroscopy and multiple scattering of light in correlated random media," Phys. Rev. B **40**, 2383.
MacKintosh, F. C., J. X. Zhu, D. J. Pine, and D. A. Weitz, 1989, "Polarization memory of multiply scattered light," Phys. Rev. B **40**, 9342.
Martelli, G., P. Rothwell, I. Giblin, P. N. Smith, M. DiMartino, and P. Farinella, 1993, "Fragment jets from catastrophic break-up events and the formation of asteroid binaries and families," Astron. Astrophys. **271**, 315.
McCollom, T. M., and B. M. Jakosky, 1993, "Interpretation of planetary radar observations: the relationship between actual and inferred slope distributions," J. Geophys. Res. **98**, 1173.
McFadden, L. A., D. J. Tholen, and G. J. Veeder, 1989, "Physical properties of Aten, Apollo, and Amor asteroids," in *Asteroids II,* edited by R. P. Binzel, T. Gehrels, and M. S. Matthews (University of Arizona, Tucson), p. 442.
McGuire, J. B., E. R. Spangler, and L. Wong, 1961, "The size of the solar system," Sci. Am. **204**, 64.
McKinnon, W. B., and E. M. Parmentier, 1986, "Ganymede and Callisto," in *Satellites,* edited by J. A. Burns and M. S. Matthews (University of Arizona, Tucson), p. 718.
Melosh, H. J., and J. A. Stansberry, 1991, "Doublet craters and the tidal disruption of binary asteroids," Icarus **94**, 171.
Milani, A., M. Carpino, G. Hahn, and A. M. Nobili, 1989, "Dynamics of planet-crossing asteroids: classes of orbital behaviour. Project Spaceguard," Icarus **78**, 212.
Mishchenko, M. I., 1992a, "Enhanced backscattering of polarized light from discrete random media: calculations in exactly the backscattering direction," J. Opt. Soc. Am. **9**, 978.
Mishchenko, M. I., 1992b, "Polarization characteristics of the coherent backscatter opposition effect," Earth, Moon, planets **58**, 127.
Mishchenko, M. I., 1993, "On the nature of the polarization op-

position effect exhibited by Saturn's rings," Astrophys. J. **411**, 351.
Mofenson, J., 1946, "Radar echoes from the Moon," Electronics **19**, 92.
Morrison, D., 1992, Ed., "The Spaceguard survey: Report of the NASA International Near-Earth-Object Detection Workshop" (Jet Propulsion Laboratory, Pasadena, CA).
Moyer, T. D., 1971, "Mathematical formulation of the Double-Precision Orbit Determination Program (DPODP)" (Jet Propulsion Laboratory, Pasadena, CA), JPL Technical Report No. 32-1527, p. 160.
Muhleman, D. O., 1966, "Planetary characteristics from radar observations," Space Sci. Rev. **6**, 341.
Muhleman, D. O., B. J. Butler, A. W. Grossman, and M. A. Slade, 1991, "Radar images of Mars," Science **253**, 1508.
Muhleman, D. O., A. W. Grossman, B. J. Butler, and M. A. Slade, 1990, "Radar reflectivity of Titan," Science **248**, 975.
Muhleman, D. O., A. W. Grossman, M. A. Slade, and B. J. Butler, 1992, "The surface of Titan and Titan's rotation: What is radar telling us?" Bull. Am. Astron. Soc. **24**, 954.
Muhleman, D. O., D. B. Holdridge, and N. Block, 1962, "The astronomical unit determined by radar reflections from Venus," Astron. J. **67**, 191.
Muinonen, K., 1990, "Light scattering by inhomogeneous media: backward enhancement and reversal of linear polarization," Ph.D. thesis (University of Helsinki, Finland).
Nash, D. B., M. H. Carr, J. Gradie, D. M. Hunten, and C. F. Yoder, 1986, "Io," in *Satellites,* edited by J. A. Burns and M. S. Matthews (University of Arizona, Tucson), p. 629.
Newhall, X X, E. M. Standish, and J. G. Williams, 1983, "DE 102: A numerically integrated ephemeris of the Moon and planets spanning forty-four centuries," Astron. Astrophys. **125**, 150.
Nielson, L. E., 1974, "The permittivity of suspensions and two-phase mixtures," J. Phys. D **7**, 1549.
Nobili, A. M., and C. M. Will, 1986, "The real value of Mercury's perihelion advance," Nature **320**, 39.
Ogilvy, J. A., 1991, *Theory of Wave Scattering from Random Rough Surfaces* (Adam Hilger, New York).
Ostro, S. J., 1987, "Benefits of an upgraded Arecibo Observatory for radar observations of asteroids and natural satellites," in *Proceedings of the Arecibo Upgrading Workshop,* edited by J. H. Taylor and M. M. Davis (National Astronomy and Ionosphere Center, Arecibo, Puerto Rico), p. 233.
Ostro, S. J., D. B. Campbell, J. F. Chandler, A. A. Hine, R. S. Hudson, K. D. Rosema, and I. I. Shapiro, 1991, "Asteroid 1986 DA: radar evidence for a metallic composition," Science **252**, 1399.
Ostro, S. J., D. B. Campbell, J. F. Chandler, I. I. Shapiro, A. A. Hine, R. Velez, R. F. Jurgens, K. D. Rosema, R. Winkler, and D. K. Yeomans, 1991, "Asteroid radar astrometry," Astron. J. **102**, 1490.
Ostro, S. J., D. B. Campbell, A. A. Hine, I. I. Shapiro, J. F. Chandler, C. L. Werner, and K. D. Rosema, 1990, "Radar images of Asteroid 1627 Ivar," Astron. J. **99**, 2012.
Ostro, S. J., D. B. Campbell, and I. I. Shapiro, 1985, "Mainbelt asteroids: Dual-polarization radar observations," Science **229**, 442.
Ostro, S. J., D. B. Campbell, and I. I. Shapiro, 1986, "Radar detection of 12 asteroids from Arecibo," Bull. Am. Astron. Soc. **18**, 796.
Ostro, S. J., *et al.*, 1992, "Europa, Ganymede, and Callisto: new radar results Arecibo and Goldstone," J. Geophys. Res. **97**, 18 227.
Ostro, S. J., J. F. Chandler, A. A. Hine, I. I. Shapiro, K. D. Rosema, and D. K. Yeomans, 1990, "Radar images of Asteroid 1989 PB," Science **248**, 1523.
Ostro, S. J., R. Connelly, and L. Belkora, 1988, "Asteroid shapes from radar echo spectra: a new theoretical approach," Icarus **73**, 15.
Ostro, S. J., J. K. Harmon, A. A. Hine, P. Perillat, D. B. Campbell, J. F. Chandler, I. I. Shapiro, R. F. Jurgens, and D. K. Yeomans, 1991, "High-resolution radar ranging to near-earth asteroids," Bull. Am. Astron. Soc. **23**, 1144.
Ostro, S. J., *et al.*, 1993, "Radar imaging of Asteroid 4179 Toutatis," Bull. Am. Astron. Soc. **25**, 1126.
Ostro, S. J., R. F. Jurgens, D. K. Yeomans, E. M. Standish, and W. Greiner, 1989, "Radar detection of Phobos," Science **243**, 1584.
Ostro, S. J., G. H. Pettengill, D. B. Campbell, and R. M. Goldstein, 1982, "Delay-Doppler radar observations of Saturn's rings," Icarus **49**, 367.
Ostro, S. J., K. D. Rosema, D. B. Campbell, J. F. Chandler, and I. I. Shapiro, 1990, "Io's radar properties," Bull. Am. Astron. Soc. **22**, 1109.
Ostro, S. J., K. D. Rosema, and R. F. Jurgens, 1990, "The shape of Eros," Icarus **84**, 334.
Ostro, S. J., and E. M. Shoemaker, 1990, "The extraordinary radar echoes from Europa, Ganymede, and Callisto: a geological perspective," Icarus **85**, 335.
Ozrin, V. D., 1992, "Exact solution for coherent backscattering of polarized light from a random medium of Rayleigh scatters," Waves Random Med. **2**, 141.
Paige, D. A., S. E. Wood, and A. R. Vasavada, 1992, "The thermal stability of water ice at the poles of Mercury," Science **258**, 643.
Parker, M. N., 1974, "Radio-wave scattering from rough surfaces and the estimation of surface shape," Ph.D. thesis (Stanford University).
Parker, M. N., and G. L. Tyler, 1973, "Bistatic radar estimation of surface-slope probability distributions with applications to the Moon," Radio Sci. **8**, 177.
Peale, S. J., 1969, "Generalized Cassini's Laws," Astron. J. **74**, 483.
Peale, S. J., 1976, "Does Mercury have a molten core?" Nature **262**, 765.
Peale, S. J., 1988, "The rotational dynamics of Mercury and the state of its core," in Mercury, edited by F. Vilas, C. R. Chapman, and M. S. Matthews (University of Arizona, Tucson), p. 461.
Peale, S. J., 1989, "On the density of Halley's Comet," Icarus **82**, 36.
Peale, S. J., 1992, "On LAMS and SAMs for Halley's rotation," in *Asteroids, Comets, Meteors 1991,* edited by A. W. Harris and E. Bowell (Lunar and Planetary Institute, Houston), p. 459.
Peters, K. J., 1992, "The coherent backscatter effect: a vector formulation accounting for polarization and absorption effects and small or large scatterers," Phys. Rev. B **46**, 801.
Pettengill, G. H., 1970, "Radar astronomy," in *Radar Handbook,* edited by M. I. Skolnik (McGraw-Hill, New York), p. 33-1.
Pettengill, G. H., H. W. Briscoe, J. V. Evans, E. Gehrels, G. M. Hyde, L. G. Kraft, R. Price, and W. B. Smith, 1962, "A radar investigation of Venus," Astron. J. **67**, 181.
Pettengill, G. H., and R. B. Dyce, 1965, "A radar determination of the rotation of the planet Mercury," Nature **206**, 1240.
Pettengill, G. H., R. B. Dyce, and D. B. Campbell, 1967, "Radar measurements at 70 cm of Venus and Mercury," Astron. J.

72, 330.
Pettengill, G. H., E. Eliason, P. G. Ford, G. B. Loriot, H. Masursky, and G. E. McGill, 1980, "Pioneer Venus radar results: altimetry and surface properties," J. Geophys. Res. **85**, 8261.
Pettengill, G. H., P. G. Ford, and B. D. Chapman, 1988, "Venus: surface electromagnetic properties," J. Geophys. Res. **93**, 14 881.
Pettengill, G. H., P. G. Ford, W. T. K. Johnson, R. K. Raney, and L. A. Soderblom, 1991, "Magellan: radar performance and data products," Science **252**, 260.
Pettengill, G. H., P. G. Ford, and R. J. Wilt, 1992, "Venus surface radiothermal emission as observed by Magellan," J. Geophys. Res. **97**, 13 091.
Pettengill, G. H., and I. I. Shapiro, 1965, "Radar astronomy," Annu. Rev. Astron. Astrophys. **3**, 377.
Pettengill, G. H., I. I. Shapiro, M. E. Ash, R. P. Ingalls, L. P. Rainville, W. B. Smith, and M. L. Stone, 1969, "Radar observations of Icarus," Icarus **10**, 432.
Phillips, R. J., R. E. Arvidson, J. M. Boyce, D. B. Campbell, J. E. Guest, G. G. Schaber, and L. A. Soderblom, 1991, "Impact craters on Venus: initial analysis from Magellan," Science **252**, 288.
Phillips, R. J., R. F. Raubertas, R. E. Arvidson, I. C. Sarkar, R. R. Herrick, N. Izenberg, and R. E. Grimm, 1992, "Impact craters and Venus resurfacing history," J. Geophys. Res. **97**, 15 923.
Pollack, J. B., and L. Whitehill, 1972, "A multiple-scattering model of the diffuse component of lunar radar echoes," J. Geophys. Res. **77**, 4289.
Priest, P., 1993, "Goldstone solar system radar capability and performance" (Jet Propulsion Laboratory, Pasadena, CA), Internal Report 1740-4.
Rabe, E., 1971, "The use of asteroids for determinations of masses and other fundamental constants," in *Physical Studies of Minor Planets, NASA SP-267,* edited by T. Gehrels (Scientific and Technical Information Office, NASA, Washington, DC), p. 13.
Ramsey, N. F., 1988, "The precise measurement of time," Am. Sci. **76**, 42.
Ramsey, N. F., 1990, "Experiments with separated oscillatory fields and hydrogen masers," Science **248**, 1612.
Reasenberg, R. D., 1983, "The constancy of G and other gravitational experiments," Philos. Trans. R. Soc. London **310**, 227.
Reasenberg, R. D., I. I. Shapiro, P. E. MacNeil, R. B. Goldstein, J. C. Breidenthal, J. P. Brenkle, D. L. Cain, T. M. Kaufman, T. A. Komarek, and A. I. Zygielbaum, 1979, "VIKING relativity experiment: verification of signal retardation by solar gravity," Astrophys. J. **234**, L219.
Roth, L. E., G. S. Downs, R. S. Saunders, and G. Schubert, 1980, "Radar altimetry of South Tharsis, Mars," Icarus **42**, 287.
Roth, L. E., R. S. Saunders, G. S. Downs, and G. Schubert, 1989, "Radar altimetry of large Martian craters," Icarus **79**, 289.
Russell, H. N., 1900, "The general perturbations of the major axis of Eros by the action of Mars," Astron. J. **21**, 25.
Samarasinha, N. H., and M. F. A'Hearn, 1991, "Observational and dynamical constraints on the rotation of Comet P/Halley," Icarus **93**, 194.
Schaber, G. G., R. G. Strom, H. J. Moore, L. A. Soderblom, R. L. Kirk, D. J. Chadwick, D. D. Dawson, L. R. Gaddis, J. M. Boyce, and J. Russell, 1992, "Geology and distribution of impact craters on Venus: What are they telling us?" J. Geophys. Res. **97**, 13 257.
Seidelmann, P. K., B. Guinot, and L. E. Doggett, 1992, "Time," in *Explanatory Supplement to the Astronomical Almanac,* edited by P. K. Seidelmann (University Science Books, Mill Valley, CA), p. 39.
Seidelmann, P. K., and G. A. Wilkins, 1992, "Introduction to positional astronomy," in *Explanatory Supplement to the Astronomical Almanac,* edited by P. K. Seidelmann (University Science Books, Mill Valley, CA), p. 1.
Shapiro, I. I., 1964, "Fourth test of general relativity," Phys. Rev. Lett. **13**, 789.
Shapiro, I. I., 1965, "Radar determination of the astronomical unit," paper presented to the IAU Symposium No. 21, Paris, Bull. Astron. **25**, 177.
Shapiro, I. I., 1966, "Testing general relativity with radar," Phys. Rev. **141**, 1219.
Shapiro, I. I., 1967, "Theory of the radar determination of planetary rotations," Astron. J. **72**, 1309.
Shapiro, I. I., 1968, "Spin and orbital motions of the planets," in *Radar Astronomy,* edited by J. V. Evans and T. Hagfors (McGraw-Hill, New York), p. 143.
Shapiro, I. I., 1980, "Experimental tests of the general theory of relativity," in *General Relativity and Gravitation, Vol. 2,* edited by A. Held (Plenum, New York), p. 469.
Shapiro, I. I., 1987, "Radar tests of gravitational theories and other exotica," in *Proceedings of the Arecibo Upgrading Workshop,* edited by J. H. Taylor and M. M. Davis (National Astronomy and Ionosphere Center, Arecibo, Puerto Rico), p. 225.
Shapiro, I. I., M. E. Ash, R. P. Ingalls, W. P. Smith, D. B. Campbell, R. B. Dyce, R. F. Jurgens, and G. H. Pettengill, 1971, "Fourth test of general relativity: new radar result," Phys. Rev. Lett. **26**, 1132.
Shapiro, I. I., M. E. Ash, and W. B. Smith, 1968, "Icarus: further confirmation of the relativistic perihelion precession," Phys. Rev. Lett. **20**, 1517.
Shapiro, I. I., M. E. Ash, and M. J. Tausner, 1966, "Radar verification of the Doppler formula," Phys. Rev. Lett. **17**, 933.
Shapiro, I. I., D. B. Campbell, and W. M. De Campli, 1979, "Nonresonance rotation of Venus?"Astrophys. J. **230**, L123.
Shapiro, I. I., J. F. Chandler, D. B. Campbell, A. A. Hine, and N. J. S. Stacy, 1990, "The spin vector of Venus," Astron. J. **100**, 1363.
Shapiro, I. I., G. H. Pettengill, M. E. Ash, R. P. Ingalls, D. B. Campbell, and R. B. Dyce, 1972, "Mercury's perihelion advance: determination by radar," Phys. Rev. Lett. **28**, 1594.
Shapiro, I. I., G. H. Pettengill, M. E. Ash, M. L. Stone, W. B. Smith, R. P. Ingalls, and R. A. Brockelman, 1968, "Fourth test of general relativity: preliminary results," Phy. Rev. Lett. **20**,1265.
Shapiro, I. I., W. B. Smith, M. E. Ash, and S. Herrick, 1971, "General relativity and the orbit of Icarus," Astron. J. **76**, 588.
Shapiro, I. I., W. B. Smith, M. B. Ash, R. P. Ingalls, and G. H. Pettengill, 1971, "Gravitational constant: experimental bound on its time variation," Phys. Rev. Lett. **26**, 27.
Shapiro, I. I., S. H. Zisk, A. E. E. Rogers, M. A. Slade, and T. W. Thompson, 1972, "Lunar topography: global determination by radar," Science **172**, 939.
Shoemaker, E. M., J. G. Williams, E. F. Helin, and R. F. Wolfe, 1979, "Earth-crossing asteroids: orbital classes, collision rates with Earth, and origin," in Asteroids, edited by T. Gehrels (University of Arizona, Tucson), p. 253.
Shoemaker, E. M., R. F. Wolfe, and C. S. Shoemaker, 1990, "Asteroid and comet flux in the neighborhood of the Earth,"

in *Global Catastrophes in Earth History; An Interdisciplinary Conference on Impacts, Volcanism and Mass Mortality* (Geol. Soc. Am. Spec. Paper. 247, Boulder), p. 155.

Sihvola, A. H., and J. A. Kong, 1988, "Effective permittivity of dielectric mixtures," IEEE Trans. Geosci. Remote Sensing **26**, 420.

Simpson, R. A., 1973, "Lunar radar echoes: an interpretation emphasizing characteristics of the leading edge," Ph.D. thesis (Stanford University).

Simpson, R. A., J. K. Harmon, S. H. Zisk, T. W. Thompson, and D. O. Muhleman, 1992, "Radar determination of Mars radar properties," in Mars, edited by H. Kieffer, B. Jakosky, C. Snyder, and M. Matthews (University of Arizona, Tucson), p. 652.

Simpson, R. A., and G. L. Tyler, 1982, "Radar scattering laws for the lunar surface," IEEE Trans. Antennas Propag. **AP-30**, 438.

Slade, M. A., B. J. Butler, and D. O. Muhleman, 1992, "Mercury radar imaging: evidence for polar ice," Science **258**, 635.

Slade, M. A., Z. Zohar, and R. F. Jurgens, 1990, "Venus: improved spin vector from Goldstone radar observations," Astron. J. **100**, 1369.

Solomon, S. C., and J. W. Head, 1991, "Fundamental issues in the geology and geophysics of Venus," Science **252**, 252.

Solomon, S. C., J. W. Head, W. M. Kaula, D. McKenzie, B. Parsons, R. J. Phillips, G. Schubert, and M. Talwani, 1991, "Venus tectonics: initial analysis from Magellan," Science **252**, 297.

Solomon, S. C., *et al.*, 1992, "Venus tectonics: an overview of Magellan observations," J. Geophys. Res. **97**, 13 199.

Sovers, O. J., and J. L. Fanselow, 1987, "Observation model and parameter partials for the JPL VLBI parameter estimation software MASTERFIT, 1987," Jet Propulsion Laboratory Publication No. 83-39, Rev. 3.

Stacy, N. J. S., 1993, "High-resolution synthetic aperture radar observations of the Moon," Ph.D. thesis (Cornell University).

Standish, E. M., 1990, "The observational basis for JPL's DE200, the planetary ephemerides of the astronomical almanac," Astron. Astrophys. **233**, 252.

Standish, E. M., and R. W. Hellings, 1989, "A determination of the masses of Ceres, Pallas, and Vesta from their perturbations upon the orbit of Mars," Icarus **80**, 326.

Standish, E. M., X. X. Newhall, J. G. Williams, and D. K. Yeomans, 1992, "Orbital ephemerides of the Sun, Moon, and Planets," in *Explanatory Supplement to the Astronomical Almanac,* edited by P. K. Seidelmann (University Science Books, Mill Valley, CA), p. 279.

Stern, S. A., and F. Vilas, 1988, "Future observations of and missions to Mercury," in *Mercury,* edited by F. Vilas, C. R. Chapman, and M. S. Matthews (University of Arizona, Tucson), p. 24.

Sulzer, M. P., 1986, "A radar technique for high range resolution incoherent scatter autocorrelation function measurements utilizing the full average power of klystron radars," Radio Sci. **21**, 1033.

Sulzer, M. P., 1989, "Recent incoherent scatter techniques," Adv. Space Res. **9**, 153.

Swindle, T. D., J. S. Lewis, and L. A. McFadden, 1991, "Near-Earth asteroids and the history of planetary formation," Eos **72**, 473.

Thompson, T. W., S. H. Zisk, R. W. Shorthill, and J. A. Cutts, 1981, "Lunar craters with radar bright ejecta," Icarus **46**, 201.

Thomson, J. H., 1963, "Planetary radar," Q. J. R. Astron. Soc. **4**, 347.

Thomson, J. H., and J. E. B. Ponsonby, 1968, "Two-dimensional aperture synthesis in lunar radar astronomy," Proc. R. Soc. London, Ser. A **303**, 477.

Tryka, K. A., and D. O. Muhleman, 1992, "Reflection and emission properties on Venus: Alpha Regio," J. Geophys. Res. **97**, 13 379.

Tyler, G. L., 1976, "Wavelength dependence in radio-wave scattering and specular point theory," Radio Sci. **11**, 83.

Tyler, G. L., 1979, "Comparison of quasi-specular radar scatter from the Moon with surface parameters obtained from images," Icarus **37**, 29.

Tyler, G. L., P. G. Ford, D. B. Campbell, C. Elachi, G. H. Pettengill, and R. A. Simpson, 1991, "Magellan: electrical and physical properties of Venus' surface," **252**, 265.

Tyler, G. L., and R. A. Simpson, 1970, "Bistatic radar measurements of topographic variations in lunar surface slopes with Explorer 5," Radio Sci. **5**, 263.

Tyler, G. L., R. A. Simpson, M. J. Maurer, and E. Holmann, 1992, "Scattering properties of the Venusian surface: preliminary results from Magellan," J. Geophys. Res. **98**, 13 115.

Ulaby, F. T., R. K. Moore, and A. K. Fung, 1982, *Microwave Remote Sensing, Vol. 1* (Addison-Wesley, Reading, PA).

Ulaby, F. T., T. H. Bengal, M. C. Dobson, J. R. East, J. B. Garvin, and D. L. Evans, 1990, "Microwave dielectric properties of dry rocks," IEEE Trans. Geosci. Remote Sensing **28**, 325.

van Albada, M. P., and A. Lagendijk, 1985, "Observation of weak localization of light in a random medium," Phys. Rev. Lett. **55**, 2692.

van Albada, M. P., M. B. van der Mark, and A. Lagendijk, 1990, "Experiments on weak localization of light and their interpretation," in *Scattering and Localization of Classical Waves in Random Media,* edited by P. Sheng (World Scientific, Singapore), p. 97.

van de Hulst, H. C., 1980, *Multiple Light Scattering* (Academic, New York).

Wahr, J. M., 1988, "The Earth's rotation," Annu. Rev. Earth Planet. Sci. **16**, 231.

Warren, S. G., 1984, "Optical constants of ice from the ultraviolet to the microwave," Appl. Opt. **23**, 1206.

Wasson, J. T., 1985, *Meteorites: Their Record of Early Solar System History* (Freeman, New York).

Weidenschilling, S. J., 1980, "Hektor: nature and origin of a binary asteroid," Icarus **44**, 807.

Weidenschilling, S. J., P. Paolicchi, and V. Zappalà, 1989, "Do asteroids have satellites?" in *Asteroids II,* edited by R. P. Binzel, T. Gehrels, and M. S. Matthews (University of Arizona, Tucson), p. 643.

Weiss, M. A., and D. W. Allan, 1987, "An NBS calibration procedure for providing time and frequency at a remote site by weighting and smoothing of GPS common view data," IEEE Trans. Instrum. Meas. **IM-36**, 572.

Weissman, P. R., M. F. A'Hearn, L. A. McFadden, and H. Rickman, 1989, "Evolution of comets into asteroids," in *Asteroids II,* edited by R. P. Binzel, T. Gehrels, and M. S. Matthews (University of Arizona, Tucson), p. 880.

Wetherill, G. W., 1977, "Evolution of the Earth's planetesimal swarm subsequent to the formation of the Earth and Moon," Proc. Lunar Sci. Conf. 8th, 1.

Wetherill, G. W., 1988, "Where do the Apollo objects come from?" Icarus **76**, 1.

Wetherill, G. W., and C. R. Chapman, 1988, "Asteroids and meteorites," in *Meteorites and the Early Solar System,* edited by J. F. Kerridge and M. S. Matthews (University of Arizona, Tucson), p. 35.

Whipple, F. L., 1987, "The cometary nucleus: current concepts," Astron. Astrophys. **187**, 852.
Will, C. M., 1984, "The confrontation between general relativity and experiment: an update," Phys. Rep. **113**, 345.
Will, C. M., 1987, "Experimental gravitation from Newton's *Principia* to Einstein's General Relativity," in *Three Hundred Years of Gravitation,* edited by S. Hawking and W. Israel (Cambridge University, Cambridge, England), p. 80.
Williams, J. G., 1969, "Secular perturbations in the solar system," Ph.D. thesis (University of California at Los Angeles).
Williams, J. G., 1984, "Determining asteroid masses from perturbations on Mars," Icarus **57**, 1.
Williams, J. G., and E. M. Standish, 1989, "Dynamical reference frames in the planetary and Earth-Moon systems," in *Reference Frames in Astronomy and Geophysics,* edited by J. Kovalevsky, I. Mueller, and B. Kolaczek (Kluwer, Dordrecht), p. 67.
Wisdom, J., 1987, "Urey Prize lecture: Chaotic dynamics in the solar system," Icarus **72**, 241.
Wolf, P., and G. Maret, 1985, "Weak localization and coherent backscattering of photons in disordered media," Phys. Rev. Lett. **55**, 2696.
Wood, J., 1985, "Meteoritic constraints on processes in the Solar Nebula: an overview," in *Protostars & Planets II,* edited by D. C. Black and M. S. Matthews (University of Arizona, Tucson), p. 687.
Wood, S. E., A. R. Vasavada, and D. A. Paige, 1992, "Temperatures in the polar regions of Mercury: Implications for water ice," Bull. Am. Astron. Soc. **24**, 957.
Yeomans, D. K., P. W. Chodas, M. S. Keesey, S. J. Ostro, J. F. Chandler, and I. I. Shapiro, 1992, "Asteroid and comet orbits using radar data," Astron. J. **103**, 303.
Yeomans, D. K., S. J. Ostro, and P. W. Chodas, 1987, "Radar astrometry of near-Earth Asteroids," Astron. J. **94**, 189.
Zinner, E., 1988, "Interstellar cloud material in meteorites," in *Meteorites and the Early Solar System,* edited by J. F. Kerridge and M. S. Matthews (University of Arizona, Tucson), p. 956.
Zisk, S. H., P. J. Mouginis-Mark, J. M. Goldspiel, M. A. Slade, and R. F. Jurgens, 1992, "Valley systems on Tyrrhena Patera, Mars: Earth-based radar measurements of slopes," Icarus **96**, 226.

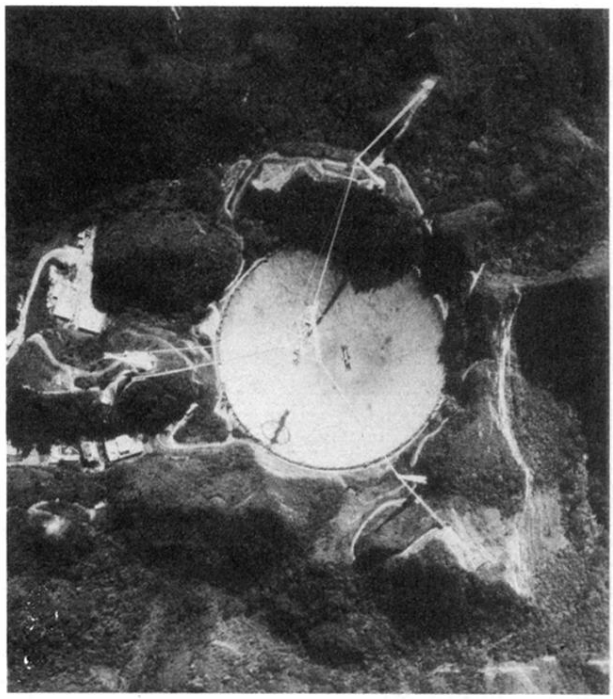

(a)

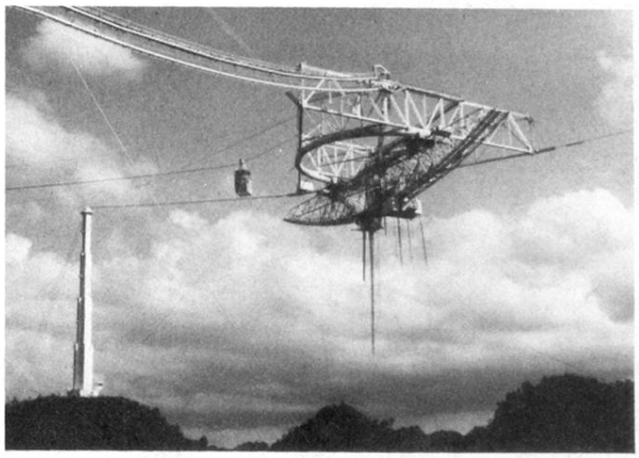

(b)

FIG. 1. The Arecibo Observatory in Puerto Rico: (a) aerial view; (b) the structure suspended above the reflector. Antenna feeds extend from the bottom of two carriage houses that contain the transmitter and the maser amplifier. Courtesy National Astronomy and Ionosphere Center.

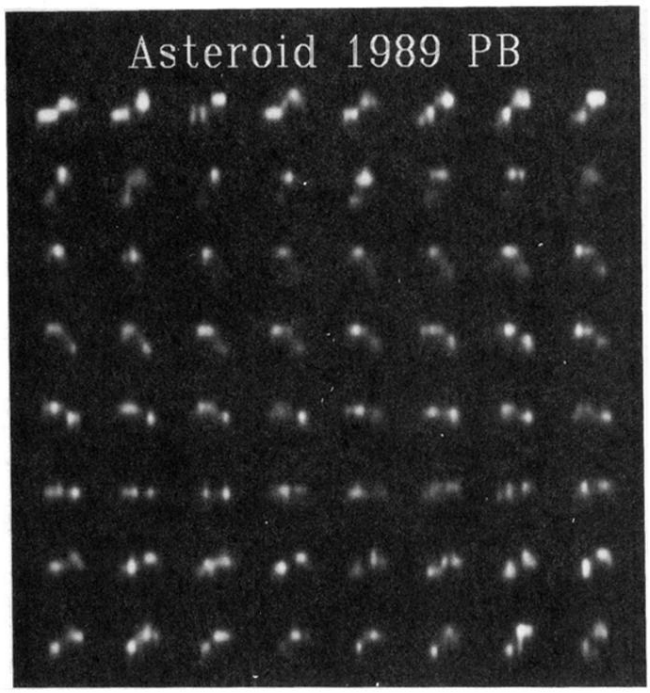

(a)

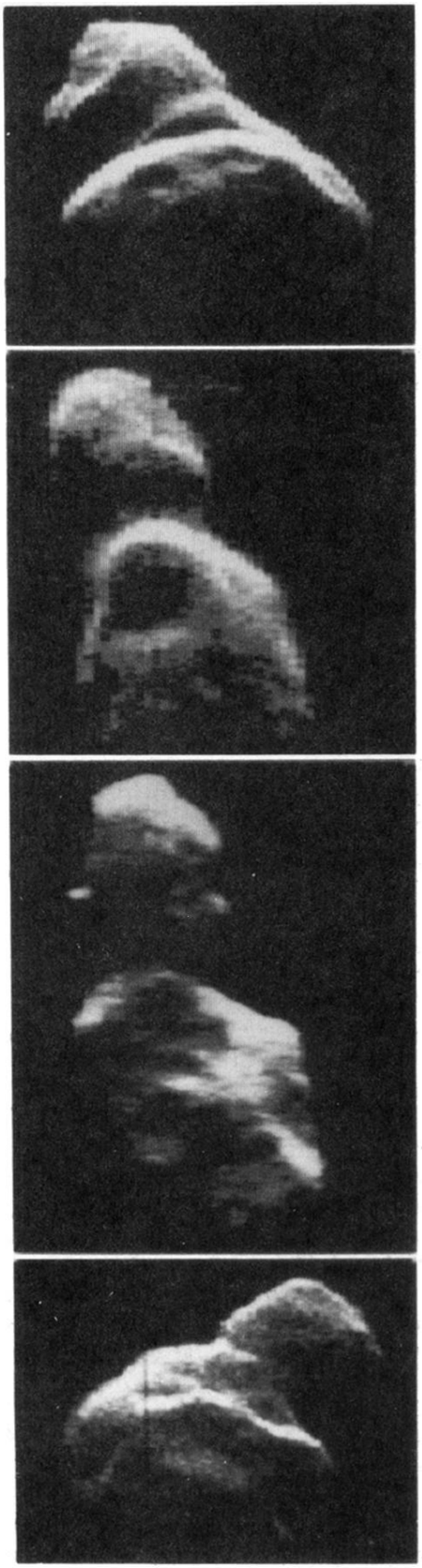

(b)

FIG. 11. Radar images of Earth-crossing asteroids: (a) This 64-frame Arecibo "movie" of 4769 Castalia (1989 PB) is to be read like a book (left to right in the top row, etc.). The radar lies toward the top of the page in the image plane, which probably is within a few tens of degrees of the asteroid's equator. In each frame, OC echo power (i.e., the brightness seem by the radar) is plotted vs time delay (increasing from top to bottom) and frequency (increasing from left to right). The radar illumination comes from the top of the screen; so parts of the asteroid facing toward the bottom are not seen in these images. The object, each of whose lobes is about a kilometer in diameter, is seen rotating through about 220° during the 2.5-h sequence. (Ostro, Chandler, Hine, *et al.*, 1990. Copyright 1990 by the AAAS.) (b) Goldstone radar images of asteroid 4179 Toutatis, made during the object's very close approach to Earth in December 1992, reveal two irregularly shaped, cratered objects about 2.5 and 1.5 kilometers in maximum dimension, probably in contact with each other. The four frames here were obtained on (from top to bottom) Dec. 8, 9, 10, and 13, with Toutatis an average of about 10 lunar distances from Earth. On each date, the asteroid was in a different orientation. The images sum data taken over intervals of 55, 14, 37, and 85 minutes, respectively. The radar illumination comes from the top of the page, so parts of each component facing toward the bottom are not seen in the images. The data's range (vertical) resolution is 0.125 μs (19 m). Doppler frequency increases from right to left. The distance equivalent of the frequency resolution (0.033 Hz) in each frame is a function of the instantaneous, apparent spin vector, which had not been estimated at the time these images were prepared; arbitrary conversions from hertz to kilometers were used here. The large crater in the Dec. 9 image is roughly 700 meters in diameter (JPL/NASA; Ostro *et al*, 1993).

FIG. 16. Arecibo OC and SC delay-Doppler maps of the 93-km-diameter lunar crater Copernicus (10° N, 20° W), courtesy of N. J. S. Stacy and D. B. Campbell. The resolution is 900 m.

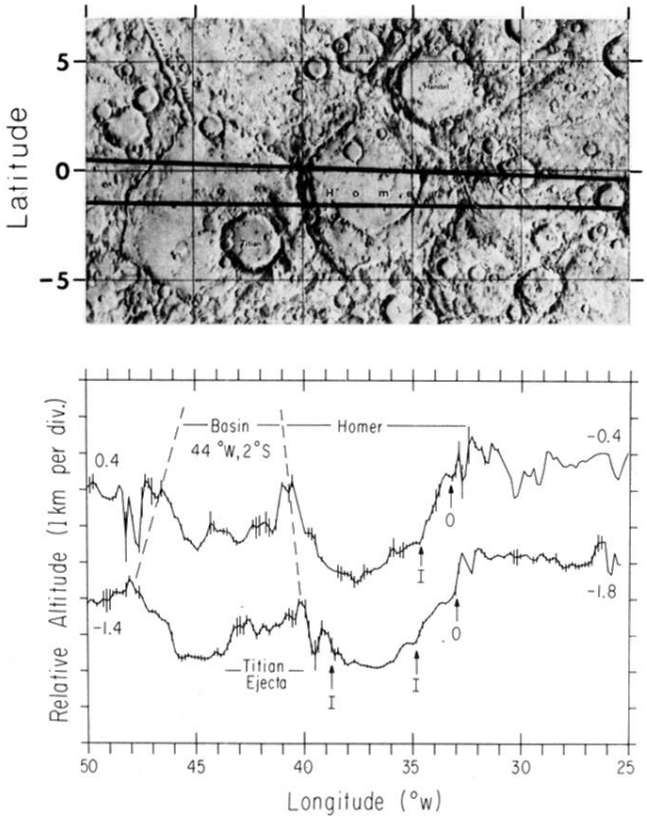

FIG. 17. Mercury altitude profiles (bottom) showing topography across Homer Basin and a large, un-named basin to the west, estimated from observations whose subradar tracks are shown on the shaded-relief map (top). Broken lines indicate approximate locations of the basin rims as seen in Mariner 10 images. Arrows locate Homer's inner/outer (*I*/*O*) basin rings (Harmon, Campbell, and Bindschadler *et al.*, 1986).

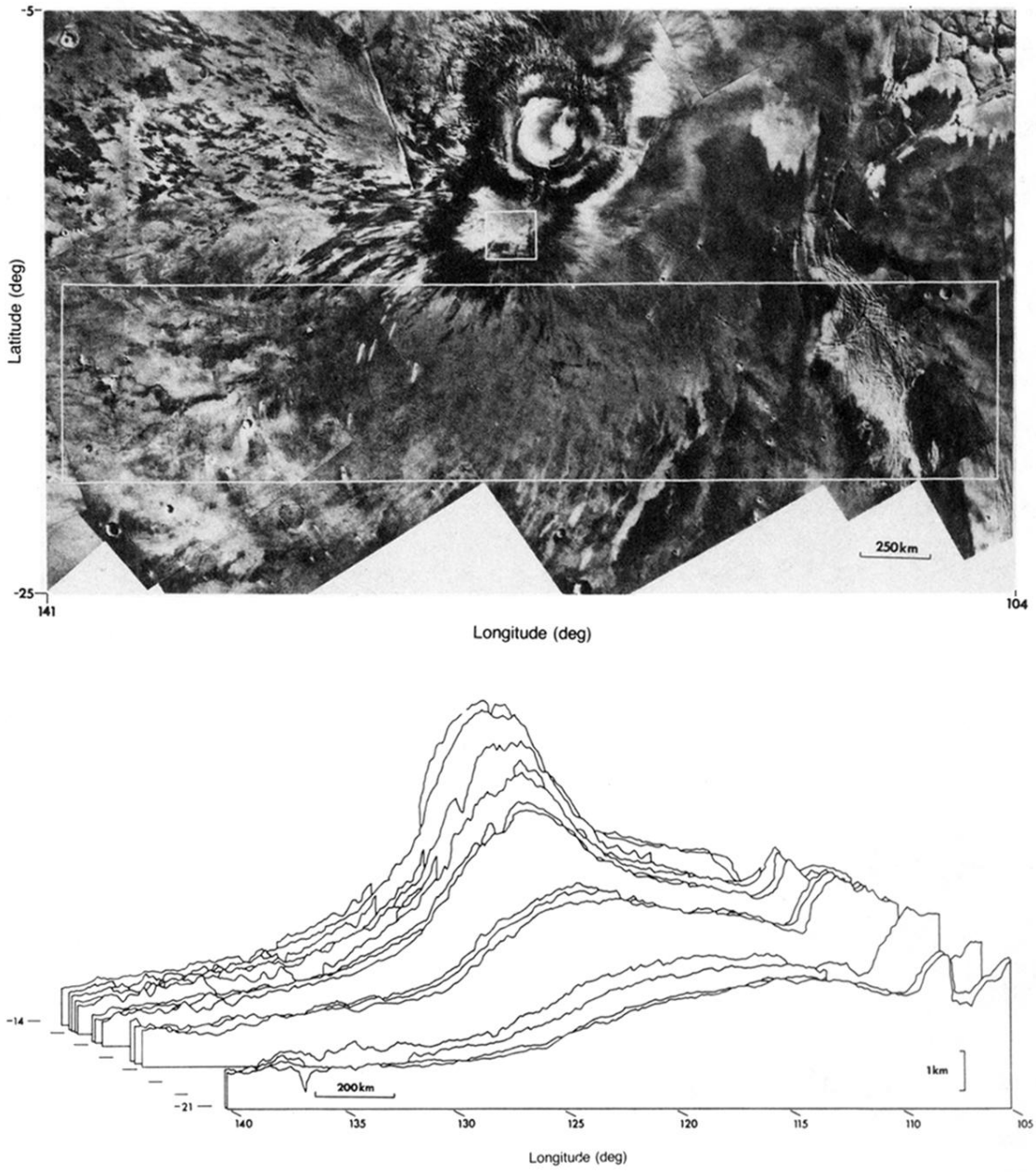

FIG. 18. Topographic contours for the southern flank (large rectangle) of the Martian shield volcano Arsia Mons, obtained from radar altimetry (Roth *et al.*, 1980).

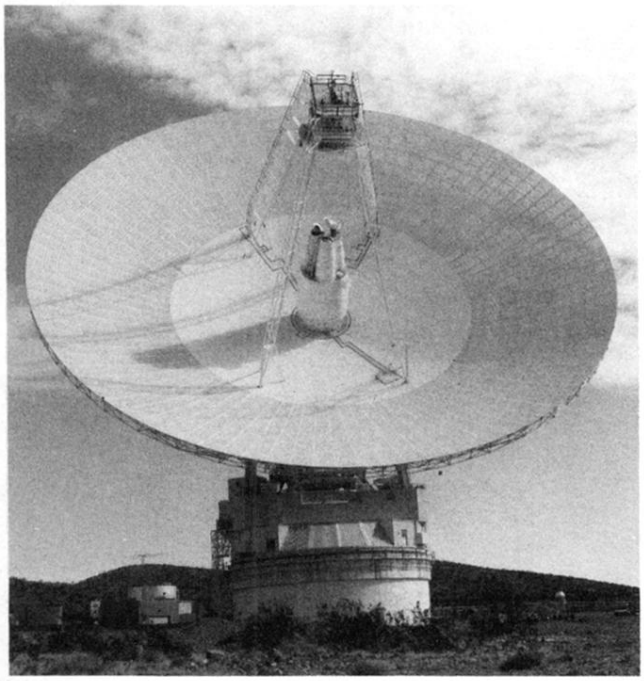

FIG. 2. The 70-m Goldstone Solar System Radar antenna (DSS 14) in California. Planetary radar equipment is at the secondary focus in the nearest of the three cones.

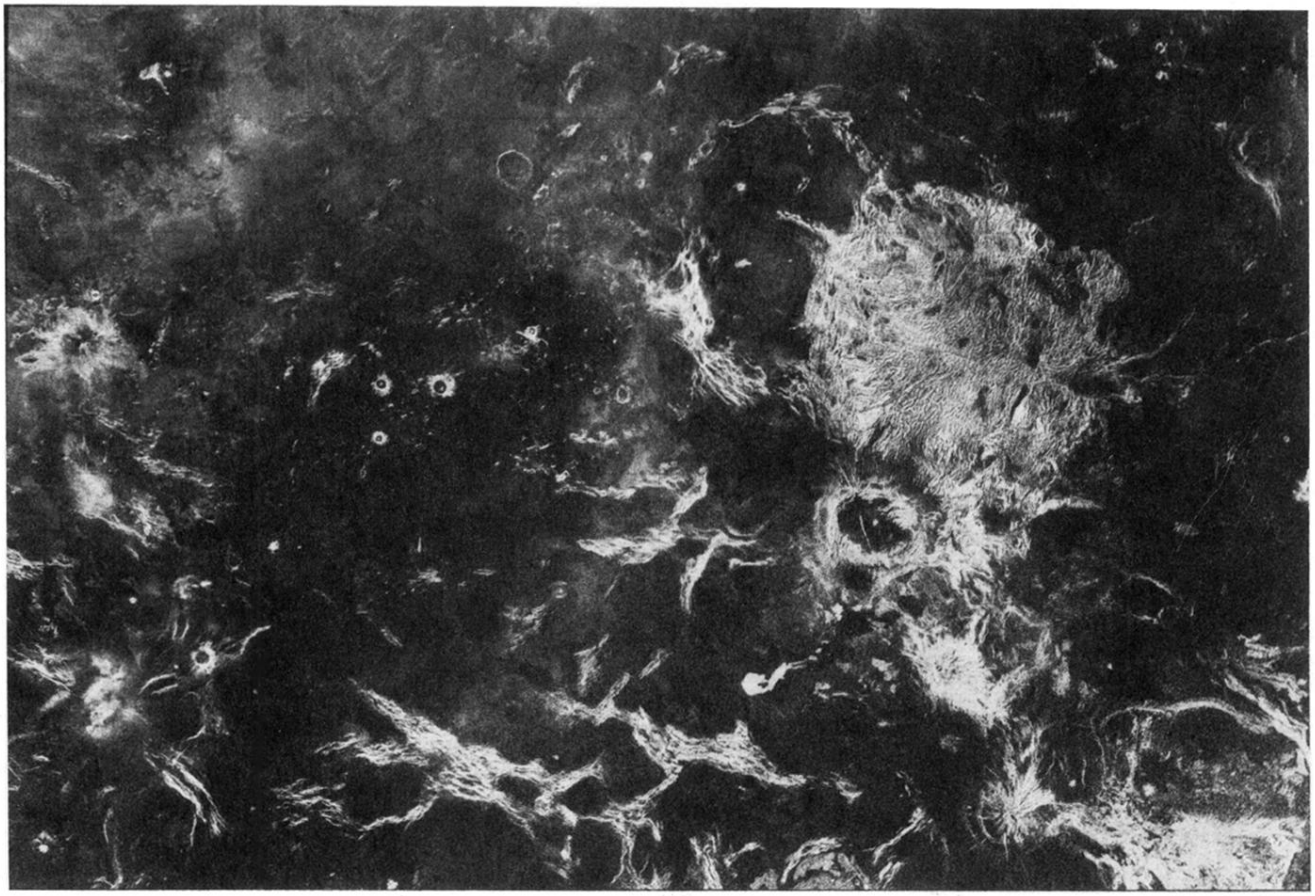

FIG. 21. Arecibo OC delay-Doppler map of Venus. In the middle of the right half of the figure is the bright 1200-km-wide Alpha Regio, a complex of intersecting ridges. Just south of Alpha is the 300-km-diameter circular feature Eve. The three prominent craters in the middle of the left half of the figure are seen close-up in Fig. 22(d). Courtesy of D. B. Campbell.

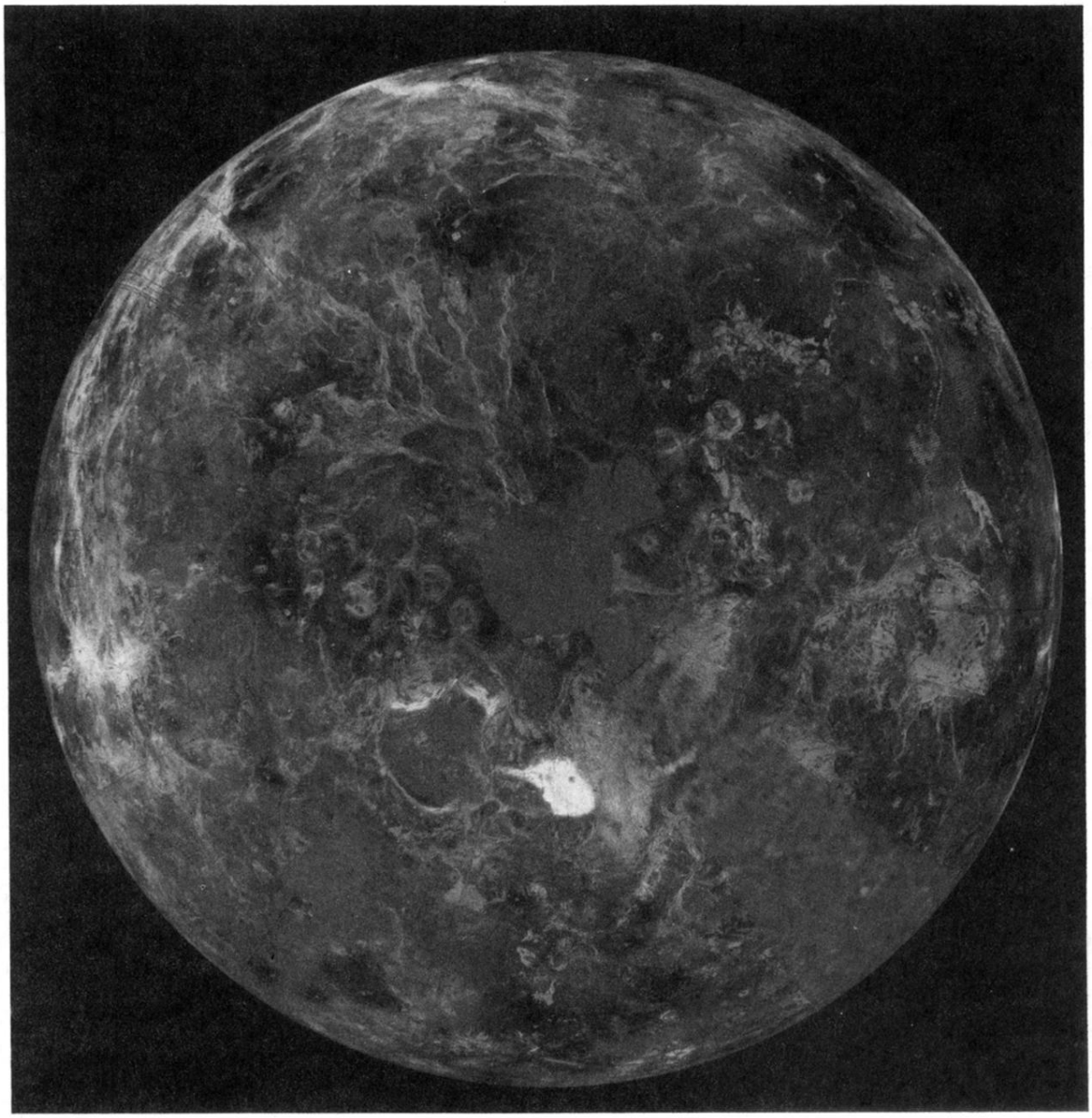

(a)

FIG. 22. Magellan 13-cm SL radar maps of Venus: (a) Northern-hemisphere projection of mosaics. The north pole is at the center with 0° and 90° E longitudes at the 12 and 9 o'clock positions. Gaps use Pioneer Venus data or interpolations. The bright porkchop-shaped feature is Maxwell Montes, a tectonically produced mountain range first seen in ground-based images. (b) 120-m-resolution map of Cleopatra, a double-ringed impact basin on the eastern slopes of Maxwell Montes. The diameter of the outer ring is about 100 km. (c) A 350-km-wide portion of the Atla region of Venus's southern hemisphere. Several types of volcanic features are crisscrossed by numerous superimposed, and hence more recent, surface fractures. Various flower-shaped patterns formed from linear fissures or lava flows emanate from circular pits. Near the center, a 10-by-20-km collapse formation is drained by a 40-km lava channel. (d) Mosaic of part of Lavinia showing three large craters, with diameters ranging from 37 to 50 km, that were discovered in Arecibo images; see Fig. 21. Note the abundant fractured planes and numerous small volcanic domes. (e) Pancakelike volcanic domes located southeast of Alpha Regio. These ~25-km-diameter edifices probably formed from extrusion of viscous magmas from central conduits (Ford *et al.*, 1991; JPL/NASA).

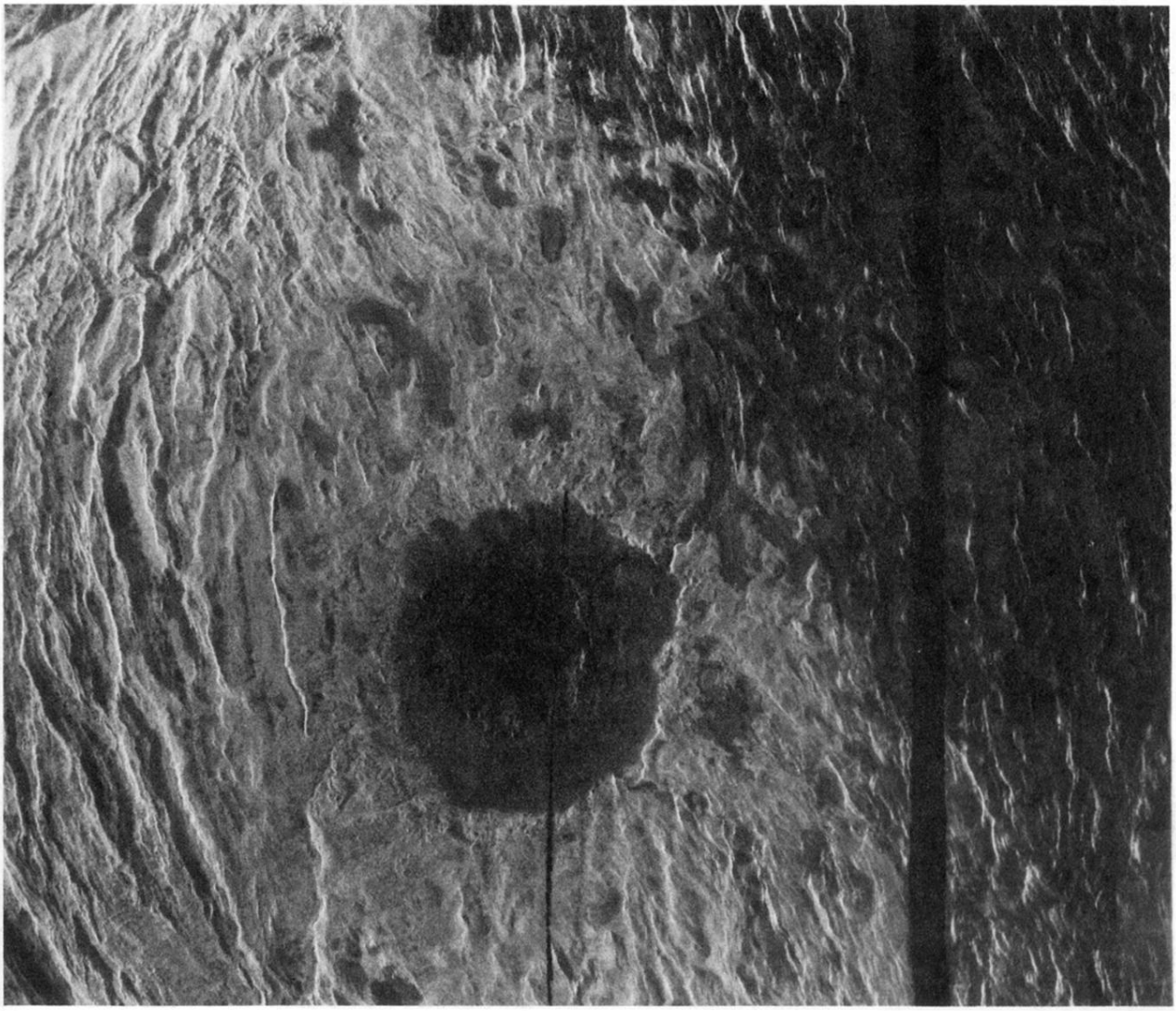

(b)

FIG. 22. (*Continued*).

(c)

FIG. 22. (*Continued*).

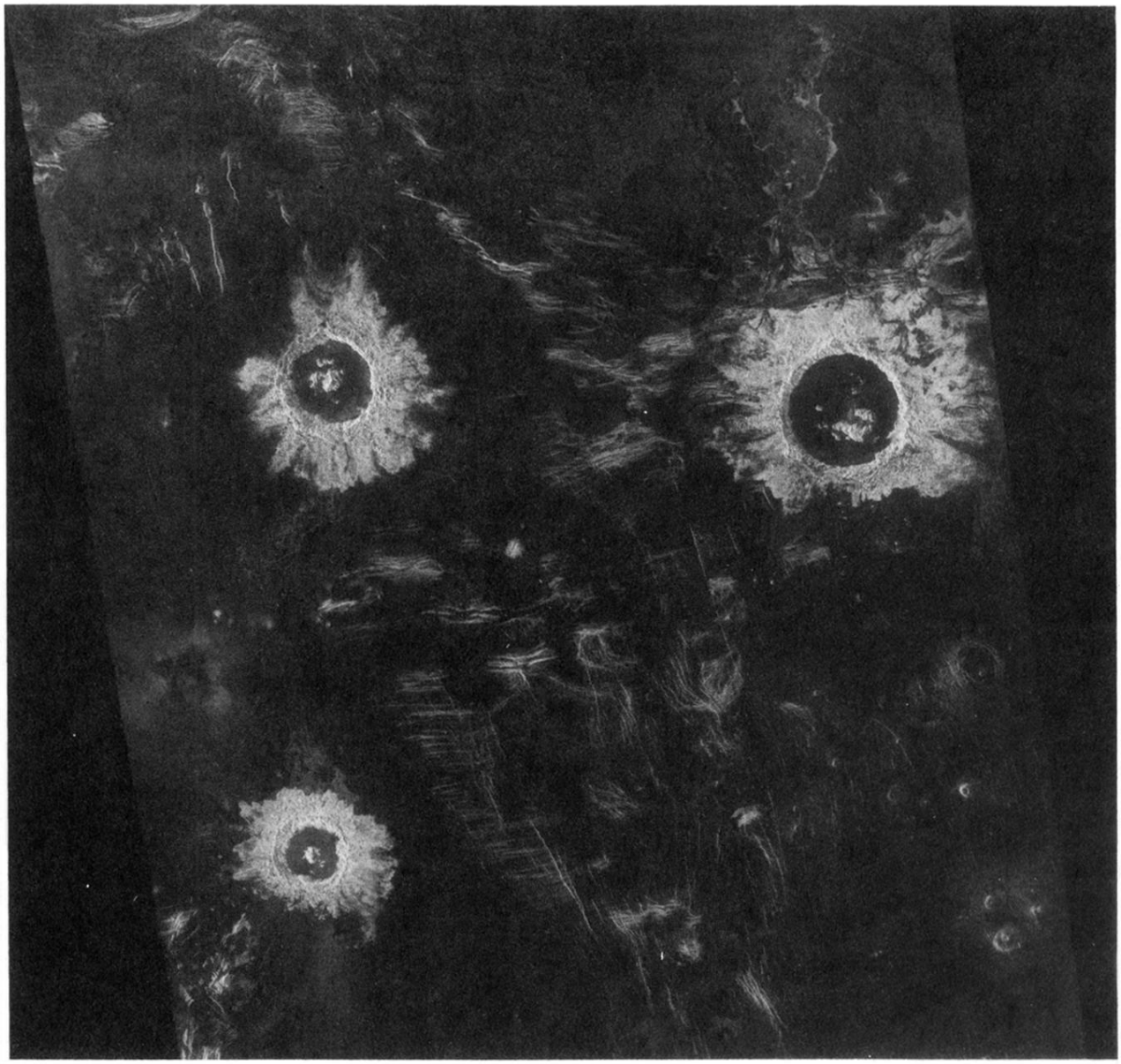

(d)

FIG. 22. (*Continued*).

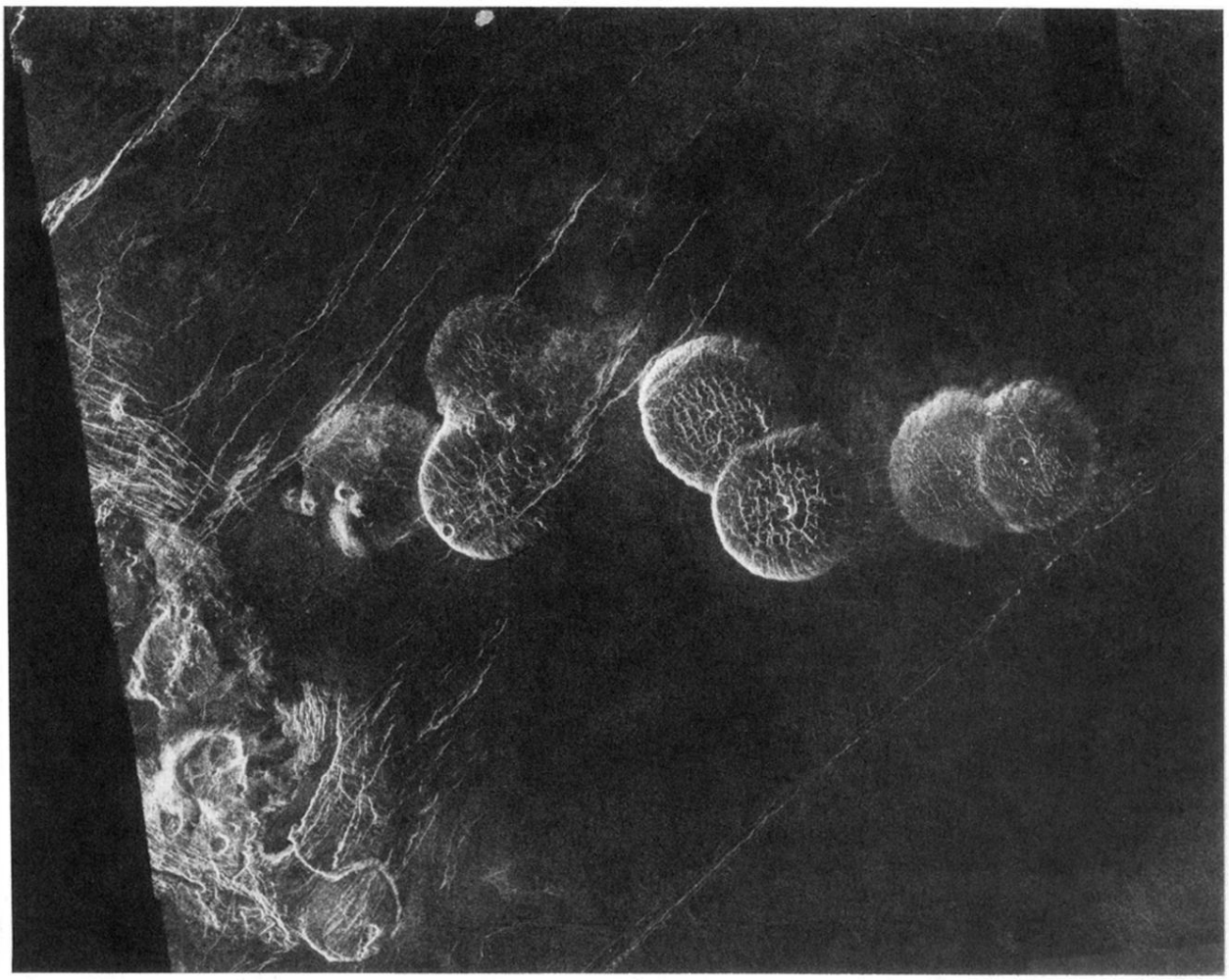

(e)

FIG. 22. (*Continued*).

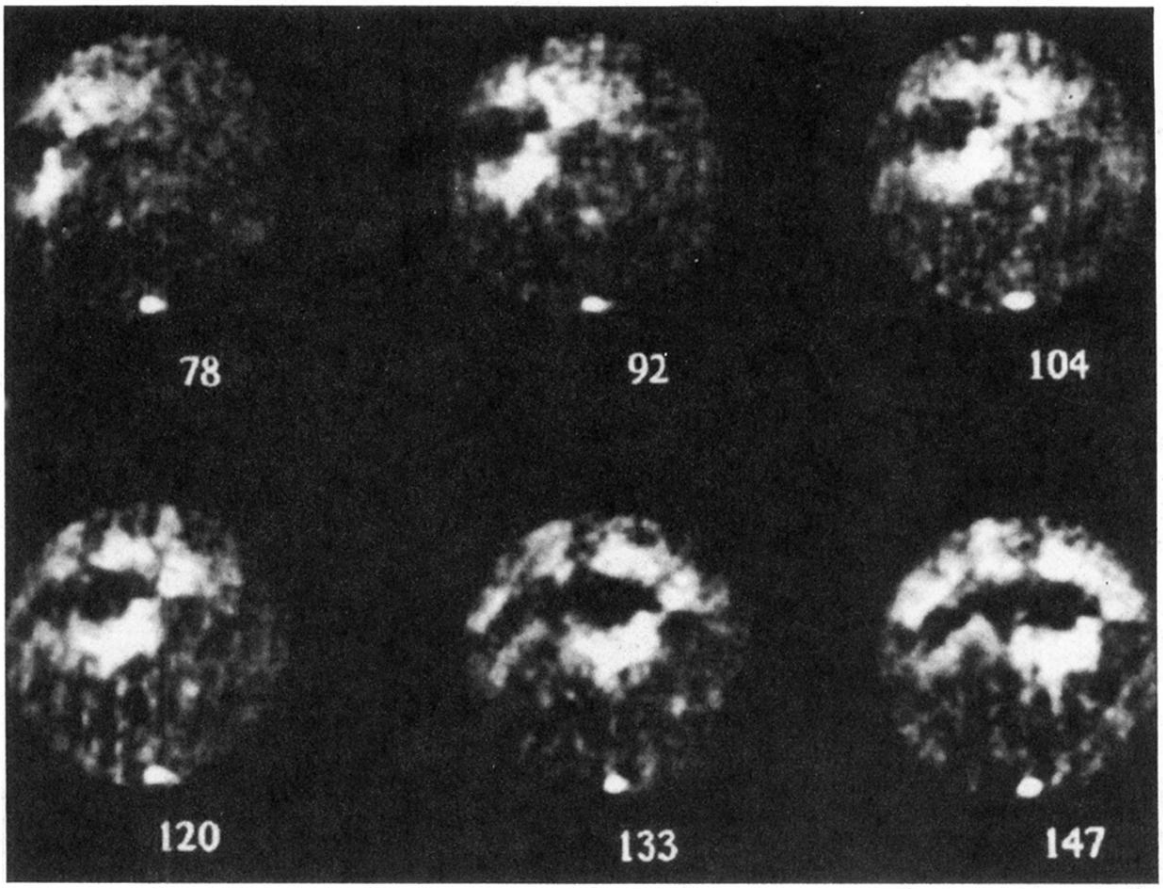

FIG. 23. Goldstone-VLA images of Mars at six west longitudes (deg), made at 3.5 cm in the SC polarization. Note the very bright residual south polar ice cap. In the north hemisphere, the brightest features are in Tharsis, which is traversed by the low-albedo Stealth region (Muhleman *et al.*, 1991).

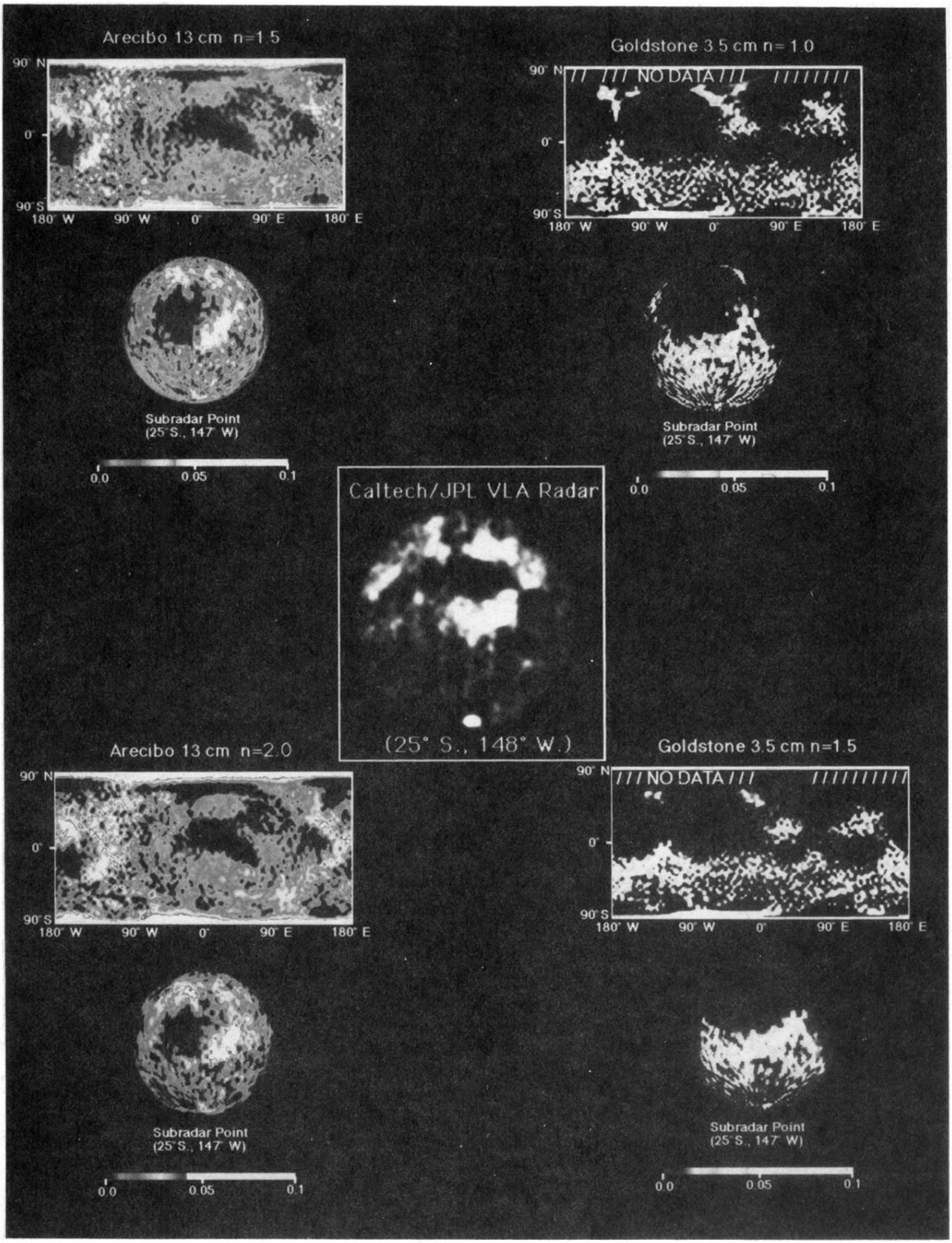

FIG. 24. Mars SC maps made from inversion of echo spectra obtained at Arecibo (left) and Goldstone (right). In the inversion, the albedos of individual surface facets were adjusted using least squares. For each observatory, results are shown for two assumed values of the exponent in a $\cos^n\theta$ scattering law. In the center is one of the Goldstone-VLA images from Fig. 23. After Harmon, Slade, and Hudson, 1992.

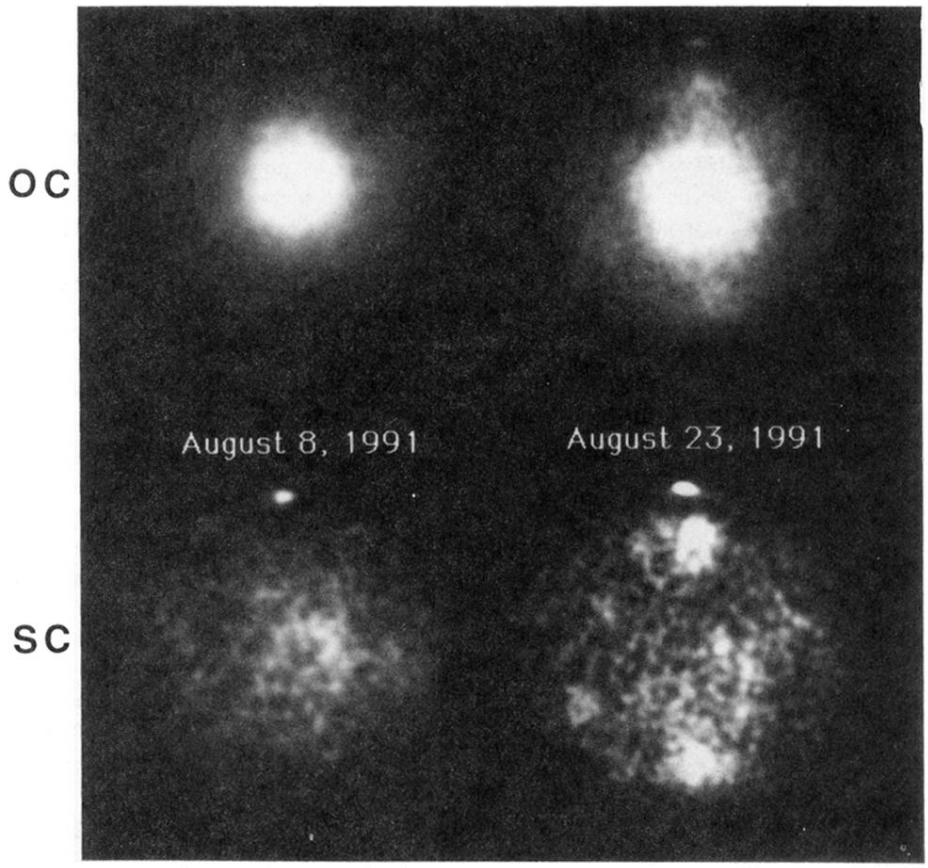

FIG. 26. Goldstone-VLA images of Mercury taken at 3.5 cm in the SC and OC polarizations at 11° N and longitudes 253° W (left) and 354° W. The SC and OC images have different brightness scales (Slade *et al.*, 1992).

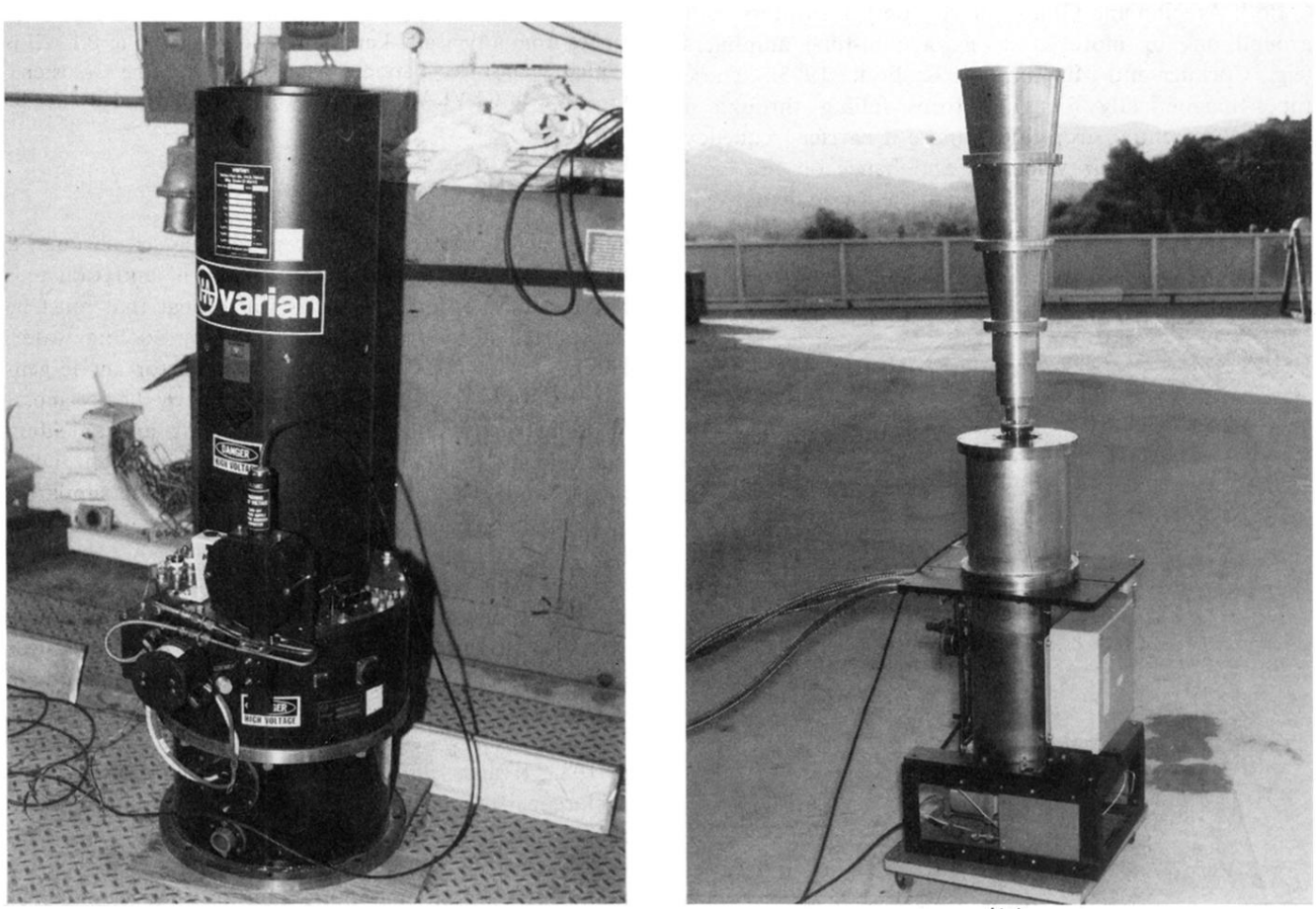

FIG. 4. Transmitter and receiver components: (a) A 250-kW, 8510-MHz klystron mounted in its solenoid and sitting in its stand. The tube is 1.5 m tall and weighs 835 lb. (b) 8510-MHz traveling-wave maser and feed horn. The maser's closed-cycle refrigeration system uses recirculating helium gas. The entire apparatus stands 1.7 m tall (JPL/NASA).